



Universiteit
Leiden

The Netherlands

The Shapes and Spins of Kuiper Belt Objects

Lacerda, Pedro

Citation

Lacerda, P. (2005, February 17). *The Shapes and Spins of Kuiper Belt Objects*. Retrieved from <https://hdl.handle.net/1887/603>

Version: Corrected Publisher's Version

License: [Licence agreement concerning inclusion of doctoral thesis in the Institutional Repository of the University of Leiden](#)

Downloaded from: <https://hdl.handle.net/1887/603>

Note: To cite this publication please use the final published version (if applicable).

The Shapes and Spins of Kuiper Belt Objects

The Shapes and Spins of Kuiper Belt Objects

Proefschrift

ter verkrijging van
de graad van Doctor aan de Universiteit Leiden,
op gezag van de Rector Magnificus Dr. D.D. Breimer,
hoogleraar in de faculteit der Wiskunde en
Natuurwetenschappen en die der Geneeskunde,
volgens besluit van het College voor Promoties
te verdedigen op donderdag 17 februari 2005
klokke 15.15 uur

door

Pedro Bernardino Lacerda Cruz
geboren te Lisboa, Portugal
in 1975

Promotiecommissie

Promotor: Prof. dr. H.J. Habing

Referent: Dr. C. Dominik (Universiteit Amsterdam)

Overige leden: Dr. M. Hogerheijde
Dr. F.P. Israel
Dr. S. Kenyon (Harvard University, USA)
Dr. J. Luu (MIT Lincoln Laboratory, USA)
Prof. dr. G.K. Miley
Prof. dr. A. Quirrenbach
Prof. dr. S. Schlemmer (Universität zu Köln, Germany)
Prof. dr. P.T. de Zeeuw

There are infinite worlds both like and unlike this world of ours.

Epicurus (341–270 B.C.)

cover design: Maria Reis and Pedro Lacerda

Table of contents

	Page
Chapter 1. Introduction	1
1.1 The origin of comets	1
1.2 The Kuiper belt	7
1.3 Kuiper belt objects	11
1.4 Thesis summary	14
1.5 Future prospects	16
Chapter 2. Detectability of KBO lightcurves	21
2.1 Introduction	22
2.2 Definitions and Assumptions	24
2.3 “Flat” Lightcurves	26
2.4 Detectability of Lightcurves	28
2.5 Conclusions	32
Chapter 3. The shape distribution	35
3.1 Introduction	36
3.2 Observations	36
3.3 Discussion	38
3.3.1 Gaussian distribution	39
3.3.2 Power law distribution	42
3.4 Summary	45
Chapter 4. Analysis of the rotational properties	47
4.1 Introduction	48
4.2 Observations and Photometry	49
4.3 Lightcurve Analysis	52
4.3.1 Can we detect the KBO brightness variation?	53
4.3.2 Period determination	56
4.3.3 Amplitude determination	57
4.4 Results	58
4.4.1 1998 SN ₁₆₅	58
4.4.2 1999 DF ₉	58
4.4.3 2001 CZ ₃₁	60
4.4.4 Flat Lightcurves	63
4.4.5 Other lightcurve measurements	63
4.5 Analysis	63
4.5.1 Spin period statistics	66

4.5.2	Lightcurve amplitudes and the shapes of KBOs	67
4.5.3	The inner structure of KBOs	71
4.6	Conclusions	74
Chapter 5. Origin and evolution of KBO spins		79
5.1	Motivation	80
5.2	Spin evolution model	81
5.2.1	General description	81
5.2.2	Model Details	82
5.3	Results and Discussion	88
5.3.1	Effect of disruption energy scaling laws	89
5.3.2	Effect of density	89
5.3.3	High angular momentum collisions	92
5.4	The origin of KBO spin rates	94
5.4.1	Anisotropic accretion	96
5.5	Limitations and future improvements	101
5.6	Summary and Conclusions	101
Nederlandse samenvatting (Dutch summary)		105
Resumo em Português (Portuguese summary)		113
Curriculum Vitae		119
Nawoord / Acknowledgments		120

CHAPTER 1

Introduction

1.1 The origin of comets

BEFORE the XVIIth century comets were seen as portents of divine will, sent by the gods to punish mankind. Newton (1686) showed that the paths of these wandering celestial objects were actually very well defined, and obeyed the universal law of gravitation. Newton's theory, undoubtedly one of the greatest achievements of human intellect, successfully describes the motions of the moon around the Earth, of the planets around the Sun, of the Sun around the center of our galaxy, and so on and so forth.

Making use of Newton's laws, Halley (1705) proposed that three comet apparitions in 1456, 1531, and 1607 were actually three returns of the same comet. He predicted that the heavenly body should revisit the inner solar system in 1758. The comet returned around Christmas of 1758, twelve years after Halley's death, and has been called Halley's Comet ever since.

But understanding how comets move was only the first step. Humans are curious beings, and thereby began questioning. What are comets? Where do they come from? Aristotle (384–322 BC) was the first man that tried to explain comets as something physical. He speculated they were atmospheric phenomena—luminous clouds of gas—that because of their transient character could not be part of the perfect realm of the heavens. Aristotle called them *kometes*, which means “wearing long hair” in ancient Greek. As with most scientific disciplines, the Aristotelian way of thinking survived until the Renaissance. In the late XVth century natural philosophers recognized that observation is an essential tool in understanding natural phenomena. The works of Leonardo da Vinci (1452–1519)—who was probably the ultimate observer of nature—exemplify how much can be learnt from detailed observation of the surrounding world. The pioneer in accurate astronomical observations was the Danish astronomer Tycho Brahe. In 1577 he used observations of a comet made

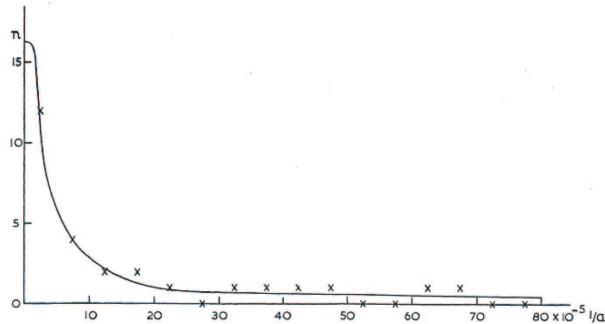


Figure 1.1 – Histogram of the reciprocal semi-major axes of comet orbits, in astronomical units. Reproduced from Oort & Schmidt (1951).

from different locations in Europe, to test the hypothesis of Aristotle. The small observed parallax¹ indicated that the comet had to be much further out than the Earth’s atmosphere—even further than the Moon.

As the number of observed comets increased, statistical analysis of their orbits became possible. Astronomers have divided the comets into two classes, according to their orbital period: the *short-period* comets, with periods shorter than 200 years, and the *long-period* comets, with periods longer than 200 years. The orbits of comets in each class are quite different. Short-period comets have prograde² orbits which lie close to the plane where planets move. This plane is called the ecliptic, and is defined as the plane of the orbit of the Earth. By contrast, the long-period comets come into the inner regions of the solar system from all directions—there is no preferred orbital plane. Furthermore, their long orbital periods indicate that they come from large distances, as a consequence of Kepler’s 3rd law of orbital motion.

The director of the Sterrewacht Leiden from 1945 to 1970 was Jan Hendrik Oort. By the time of his appointment, Oort had already made key contributions to astronomy. He had observationally confirmed, and analytically described the rotation of the Milky Way³ (Oort 1927), following a hypothesis by Lindblad (1925), and had made important contributions to the theory of dark matter (Oort 1940). In the fall of 1948, a PhD student of Oort, van Woerkom, obtained his doctor degree with a dissertation titled “On the origin of comets”. The work of his student got Oort pondering on the subject. A little over a year later he published his conclusions (Oort 1950). The high frequency of comet orbits with very small reciprocal semi-major axes (see Fig. 1.1) led Oort to propose

¹The apparent difference in position of a body on the sky (relative to the background stars) as seen from different points of observation.

²All planets orbit the Sun in the same direction, usually called direct or prograde.

³The Milky Way is the home galaxy to our solar system; it is a spiral galaxy, containing some 100 billion (10^{11}) stars.

the existence of a vast spherical swarm of comets extending to a radius of about 150 000 astronomical units⁴. Oort figured that this spherical cloud is occasionally be perturbed by stars passing close to the Sun. As a result, some comets are ejected to interstellar space, and some fall into the inner solar system along nearly parabolic orbits. The latter become the visible comets. The idea prevailed and the spherical reservoir became known as the “Oort cloud”. Although its existence cannot be observationally confirmed, the Oort cloud provides the best explanation of the observed distribution of the orbits of long-period comets.

Until late-1970s it was believed that short-period comets also originate in the Oort cloud. The evolution of cometary orbits, from randomly-oriented long-period to prograde low-inclination short-period trajectories, was attributed to perturbations by the giant planets, particularly Jupiter. It was necessary, however, to demonstrate that such evolution is possible, and that it correctly predicts the observed number of short-period comets. The work of van Woerkom (1948) was partly an attempt to show that long-period comets could be brought into short-period orbits due to perturbations by Jupiter. His theoretical calculations predicted that this process was a factor ~ 20 less efficient than needed to explain the observed frequency of short-period comets. With the advent of computers the complex analytical calculations of orbital evolution became complemented by numerical simulations. Everhart (1972, 1973, 1977), who favoured the idea that all comets originated from nearly parabolic orbits, used Monte Carlo simulations to show that a fraction of long-period comets with perihelia close to the orbit of Jupiter (~ 5 AU) could evolve into short-period orbits. As in van Woerkom’s work, the efficiency of the process was too low. Besides, neither Everhart nor van Woerkom could convincingly explain the preponderance of prograde orbits among short-period comets.

Alongside the question of the origin of the short-period comets, there remained the issue of the origin of comets altogether: of where they formed. Theories of a possible interstellar origin had been dismissed by van Woerkom (1948) on the basis that no comet had ever been found to have a hyperbolic orbit. Comets must have formed in the Solar System. Important clues to the origin of comets came from the work of Fred Whipple. He presented a model of the chemical composition of comets (Whipple 1950) consisting mainly of ices of H_2O , NH_3 , CH_4 , CO_2 , CO , and other volatiles, “polluted” by smaller amounts of refractory⁵ material in the form of dust. This model, popularized by Whipple as “dirty snowball”, explained the tails and comæ⁶ of comets upon approaching the Sun. Due to the temperature increase, the icy material sublimates and becomes partly ionized—forming the coma and ion tail—and forces solid particles off the surfaces of comets, which form the dust tail.

⁴An astronomical unit (AU) is the mean distance between the Sun and the Earth.

⁵Material with a higher (melting) sublimation temperature, here meant to signify rocky (silicate based) material.

⁶Comets usually show an ion (gas) tail pointing away from the Sun, a dust tail slightly trailing the ion tail, and a luminous halo (coma) surrounding the nucleus (central solid part).

Partly motivated by Whipple’s model, Kuiper (1951) proposed that comets could have formed in the outer solar system, between 35 and 50 AU. Gerard Kuiper was born in the Netherlands in 1905. He studied astronomy in Leiden, where he got his PhD degree in 1933, with a dissertation on binary stars. He immediately moved to the USA to pursue his studies of multiple star systems. Later he switched to solar system science, which became his main field of research. Kuiper contributed significantly to the development of planetary science, both theoretically and observationally. He died in 1973.

Kuiper realized that the volatile-rich composition of comets (as opposed to the more “rocky” asteroids) was inconsistent with their forming in the inner region of the solar system. Therefore, Kuiper believed that comets must have formed far from the Sun. The “nebular model”⁷ for the formation of the solar system does not invalidate the formation of “condensations” beyond the orbits of the known planets. As Kuiper argued, by forming far from the Sun, such condensations would be smaller and more numerous, due to the lower density of material, and made up mostly of ices (as Whipple proposed) because of the very low temperatures. Nevertheless, Kuiper intended to explain the formation of Oort cloud comets, not short-period comets. Since it is unlikely that there was enough material at distances $\sim 100\,000$ AU from the Sun to support *in situ* formation of Oort cloud comets, Kuiper speculated that comets must have formed much closer to the Sun—at about 40 AU. A substantial fraction was scattered outwards and populated the Oort cloud. Kuiper did not question the idea that short-period comets were dynamical descendants of long-period comets.

Shortly before Kuiper’s 1951 paper, Kenneth Edgeworth (1880–1972) speculated on the possibility that the outer solar system was occupied by a ring of small bodies, in his own words, “a vast reservoir of potential comets” (Edgeworth 1949). During his professional career, Edgeworth was an army officer, electrical engineer, and economist, and only in his retirement years, at the age of 59, began actively working as an independent theoretical astronomer (McFarland 1996).

Already in 1943, in a paper communicated to the British Astronomical Association, Edgeworth (1943) mentioned that it would be unthinkable that the cloud from which the solar system formed would be bounded by the orbit of Pluto. Instead he proposed, and later supported with theoretical calculations (Edgeworth 1949), a “gradual thinning” of the cloud at greater and greater distances from the Sun; this thinner (less dense) cloud would support the formation of small bodies. Therefore, outside the orbits of Neptune and Pluto there should exist a swarm of small bodies. Edgeworth thought that bodies in this swarm that got displaced into the inner solar system (no mechanism is suggested for this displacement) would become the visible comets. Edgeworth (1943) further

⁷Originally proposed by Kant (1755) and Laplace (1796), this model supports that the Sun, the planets, and all the other solar system bodies formed from the gravitational collapse of a single cloud (nebula) of gas and dust. It has obtained strong observational support in recent years, and is widely accepted as the most plausible model of formation of planetary systems.

speculated that comets, unlike asteroids, are probably “astronomical heaps of grains with low cohesion”, due to the low formation temperatures; this is very close to what is known today about the structure of comets. Edgeworth’s work in astronomy was rarely cited by his contemporaries (including Kuiper). This has been attributed to his “brusque style of presentation” (McFarland 1996). On the other hand, at a time when information flowed slower than today, being an outsider to the astronomical community (Edgeworth was not affiliated to any research institution) may have contributed to his work remaining unnoticed.

The lack of observational evidence kept the idea of a “comet belt” at the edge of the solar system in the realm of speculation. Indeed, further (indirect) evidence for the need of such a belt came from theoretical calculations in the 1980s. Earlier work by Joss (1973) had reinforced the idea that the capture mechanism of long-period comets into short-period comets by the giant planets was inefficient. In 1980, Julio Fernández presented results of a Monte Carlo simulation confirming that comets coming from a hypothetical belt beyond Neptune could produce the observed distribution of short-period comets (Fernandez 1980). Decisive results came nearly a decade later from extensive numerical simulations by Martin Duncan, Thomas Quinn, and Scott Tremaine. Their calculations convincingly ruled out that short-period comets could originate in a spherically symmetric population such as the Oort cloud. The prograde low-inclination orbits of short-period comets could only be explained if the parent population had a similar orbital distribution, most likely located in the outer solar system (Duncan et al. 1988). The authors referred to this parent population as “Kuiper belt”, acknowledging the hunch of Gerard Kuiper.

Around the same time, sensitive charge-coupled devices (CCDs, electronic detectors) began replacing photographic plates, as means of registering the light collected by telescopes. Among many other advantages, such as linearity and reusability, CCDs are more sensitive than photographic plates, and allow ready analysis of the collected data using computers. Making use of this new technology, installed at the 2.2 m UH⁸ telescope atop Mauna Kea (Hawaii), David Jewitt and Jane Luu began a survey⁹ of the outer solar system looking for “slow moving objects”. Expected to lie beyond Neptune, the hypothetical Kuiper belt objects would take about 250 years to complete a full orbit around the Sun. This means they must move very slowly against the background stars. Actually, their apparent movement with respect to the stars is primarily due to the movement of the Earth around the Sun¹⁰. Therefore, if Jewitt and Luu could identify faint slow moving objects, they would likely be located deep in the outer solar system.

⁸University of Hawaii, USA.

⁹Jewitt and Luu actually began the survey in 1987 using photographic plates, but soon switched to the more sensitive CCDs.

¹⁰Much like the movement of a cow against a background windmill, as seen from a moving car on a Dutch highway, is due mostly to the movement of the car and not to the movement of the cow.

In the summer of 1992, after 5 years of persevering, Jewitt and Luu detected a faint object that seemed to move at the expected pace in four consecutive images. Accurate measurements of the object's positions were used to determine its orbit: a nearly circular path, at a distance of 40 AU from the Sun. Following the naming convention of the Minor Planet Center¹¹ (MPC), this object was designated 1992 QB₁. It was the first detection (Jewitt & Luu 1993) of an object with an orbit entirely outside that of Neptune: a “Kuiper belt object”. 1992 QB₁ was estimated to have a diameter of about 200 km. About six months later—when the Earth is on the “other side” of the Sun—Jewitt and Luu found another object, equally beyond Neptune. Since then, nearly 1000 Kuiper belt objects have been discovered, confirming the predictions of Kuiper, Edgeworth, and others.

The discovery of the Kuiper belt raised doubts about Pluto's classification as planet. When Clyde Tombaugh discovered Pluto, in early 1930, he was on a mission to find the planet which was causing perturbations measured in Neptune's orbit¹². Tombaugh found an object, and the object was classified as planet. But Pluto was odd in the context of the outer solar system: it is icy and small, unlike the outer large gaseous planets, and it has a very elliptical and inclined orbit. In an inspired—almost prophetic—leaflet of the Astronomical Society of the Pacific published a few months after Pluto's discovery, Leonard (1930) wrote:

“... We know that the Sun's gravitational sphere of control extends far beyond the orbit of Pluto. Now that a body of the evident dimensions and mass of Pluto has been revealed, is there any reason to suppose that there are not other, probably similarly constituted, members revolving around the Sun outside of the orbit of Neptune? Indeed, it may ultimately be found that the solar system consists of a number of zones, or families, of planets, one with the other. As a matter of fact, astronomers have recognized for more than a century that this system is composed successively of the families of the terrestrial planets, the minor planets, and the giant planets. Is it not likely that in Pluto there has come to light the *first* of a *series* of ultra-Neptunian bodies, the remaining members of which still await discovery but which are destined eventually to be detected? ...”

Leonard guessed right. Pluto is the largest known member of the recently discovered family of “ultra-Neptunian” bodies. Besides being the likely precursors of comets, Kuiper belt objects are believed to be remnants of outer solar system planetesimals¹³. Frozen at the distant edge of the planetary system, they preserve information about the environment in which the planets formed. The discovery of the Kuiper belt has helped understand the origins of Pluto and the short-period comets. But, as is usually the case in science, it has raised a multi-

¹¹<http://cfa-www.harvard.edu/iau/mpc.html>

¹²It was later discovered that the observed perturbations in the orbit of Neptune were actually measurement errors.

¹³First aggregates of solid material that merged to form the planets.

tude of new questions, thereby opening an entirely new field of research. Observationally speaking, Kuiper belt science is extremely challenging. The brightness of KBOs, due to reflected sunlight, is inversely proportional to roughly the fourth power of their distance to the Earth. At 40 AU most KBOs are too faint ($\langle m_R \rangle \sim 23$, Trujillo et al. 2001b), and only the largest are accessible to detailed analysis. Although it is expected that Kuiper belt studies will provide invaluable information about the history of our planetary system, and even of planetary systems around other stars, it might take a while before that information can be gathered and decoded. The process will eventually require spacecraft to be sent to individual Kuiper belt objects. And that, to the joy of the “curious beings”, will certainly reveal new surprises begging for an explanation.

The belt and its population of objects still have no unanimously accepted name. In the first key publications (Duncan et al. 1988; Jewitt & Luu 1993) it was referred to as “Kuiper belt”, and most astronomers use this name. The most frequently used alternative is the self-explanatory “Trans-Neptunian belt”. Some attempts have been made to acknowledge Edgeworth’s contribution, and use “Edgeworth-Kuiper belt”, but the name is not used very often. Therefore, in the literature all of the following acronyms are found: KB and KBOs, TNB and TNOs, and EKB and EKO. In this thesis the names Kuiper belt (KB) and Kuiper belt objects (KBOs) will be used.

1.2 The Kuiper belt

The bulk of the Kuiper belt is located beyond the orbit of Neptune, between 30 and 50 astronomical units from the Sun (see Fig. 1.2). The orbit of Neptune is, by definition, the lower limit to the semi-major axis of the orbits of Kuiper belt objects; there is no defined upper limit. The belt extends roughly 25 AU above and below the ecliptic (see Fig. 1.3). All known KBOs orbit the Sun in the prograde sense. Although most objects follow this regular merry-go-round pattern, some KBOs have very eccentric and inclined orbits, and only rarely visit the central region of the belt. These “scattered” objects reach heliocentric distances of several hundreds of AU.

According to the MPC, almost 1000 KBOs have been detected¹⁴. However, reliable orbits have only been determined for about half of them. Figure 1.4 shows that the distribution of KBO orbits is not random. The apparent structure has led to a classification of KBOs into 3 dynamically distinct groups: the *Classical KBOs*, the *Resonant KBOs*, and the *Scattered KBOs*. Table 1.1 lists the number and mean orbital properties of KBOs belonging to each of these dynamical groups. Only those objects that have been observed for more than one opposition have been considered. Table 1.1 also shows the number of observed *Centaurs*. The main characteristics of these different groups are given below.

¹⁴<http://cfa-www.harvard.edu/iau/lists/TNOs.html> and [Centaurs.html](http://cfa-www.harvard.edu/iau/lists/Centaurs.html)

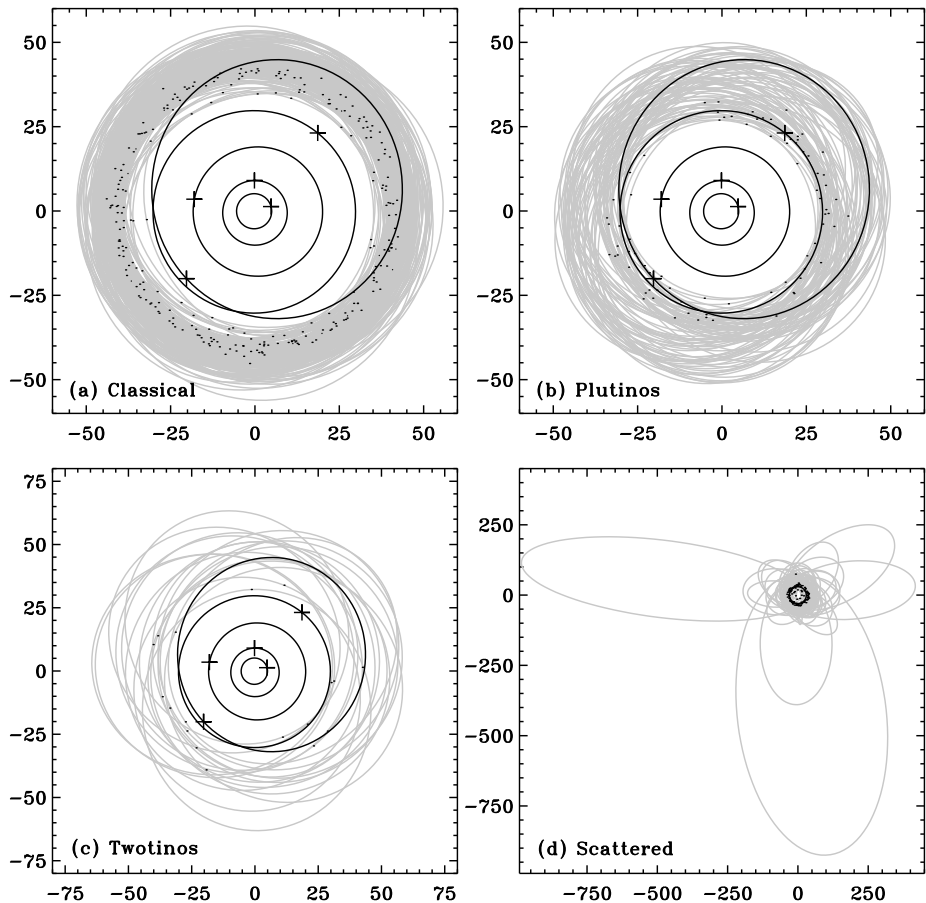


Figure 1.2 – Plan view of the orbits of Kuiper belt objects (grey ellipses). Different dynamical groups are shown in separate panels. The orbits of Jupiter, Saturn, Uranus, Neptune, and Pluto are also shown (black ellipses). Black dots (KBOs) and crosses mark the perihelia of all orbits. The axes are in AU.

Classical KBOs

Making more than half of the known population, the Classical KBOs are the prototypical group. The first KBO to be discovered, 1992 QB₁, is a Classical object. CKBOs are selected to have perihelia $q > 35$ AU and orbital semi-major axis $42 \text{ AU} < a < 48 \text{ AU}$ (see Figs. 1.2, 1.3, and 1.4). Most have nearly circular ($e < 0.2$) and moderately inclined orbits ($i < 10^\circ$). There is, however, a small fraction of CKBOs reaching orbital inclinations $i \sim 30^\circ$. The intrinsic fraction of CKBOs with inclined orbits may be larger than what is measured, because of the observational bias towards detecting low- i objects. Numerical simulations have shown that orbits with $q > 42$ and $e < 0.1$ are stable for the age of the solar

Figure 1.3 – Same as Fig. 1.2 but seen from the side. Axes are in AU.

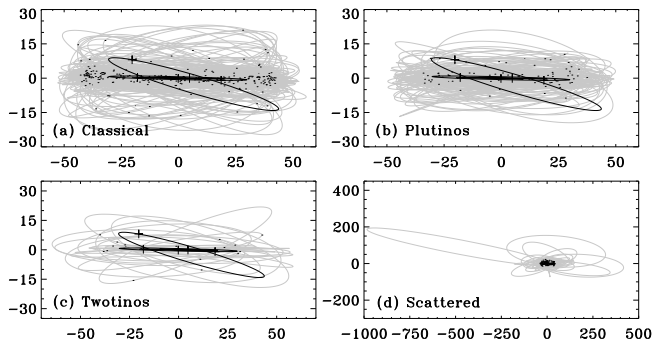


Table 1.1 – Number and orbital parameters of KBOs and Centaurs.

Dynamical group	N	f_{obs}^*	f_{int}^{**}	a [AU]	$\langle e \rangle$	$\langle i \rangle$ [deg]
Classical KBOs	267	0.57	0.44	42 ··· 48	0.08	5.3
Resonant KBOs						
Plutinos (3:2)	79	0.17	0.18	~39.4	0.21	9.2
Twotinos (2:1)	18	0.04	0.03	~47.8	0.23	10.0
4:3 resonance	4	0.01	–	~36.4	0.15	10.1
Scattered KBOs	101	0.22	0.35	$> \frac{30}{1-e}$	0.33	14.6
Centaurs	47			$< \frac{30}{1-e}$	0.35	12.7
Total (KBOs)	469	1.00	1.00		0.17	8.3

The data was obtained from the MPC website. Only objects observed for more than one opposition have been considered.

* Fraction of observed KBOs;

** Bias-corrected estimate of the intrinsic fraction (Trujillo et al. 2001a).

system (Duncan et al. 1995). Because of their stable dynamical configuration, the Classical objects are thought to best represent the primordial population.

Resonant KBOs

These objects lie close to mean motion resonances with Neptune. This means that the quotient of the orbital period of a Resonant KBO and that of Neptune is a ratio of integers. The 3:2 resonance, harbouring ~80% of the observed Resonants, is the most populated. Bodies lying in the 3:2 resonance are called *Plutinos*, because Pluto itself lies in this resonance. The second most populated resonance is the 2:1, containing ~20% of all Resonant KBOs. The 2:1 Resonants have lately been called *Twotinos* (Chiang & Jordan 2002). Four objects have been observed close to the 4:3 resonance. Some Resonants, including Pluto, have perihelia¹⁵ inside the orbit of Neptune (see Figs. 1.2 & 1.4). However, the resonant character of their orbits prevents close encounters. Resonant orbits are also dynamically stable on Gyr timescales (Duncan et al. 1995). The overabundance

¹⁵Point of closest approach to the Sun, usually represented by q .

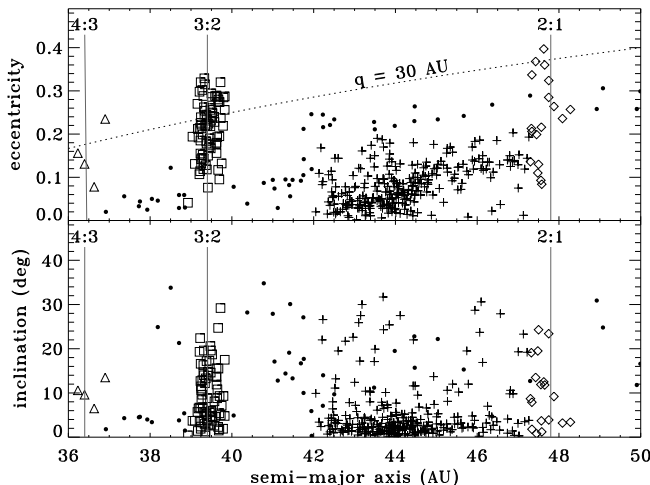


Figure 1.4 – Orbital eccentricity and inclination versus semi-major axis of KBOs. Symbols are: (+) Classical KBOs, (□) Plutinos, (◇) Twotinos, (△) 4:3 Resonant KBOs, (·) Scattered KBOs. Gray vertical lines indicate the mean motion resonances with Neptune. Constant perihelion $q = 30$ AU (orbit of Neptune) is shown as a dotted curve.

of Plutinos is understood as evidence of planetary migration (Malhotra 1993, 1995). It is possible that Neptune formed closer to the Sun and migrated outwards to its current location, due to angular momentum exchange with surrounding planetesimals (Fernandez & Ip 1984). As the planet migrated, its mean motion resonances swept through the KB region. Because resonances are more stable they “captured” KBOs, as they swept by. Simulations show that an outward migration of ~ 8 AU on a timescale $\tau \sim 10^7$ yr produces the observed distribution of eccentricities and inclinations of Plutinos (Malhotra 1998; Gomes 2000).

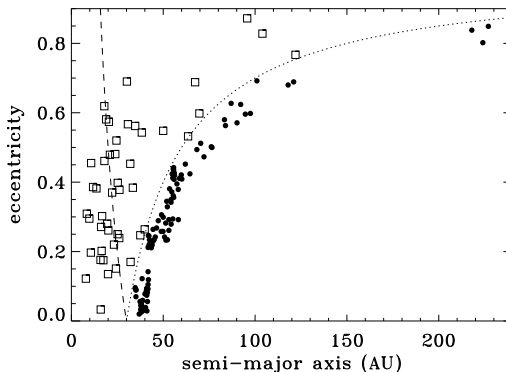
Scattered KBOs

Sometimes referred to as Scattered Disk objects (SDOs), these KBOs have more eccentric and inclined orbits than the previous two groups. Due to the large ellipticity of their orbits, some SKBOs spend many Earth centuries outside the KB region, at large distances from the Sun (see Fig. 1.2). Figure 1.5 shows the orbital distribution of SKBOs. By definition, SKBOs have perihelia $q > 30$ AU (below the dotted line in Fig. 1.5). The reason why all the observed objects actually have perihelia close to $q = 30$ AU is that objects with larger q are very hard to detect. Given the nature of their orbits, SKBOs may represent an intermediate stage between KBOs and Oort cloud objects.

Centaurs

The Centaurs have perihelia between the orbits of Jupiter and Neptune—they are sometimes referred to as giant planet crossers. Centaurs are not KBOs: they are believed to be dynamical transients between KBOs and short-period comets. The short dynamical lifetimes (1–100 Myr) of Centaur orbits, when compared to the age of the solar system, implies that the population must be resupplied on comparable timescales; the most likely source is the KB. Recent numerical simulations by Tiscareno & Malhotra (2003) show that, due to dynamical inter-

Figure 1.5 – Same as Fig. 1.4 for a broader range of semi-major axes, to show the distribution of Scattered KBOs (filled circles) and Centaurs (open squares). Curves represent constant perihelion $q = 30$ AU (dotted) and constant aphelion $Q = 30$ AU (dashed).



actions with the giant planets, 2/3 of the population is ejected from the solar system (or enters the Oort cloud), 1/3 become Jupiter Family¹⁶ comets, and a negligible fraction collides with a giant planet. As our understanding of the structure of KB orbits improves, better simulations of the transition of KBOs into short-period comets are needed to clarify the role of Centaurs.

1.3 Kuiper belt objects

One thing people always ask, when told about KBOs for the first time is: how big are they? The answer is: we don't know. KBOs are not observationally resolved¹⁷, so their sizes cannot be measured directly. Basic information about KBOs, such as their sizes and masses, relies on two quantities that are not known: albedo¹⁸ and density. Since KBOs are believed to be progenitors of short-period comets, these properties are taken to be similar in both families. As short-period comets, KBOs are expected to have low albedos ($A \sim 0.04$) and densities close to water ice ($\rho \sim 1000 \text{ kg m}^{-3}$). With these assumptions, the observational data can be used to infer, for example, the total number of KBOs, their size distribution, and the total mass present in the Kuiper belt.

The observed cumulative surface density of KBOs (number of objects per square degree brighter than a given magnitude) is well fit by an exponential power law of the form $\Sigma(m_R) = \exp[\alpha(m_R - m_0)]$. The best fit parameters, $\alpha \approx 0.6$ and $m_0 \approx 23$ mag (Trujillo et al. 2001a; Bernstein et al. 2004), indicate that 1 KBOs of magnitude 23 can be found per square degree; the number is 4 times higher at each fainter magnitude. The observed cumulative surface density can be used to infer the size distribution. Assuming the latter can be represented by a power law, $n(r) dr \propto r^{-q}$, the best estimate index is $q \approx 4$ (Trujillo et al. 2001a). Note that a different q was used before, to represent perihelion distance.

¹⁶Short-period comets that have periods $P < 20$ yr and orbits dominated by Jupiter's gravity.

¹⁷Except the 2 largest known, Pluto and (50000) Quaoar, which have been resolved by HST.

¹⁸The albedo (A) of an object is the fraction (between 0 and 1) of sunlight it reflects.

Recent, deeper observations show that the size distribution may be shallower ($q = 3.0\text{--}3.5$) at radii below $r = 10\text{--}100$ km (Bernstein et al. 2004). This size distribution implies that there are roughly 10 000 KBOs with radii larger than $r = 100$ km, and about 10 Pluto-size objects ($r \sim 1000$ km). Assuming individual body densities $\rho \sim 1000 \text{ kg m}^{-3}$ the total mass of KBOs between 30 AU and 50 AU is $M_{\text{KB}} = 0.01\text{--}0.1 M_{\oplus}$, where $M_{\oplus} = 6 \times 10^{24}$ kg is the mass of the Earth.

These measurements agree well with what is predicted by current KBO formation and evolution scenarios; a few examples are cited below. The “minimum mass solar nebula” (Hayashi 1981; Weidenschilling 1977) estimate of the mass initially¹⁹ present in the KB region is $10 M_{\oplus}$, 100 to 1000 times higher than what is observed. Numerical simulations of KBO accretion show that if this was indeed the initial mass then several “Plutos” can form in less than 100 Myr (Kenyon & Luu 1998, 1999). The same simulations produce a power law KBO size distribution of index $q \sim 3.5$, at the end of the 100 Myr accretional phase. Subsequently, erosive collisions between KBOs convert bodies with $r \lesssim 100$ km into smaller and smaller fragments, some of which may plunge into the inner solar system as short-period comets (Davis & Farinella 1997). This collisional cascade produces the observed break in the size distribution at $r \sim 10\text{--}100$ km (Kenyon & Bromley 2004). A substantial amount of mass is converted to $1\text{--}100 \mu\text{m}$ -size dust grains, which are blown away from the solar system by solar radiation in a few tens of million years (Burns et al. 1979; Barge & Pellat 1990). These processes are believed to have caused the mass depletion ($\sim 99\%$) in the Kuiper belt. The data also indicate that the KB population is large enough to serve as source of short-period comets. The observed size distribution predicts that there are 10^{10} KBOs larger than 1 km in radius—enough to account for the observed short-period comet population (Holman & Wisdom 1993; Levison & Duncan 1997).

KBO albedos can be determined using combined observations in visible and thermal (infrared) wavelengths. The amount of sunlight reflected by a KBO is roughly proportional to the product of albedo and cross-section, $A \times S$. Conversely, the fraction of sunlight absorbed by the KBO, which maintains its temperature and is re-emitted at longer (infrared) wavelengths, is proportional to $(1 - A) \times S$. Measurements in both wavelength ranges permit the determination of both A and S . At about 40 AU from the Sun, KBOs have surface temperatures of about 50 K. This means their thermal emission peaks at infrared wavelengths, around $50 \mu\text{m}$. Unfortunately the atmosphere is not transparent at these wavelengths. As a result only the brightest (largest) KBOs can have their thermal radiation measured from Earth. Observations from space do not suffer from atmospheric extinction. Table 1.2 lists the KBOs with known albedos. The measurements by Thomas et al. (2000) have been done from space, using ISO²⁰, and the size of (50000) Quaoar was measured directly using the High Resolution Camera of the Hubble Space Telescope. Indeed, KBO albedos seem to be very

¹⁹About 4.5 Gyr ago, when the solar system formed.

²⁰Infrared Space Observatory

Table 1.2 – KBOs with measured albedo.

Object	Albedo	r [km]	Reference
Pluto	0.44–0.61	1150	Stern & Yelle (1999)
(50000) Quaoar	0.09	630	Brown & Trujillo (2004)
(20000) Varuna	0.07	450	Jewitt et al. (2001)
1999 TL ₆₆	0.03	320	Thomas et al. (2000)
1993 SC	0.02	160	Thomas et al. (2000)

low, close to that of short-period comets. Pluto’s extremely high reflectivity is an exception. The accepted explanation is that Pluto is massive enough to hold a very thin atmosphere, which can condense on the surface creating a reflective frost layer. Recently reported observations made with the Spitzer Space Telescope appear to indicate that KBOs may have higher albedos than expected (Emery et al. 2004). These results are still unpublished.

The chemical compositions of KBOs is poorly known. Even for the largest KBOs, spectroscopic studies are extremely difficult, due to low signal-to-noise. For this reason, broadband colours are generally used as a low resolution alternative. KBOs, as a population, have very diverse colours, from blue to very red (Luu & Jewitt 1996; Jewitt & Luu 1998; Tegler & Romanishin 2000). Statistical studies show that KBO colours may correlate with orbital inclinations and perihelion distances (e.g., Jewitt & Luu 2001; Doressoundiram et al. 2002; Trujillo & Brown 2002). Different dynamical groups appear to have distinct colour distributions (Peixinho et al. 2004). The underlying reasons for these trends are not understood. Comparison between the colours of KBOs and short-period comets show that the former are redder on average than the latter (Jewitt 2002). This suggests that comet surfaces have been modified somewhere along the transition from the KB to their current orbits.

The few existing spectra (optical and near-IR) of KBOs are mostly featureless, although some show a weak $2\mu\text{m}$ water ice absorption line (Brown et al. 1999; Jewitt & Luu 2001). Very recent near-infrared spectroscopic observations of the largest (besides Pluto) known KBO, (50000) Quaoar, have revealed the presence of water ice with crystalline structure (Jewitt & Luu 2004). This means the ice (usually at $\sim 50\text{K}$) must have been heated to 110K . What makes this finding a puzzle is that, since cosmic radiation destroys the ice molecular bonds and turns it into amorphous ice in about 10^7yr (Strazzulla et al. 1991), the surface of Quaoar must have somehow been heated in the last 10 million years.

Direct observations of binary KBOs indicate that they may represent about 4% of the known population (Veillet et al. 2002; Noll et al. 2002). The Pluto-Charon system is an example of a long known binary KBO. The observed binaries have separations $\delta > 0''.15$, and primary-to-secondary mass ratios close to unity. Existing models of binary KBO formation require a ~ 100 times denser environ-

ment than the present, implying that the binaries must have formed early in the evolution of the KB (Weidenschilling 2002; Goldreich et al. 2002). Recently, the discovery of a contact (or very close) binary KBO has been reported (Sheppard & Jewitt 2004). The authors estimate that the fraction of similar objects in the Belt may be $\sim 15\%$.

The spin states of KBOs can be determined from their “lightcurves”. The lightcurves are periodical brightness oscillations produced by the varying aspect of non-spherical KBOs, as they spin. Spherical KBOs, or those whose spin axis coincides with the line-of-sight, show nearly constant brightness (or “flat” lightcurves), because their sunlight reflecting area is constant in time. The period of a KBO lightcurve is a direct measure of the KBO’s spin period, and the lightcurve peak-to-peak amplitude has information about the shape of the object. The spin rates of KBOs also place constraints on their bulk densities. In bodies with no internal strength, the centrifugal acceleration due to rotation must be balanced by self-gravity, or the body would “fly apart”. Thus by measuring the spin rate of a KBO we find a lower limit to its bulk density. The shapes and spins of KBOs potentially carry information about their formation environment, and their evolution. For example, the larger objects should retain the angular momentum acquired at formation, while smaller bodies have probably had their spins and shapes modified by mutual collisions in the last ~ 4.5 Gyr.

Rotational data have been used in the past to investigate the evolution and the physical properties of other minor planets (e.g., asteroids). In the case of KBOs, such data have only recently become available, although still in meager amounts. The small brightness variations (typically a few tenths of magnitude) are difficult to measure for KBOs, and require large collecting areas (large telescopes). Besides, the long timebases needed to accurately determine the periodicity of the variations, are not readily available in the competitive world of time allocation for usage of large telescopes. Approximately 4.5 years ago, when the project that led to this thesis started, rotational data had been reported for 10 KBOs. We set out to increase that number, and to use the rotational properties of KBOs to learn more about their nature. Now, as a combined result of different observational campaigns (Sheppard & Jewitt 2002; Sheppard & Jewitt 2003; this work), the number of KBO lightcurves is 4 times larger. In this thesis, the existing rotational data of KBOs are used to investigate some of their physical properties.

1.4 Thesis summary

My thesis uses rotational data of KBOs to investigate their shapes, spins, and inner structure. The rotational properties were obtained from analysis of KBO “lightcurves”. The lightcurves are periodic brightness variations mainly due to the aspherical shapes of KBOs—as aspherical KBOs spin in space their sky-projected cross-sections vary periodically, and so does the amount of reflected

sunlight. The period of a lightcurve is related to the spin period of the KBO that produces it, and the amplitude of the light variation has information on the KBO's shape.

Most KBOs (about 70%) actually show no brightness variations. This can be because they are not spinning (or spin very slowly), because they are spherical, or because the spin axis points directly at the observer. In **Chapter 2**, the likelihood of these and other possibilities is discussed, and presented in the form of a statistical study of the detectability of lightcurves of KBOs. As a result, an expression is derived that gives the probability of detecting light variations from a KBO, assuming an a priori shape distribution for the whole population. This expression can test candidate shape distributions by checking if they reproduce the observed detection probability, i.e., the fraction of observed KBOs that show detectable variations.

In **Chapter 3**, the method developed in Chapter 2 is used to test two possible functional forms for the KBO shape distribution: gaussian and power-law. The (then) existing database of KBO lightcurves is used to determine the fraction that have detectable light variations. The results show that a power-law shape distribution gives a better fit to the data. However, a single power-law distribution does not explain the shapes of the whole population.

Chapter 4 presents our observations of KBO lightcurves. We collected data for 10 KBOs, 5 of which had not been studied before. Significant light variations were detected for 3 out of the 10 objects. The periods and amplitudes of the lightcurves were determined, and combined with the existing database of rotational properties. After adding our observations, lightcurve data exist for a total of 41 KBOs. Using the conclusions of Chapter 3, we used this data to better constrain the KBO shape distribution. KBOs were split in two groups, with diameter smaller and larger than $D = 400$ km, which were analysed separately. We find that the shapes of bodies are different in the two groups. The larger group has a higher fraction of round bodies. A comparison between KBOs and asteroids shows that KBOs are rounder than asteroids. In the case of asteroids it has been shown that the ones with diameter $D < 100$ km have shapes consistent with collisional fragments. The smallest KBO with a measured lightcurve has a diameter $D = 100$ km, so we are still far from being able to compare KBOs and asteroids in small size ranges. The rotational data were also used to investigate the inner structure of KBOs. Large KBOs have in principle survived the collisional evolution, but may have been internally fractured by multiple impacts, and turned into agglomerates of smaller pieces held together mainly by gravity. If this is true then their shapes are mostly controlled by a balance between gravitational and centrifugal acceleration. In the case of uniform fluids, the shape of a rotating body depends on the spin rate and on the body's density. We compare a diagram KBO spin rates vs. lightcurve amplitudes with what is expected in the case of perfect fluid behaviour, and with results of N-body simulations of collisions between ideal "rubble piles". The results are not conclusive but most

KBOs are at least consistent with having a rubble pile structure and densities $\rho > 1000 \text{ kg m}^{-3}$.

In **Chapter 5** we investigate how collisions between KBOs have affected their spins. A model is constructed to simulate the collisional evolution of KBO spins, in the last 4 Gyr (Note: the best models of KBO formation indicate the bulk of the population was formed in about 100 Myr). Each simulation follows a single KBO and calculates the spin rate change and mass change due to each individual collision. These changes depend on several parameters, which are tested. Among other things, we find that the spin rates of KBOs with radii larger than about $r = 200 \text{ km}$, have not been changed by collisions—their spin must be “primordial”. The lightcurve data presented in Chapter 4 show that 4 out of 7 KBOs with $r \sim 500 \text{ km}$ spin with periods of about 15 hours. This raises the question: what is the origin of the spins of these large KBOs? If these objects grew by isotropically accreting material, angular momentum conservation should significantly slow down their spin rates. We estimate how anisotropic does the accretion need to be to explain the rotation of the large KBOs. It turns out that an asymmetry of about 10% in the angular momentum contributed by the accreted particles is enough. But we also found that this is only necessary if the accreted particles are very small. If they are at least 1/5 of the size of the growing body, then isotropic accretion can also reproduce the observed spins. The distribution of spins predicted by these two possibilities is very different. If KBOs grew from isotropic accretion of large particles, the dispersion of spin rates should be large, and the spin axes should be randomly oriented. On the other hand, if KBOs grew by anisotropically accreting small particles, the dispersion in spin rates should be small, and if this asymmetry exists primarily in the ecliptic plane then the spin axis of large KBOs would tend to be aligned perpendicularly to the plane, like most planetary axes. Measurements of the distribution of spin axis orientations of large KBOs can in principle rule out one of the possibilities.

1.5 Future prospects

Chapter 2 was written before good constraints existed on the fraction of binary KBOs. As more binaries are discovered and the statistics of, for example, primary-to-secondary size ratios and distance between the two components improves, it becomes possible to account for the probability that a lightcurve is due to an eclipsing binary. This should be incorporated in the method developed in the chapter.

It would be extremely useful to construct an “atlas” of lightcurves. The morphology of a lightcurve reflects the cause of the brightness variation. The recovery of the cause from the analysis of the morphology is known as lightcurve inversion. Although the problem of lightcurve inversion is known to be degenerate (Russell 1906), the importance of understanding the morphology of lightcurves caused by different physical situations cannot be denied. Using ray-

tracing software, a host of different physical situations (KBOs of various shapes, close tidally deformed binaries, objects with surface features, etc.) can be created, “observed”, and used to systematically generate a database of lightcurve properties. The lightcurves can be analysed in terms of Fourier expansions, to look for structure in the distribution of the coefficients.

As described in Chapter 4 (§4.5.2), KBOs are more spherical on average than asteroids. Yanagisawa (2002) has investigated the transfer of angular momentum by collisions, for spherical as well as ellipsoidal targets. The author calculated the ratio between the spin-up rate (angular momentum transferred divided by the moment of inertia of the target) of ellipsoidal targets and the spin-up rate of spherical targets of the same mass, and concluded that ellipsoidal bodies can spin up more rapidly than spherical bodies. If this is true, one would expect a population of rounder objects to have lower spin rates than a population of more elongated objects, if both have similar collisional evolution histories. The different shape distributions of KBOs and asteroids could partially justify their different mean spin rates. A natural extension to the collisional evolution model presented in Chapter 5 is to consider targets and projectiles with ellipsoidal shapes, and see how this affects the results.

It is shown in Chapter 5 that the distribution of spin periods of the largest KBOs is likely to be primordial. If the spins have been caused by accretion of large planetesimals (comparable, in size, with the growing body) then the observed distribution of spin periods can constrain the size distribution of the accreting planetesimals. In Chapter 5 only the simple case where all accreted planetesimals have a fixed size—function of the size of the growing object—was considered. More realistic scenarios allowing for a range of accreted planetesimal sizes should be investigated. The results may serve as an independent check on the planetesimal size distribution obtained from models of accretion in the KB (Kenyon & Luu 1998, 1999).

In Chapter 5 the possibility is considered that the rotations of the largest KBOs were caused by a torque due to the accreted material. It would be interesting to investigate if the dynamics of the particles being accreted into a large KBO, as it grows in a swarm of smaller planetesimals, can produce such a torque. This can be done by means of an N-body simulation.

It is essential to increase the database of KBO rotational properties, for various reasons. With better statistics it will be possible to compare the shapes and spin states of KBOs in different dynamical groups. The comparison may serve as a check for different evolution scenarios.

References

- Barge, P. & Pellat, R. 1990, *Icarus*, 85, 481
- Bernstein, G. M., Trilling, D. E., Allen, R. L., Brown, M. E., Holman, M., & Malhotra, R. 2004, *AJ*, 128, 1364
- Brown, R. H., Cruikshank, D. P., & Pendleton, Y. 1999, *ApJ*, 519, L101
- Brown, M. E. & Trujillo, C. A. 2004, *AJ*, 127, 2413
- Burns, J. A., Lamy, P. L., & Soter, S. 1979, *Icarus*, 40, 1
- Chiang, E. I. & Jordan, A. B. 2002, *AJ*, 124, 3430
- Davis, D. R. & Farinella, P. 1997, *Icarus*, 125, 50
- Doressoundiram, A., Peixinho, N., de Bergh, C., Fornasier, S., Thébault, P., Barucci, M. A., & Veillet, C. 2002, *AJ*, 124, 2279
- Duncan, M., Quinn, T., & Tremaine, S. 1988, *ApJ*, 328, L69
- Duncan, M. J., Levison, H. F., & Budd, S. M. 1995, *AJ*, 110, 3073
- Edgeworth, K. E. 1943, *Journal of the British Astronomical Association*, 53, 181
- Edgeworth, K. E. 1949, *MNRAS*, 109, 600
- Emery, J. P., Cruikshank, D. P., Van Cleve, J., & Stansberry, J. A. 2004, *AAS/Division for Planetary Sciences Meeting Abstracts*, 36,
- Everhart, E. 1972, *Astrophys. Lett.*, 10, 131
- Everhart, E. 1973, *AJ*, 78, 329
- Everhart, E. 1977, *IAU Colloq. 39: Comets, Asteroids, Meteorites: Interrelations, Evolution and Origins*, 99
- Fernandez, J. A. 1980, *MNRAS*, 192, 481
- Fernandez, J. A. & Ip, W.-H. 1984, *Icarus*, 58, 109
- Gomes, R. S. 2000, *AJ*, 120, 2695
- Goldreich, P., Lithwick, Y., & Sari, R. 2002, *Nature*, 420, 643
- Halley, E. 1705, *A Synopsis of the Astronomy of Comets*, Johnson Reprint Corp. New York, 1972 ,
- Hayashi, C. 1981, *Progress of Theoretical Physics Supplement*, 70, 35
- Holman, M. J. & Wisdom, J. 1993, *AJ*, 105, 1987
- Jewitt, D. C. 2002, *AJ*, 123, 1039
- Jewitt, D., Aussen, H., & Evans, A. 2001, *Nature*, 411, 446
- Jewitt, D. & Luu, J. 1993, *Nature*, 362, 730
- Jewitt, D. & Luu, J. 1998, *AJ*, 115, 1667
- . 2001, *AJ*, 122, 2099
- Jewitt, D. & Luu, J. 2004, *Nature*, 432, 731
- Joss, P. C. 1973, *A&A*, 25, 271
- Kepler, J., Ptolemaeus, C., & Fludd, R. 1619, *Lincii Austriae, sumptibus G. Tampachii, excudebat I. Plancvs*, 1619.,
- Kant, I. 1755, *Allgemeine Naturgeschichte und Theorie des Himmels* (Leipzig: Petersen)
- Kenyon, S. J. & Bromley, B. C. 2004, *AJ*, 128, 1916
- Kenyon, S. J. & Luu, J. X. 1998, *AJ*, 115, 2136
- Kenyon, S. J. & Luu, J. X. 1999, *AJ*, 118, 1101
- Kuiper, G. P. 1951, *Proceedings of a topical symposium, commemorating the 50th anniversary of the Yerkes Observatory and half a century of progress in astrophysics*, New York: McGraw-Hill, 1951, edited by Hynek, J.A., p.357, 357
- Laplace, P.-S. 1796, in *Exposition du systeme du monde* (Paris: de l'Impr. Cercle-

- Social)
- Leonard, F. C. 1930, Leaflet of the Astronomical Society of the Pacific, 1, 121
- Levison, H. F. & Duncan, M. J. 1997, *Icarus*, 127, 13
- Lindblad, B. 1925, *ApJ*, 62, 191
- Luu, J. & Jewitt, D. 1996, *AJ*, 112, 2310
- Malhotra, R. 1993, *Nature*, 365, 819
- Malhotra, R. 1995, *AJ*, 110, 420
- Malhotra, R. 1998, Lunar and Planetary Institute Conference Abstracts, 29, 1476
- McFarland, J. 1996, *Vistas in Astronomy*, 40, 343
- Newton, I. 1686, *Philosophiae naturalis principia mathematica*, Joseph Streater. London, 1686
- Noll, K. S., Stephens, D. C., Grundy, W. M., Millis, R. L., Spencer, J., Buie, M. W., Tegler, S. C., Romanishin, W., & Cruikshank, D. P. 2002, *AJ*, 124, 3424
- Oort, J. H. 1927, *Bull. Astron. Inst. Netherlands*, 3, 275
- Oort, J. H. 1940, *ApJ*, 91, 273
- Oort, J. H. 1950, *Bull. Astron. Inst. Netherlands*, 11, 91
- Oort, J. H. & Schmidt, M. 1951, *Bull. Astron. Inst. Netherlands*, 11, 259
- Peixinho, N., Boehnhardt, H., Belskaya, I., Doressoundiram, A., Barucci, M. A., & Delsanti, A. 2004, *Icarus*, 170, 153
- Russell, H. N. 1906, *ApJ*, 24, 1
- Sheppard, S. S. & Jewitt, D. C. 2002, *AJ*, 124, 1757
- 2003, *Earth Moon and Planets*, 92, 207
- Sheppard, S. S. & Jewitt, D. 2004, *AJ*, 127, 3023
- Stern, S. A. & Yelle, R. V. 1999, *Pluto and Charon*, Academic Press
- Strazzulla, G., Leto, G., Baratta, G. A., & Spinella, F. 1991, *J. Geophys. Res.*, 96, 17547
- Tegler, S. C. & Romanishin, W. 2000, *Nature*, 407, 979
- Thomas, N., et al. 2000, *ApJ*, 534, 446
- Tiscareno, M. S. & Malhotra, R. 2003, *AJ*, 126, 3122
- Trujillo, C. A. & Brown, M. E. 2002, *ApJ*, 566, L125
- Trujillo, C. A., Jewitt, D. C., & Luu, J. X. 2001a, *AJ*, 122, 457
- Trujillo, C. A., Luu, J. X., Bosh, A. S., and Elliot, J. L. 2001b, *AJ* 122, 2740.
- Veillet, C., et al. 2002, *Nature*, 416, 711
- Weidenschilling, S. J. 1977, *Ap&SS*, 51, 153
- Weidenschilling, S. J. 2002, *Icarus*, 160, 212
- Whipple, F. L. 1950, *ApJ*, 111, 375
- van Woerkom, A. J. J. 1948, *Bull. Astron. Inst. Netherlands*, 10, 445
- Yanagisawa, M. 2002, *Icarus*, 159, 300

Detectability of KBO lightcurves

ABSTRACT

We present a statistical study of the detectability of lightcurves of Kuiper Belt objects (KBOs). Some Kuiper Belt objects display lightcurves that appear "flat", i.e., there are no significant brightness variations within the photometric uncertainties. Under the assumption that KBO lightcurves are mainly due to shape, the lack of brightness variations may be due to (1) the objects have very nearly spherical shapes, or (2) their rotation axes coincide with the line of sight. We investigate the relative importance of these two effects and relate it to the observed fraction of "flat" lightcurves. This study suggests that the fraction of KBOs with detectable brightness variations may provide clues about the shape distribution of these objects. Although the current database of rotational properties of KBOs is still insufficient to draw any statistically meaningful conclusions, we expect that, with a larger dataset, this method will provide a useful test for candidate KBO shape distributions.

Pedro Lacerda & Jane Luu
Icarus, **161**, 174–180, (2003)

2.1 Introduction

THE Kuiper Belt holds a large population of small objects which are thought to be remnants of the protosolar nebula (Jewitt & Luu 1993). The Belt is also the most likely origin of other outer solar system objects such as Pluto-Charon, Triton, and the short-period comets; its study should therefore provide clues to the understanding of the processes that shaped our solar system. More than 650 Kuiper Belt objects (KBOs) are known to date and a total of about 10^5 objects larger than 50 km are thought to orbit the Sun beyond Neptune (Jewitt & Luu 2000).

One of the most fundamental ways to study physical properties of KBOs is through their lightcurves. Lightcurves show periodic brightness variations due to rotation, since, as the KBO rotates in space, its cross-section as projected in the plane of the sky will vary due to its non-spherical shape, resulting in periodic brightness variations (see Fig. 2.1). A well-sampled lightcurve will thus yield the rotation period of the KBO, and the lightcurve amplitude has information on the KBO's shape. This technique is commonly used in planetary astronomy, and has been developed extensively for the purpose of determining the shapes, internal density structures, rotational states, and surface properties of atmosphereless bodies. These properties in turn provide clues to their formation and collisional environment.

Although lightcurves studies have been carried out routinely for asteroids and planetary satellites, the number of KBO lightcurves is still meager, with few of sufficient quality for analysis (see Table 2.1). This is due to the fact that most KBOs are faint objects, with apparent red magnitude of $m_R \sim 23$ (Trujillo *et al.* 2001), rendering it very difficult to detect small amplitude changes in their brightness. One of the few high quality lightcurves is that of (20000) Varuna, which shows an amplitude of $\Delta m = 0.42 \pm 0.02$ mag and a period of $P_{\text{rot}} = 6.3442 \pm 0.0002$ hrs (Jewitt & Sheppard 2002). Only recently have surveys started to yield significant numbers of KBOs bright enough for detailed studies (Jewitt *et al.* 1998).

Another difficulty associated with the measurement of the amplitude of a lightcurve is the one of determining the period of the variation. If no periodicity is apparent in the data, any small variations in the brightness of an object must be due to noise. Furthermore, a precise measurement of the amplitude of the lightcurve requires a complete coverage of the rotational phase. Therefore, any conclusion based on amplitudes of lightcurves must assume that their periods have been determined and confirmed by well sampled phase plots of the data.

However, not all of the observed KBOs show detectable brightness variations (the so-called "flat" lightcurves). The simplest explanations for this could be due to (1) the object is axisymmetric (the two axes perpendicular to the spin vector are equal), or (2) its rotation axis is nearly coincident with the line of

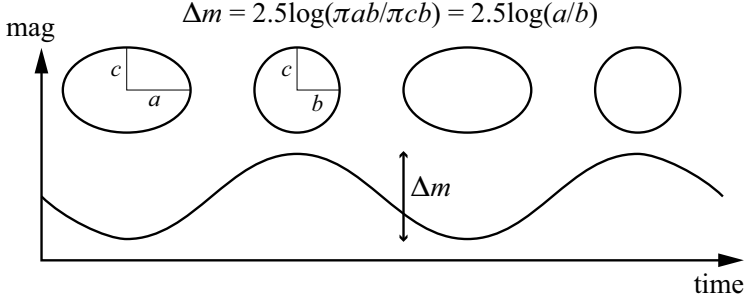


Figure 2.1 – The lightcurve of an ellipsoidal KBO observed at aspect angle $\theta = \pi/2$. Cross-sections and lightcurve are represented for one full rotation of the KBO. The amplitude, Δm , of the lightcurve is determined for this particular case. See text for the general expression.

Table 2.1 – KBOs with measured lightcurves.

Name	Class ^a	H^b [mag]	Δm^c [mag]	P^d [hrs]	Source ^e
1993 SC	C	6.9	<0.04		RT99
1994 TB	P	7.1	0.3	6.5	RT99
1996 TL ₆₆	S	5.4	<0.06		RT99
1996 TP ₆₆	P	6.8	<0.12		RT99
1994 VK ₈	C	7.0	0.42	9.0	RT99
1996 TO ₆₆	C	4.5	0.1	6.25	Ha00
(20000) Varuna	C	3.7	0.42	6.34	JS02
1995 QY ₉	P	7.5	0.6	7.0	RT99
1996 RQ ₂₀	C	7.0	—		RT99
1996 TS ₆₆	C	6.4	<0.16		RT99
1996 TQ ₆₆	C	7.0	<0.22		RT99
1997 CS ₂₉	C	5.2	<0.2		RT99
1999 TD ₁₀	S	8.8	0.68	5.8	Co00

^adynamical class (C=classical KBO, P=plutino, S=scattered KBO)

^babsolute magnitude

^clightcurve amplitude

^dspin period

^eRT99=Romanishin & Tegler (1999), Ha00=Hainaut (2000),
Co00=Consolmagno et al. (2000), JS02=Jewitt & Sheppard (2002)

sight (see Fig. 2.3). In other words, the undetectable variations are either a consequence of the KBO's shape, or of the observational geometry. By studying the relative probabilities of these two causes, and relating them to the observed fraction of "flat" lightcurves, we might expect to improve our knowledge of the intrinsic shape distribution of KBOs. In this paper we address the following question: Can we learn something about the shape distribution of KBOs from the fraction of "flat" lightcurves?

Symbol	Description
$a \geq b \geq c$	axes of ellipsoidal KBO
$\tilde{a} \geq \tilde{b} \geq \tilde{c}$	normalized axes of KBO ($\tilde{b} = 1$)
θ	aspect angle
Δm_{\min}	minimum detectable lightcurve amplitude
θ_{\min}	aspect angle at which $\Delta m = \Delta m_{\min}$
K	$10^{0.8\Delta m_{\min}}$

Table 2.2 – Used symbols and notation.

2.2 Definitions and Assumptions

The observed brightness variations in KBO lightcurves can be due to:

- eclipsing binary KBOs
- surface albedo variations
- irregular shape

In general the brightness variations will arise from some combination of these three factors, but the preponderance of each effect among KBOs is still not known. In the following calculations we exclude the first two factors and assume that shape is the sole origin of KBO brightness variations. We further assume that KBO shapes can be approximated by triaxial ellipsoids, and thus expect a typical KBO lightcurve to show a set of 2 maxima and 2 minima for each full rotation (see Fig. 2.1). Table 2.2 summarizes the used symbols and notations. The listed quantities are defined in the text.

The detailed assumptions of our model are as follows:

1. *The KBO shape is a triaxial ellipsoid.* This is the shape assumed by a rotating body in hydrostatic equilibrium (Chandrasekhar 1969). There are reasons to believe that KBOs might have a “rubble pile” structure (Farinella *et al.* 1981), justifying the approximation even further.
2. *The albedo is constant over surface.* Although albedo variegation can in principle explain any given lightcurve (Russell 1906), the large scale brightness variations are generally attributed to the object’s irregular shape (Burns & Tedesco 1979).
3. *All axis orientations are equally probable.* Given that we have no knowledge of preferred spin vector orientation, this is the most reasonable *a priori* assumption.
4. *The KBO is in a state of simple rotation around the shortest axis (the axis of maximum moment of inertia).* This is likely since the damping timescale of a complex rotation (e.g., precession), $\sim 10^3$ yr, (Burns & Safronov 1973), (Harris 1994) is smaller than the estimated time between collisions (10^7 – 10^{11} yr) that would re-excite such a rotational state (Stern 1995; Davis & Farinella 1997).

5. *The KBO is observed at zero phase angle ($\alpha = 0$).* It has been shown from asteroid data that lightcurve amplitudes seem to increase linearly with phase angle,

$$A(\theta, 0) = A(\theta, \alpha)/(1 + m\alpha),$$

where θ is the aspect angle, α is the phase angle and m is a coefficient which depends on surface composition. The aspect angle is defined as the angle between the line of sight and the spin axis of the KBO (see Fig. 2.2a), and the phase angle is the Sun-object-Earth angle. The mean values of m found for different asteroid classes are $m(\text{S}) = 0.030$, $m(\text{C}) = 0.015$, $m(\text{M}) = 0.013$, where S, C, and M are asteroid classes (see (Michalowsky 1993)). Since KBO are distant objects the phase angle will always be small. Even allowing m to be one order of magnitude higher than that of asteroids the increase in the lightcurve amplitude will not exceed 1%.

6. *The brightness of the KBO is proportional to its cross-section area (geometric scattering law).* This is a good approximation for KBOs because (1) most KBOs are too small to hold an atmosphere, and (2) the fact that they are observed at very small phase angles reduces the influence of scattering on the lightcurve amplitude (Magnusson 1989).

The KBOs will be represented by triaxial ellipsoids of axes $a \geq b \geq c$ rotating around the short axis c (see Fig. 2.2b). In order to avoid any scaling factors we normalize all axes by b , thus obtaining a new set of parameters \tilde{a} , \tilde{b} and \tilde{c} given by

$$\tilde{a} = a/b, \quad \tilde{b} = 1, \quad \tilde{c} = c/b. \tag{2.1}$$

As defined, \tilde{a} and \tilde{c} can assume values $1 \leq \tilde{a} < \infty$ and $0 < \tilde{c} \leq 1$. Note that the parameters \tilde{a} and \tilde{c} are dimensionless.

The orientation of the spin axis of the KBO relative to the line of sight will be defined in spherical coordinates (θ, ϕ) , with the line of sight (oriented from the object to the observer) being the z -axis, or polar axis, and the angle θ being the polar angle (see Fig. 2.2a). The solution is independent of the azimuthal angle ϕ , which would be measured in the plane perpendicular to the line of sight, between an arbitrary direction and the projection of the spin axis on the same plane. The observation geometry is parameterized by the aspect angle, which in this coordinate system corresponds to θ .

As the object rotates, its cross-section area S will vary periodically between S_{\max} and S_{\min} (see Fig. 2.1). These areas are simply a function of a , b , c and the aspect angle θ . Given the assumption of geometric scattering, the ratio between maximum and minimum flux of reflected sunlight will be equal to the ratio between S_{\max} and S_{\min} . The lightcurve amplitude can then be calculated

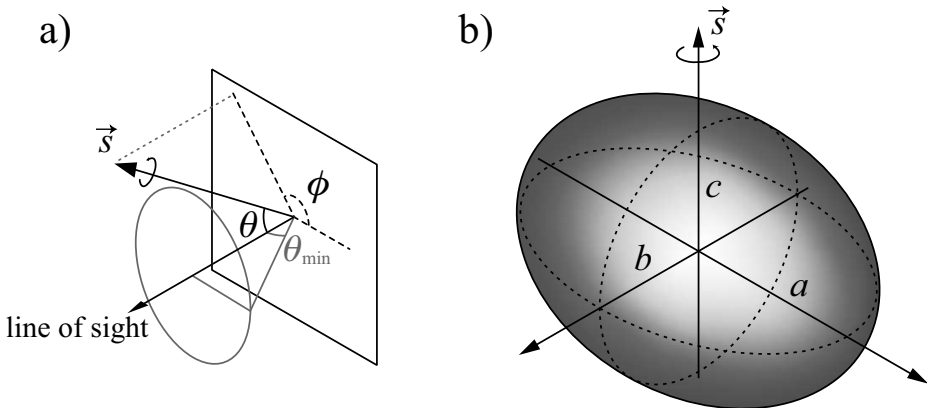


Figure 2.2 – a) A spherical coordinate system is used to represent the observing geometry. The line of sight (oriented from the object to the observer) is the polar axis and the azimuthal axis is arbitrary in the plane orthogonal to the polar axis. θ and ϕ are the spherical angular coordinates of the spin axis \vec{s} . In this coordinate system the aspect angle is given by θ . The “non-detectability” cone, with semi-vertical angle θ_{\min} , is represented in grey. If the spin axis lies within this cone the brightness variations due to changing cross-section will be smaller than photometric errors, rendering it impossible to detect brightness variations. **b)** The picture represents an ellipsoidal KBO with axes $a \geq b \geq c$.

from the quantities \tilde{a} , \tilde{c} and θ and is given by

$$\Delta m = 2.5 \log \sqrt{\frac{\tilde{a}^2 \cos^2 \theta + \tilde{a}^2 \tilde{c}^2 \sin^2 \theta}{\tilde{a}^2 \cos^2 \theta + \tilde{c}^2 \sin^2 \theta}}. \quad (2.2)$$

2.3 “Flat” Lightcurves

It is clear from Eqn. (2.2) that under certain conditions, Δm will be zero, i.e., the KBO will exhibit a flat lightcurve. These special conditions involve the shape of the object and the observation geometry, and are described quantitatively below. Taking into account photometric error bars will bring this “flatness” threshold to a finite value, Δm_{\min} , a minimum detectable amplitude below which brightness variation cannot be ascertained.

The two factors that influence the amplitude of a KBO lightcurve are:

1. Sphericity For a given ellipsoidal KBO of axes ratios \tilde{a} and \tilde{c} the lightcurve amplitude will be largest when $\theta = \pi/2$ and smallest when $\theta = 0$ or π . At $\theta = \pi/2$, Eqn. (2.2) becomes

$$\Delta m = 2.5 \log \tilde{a}. \quad (2.3)$$

Even at $\theta = \pi/2$, having a minimum detectable amplitude, Δm_{\min} , puts constraints on \tilde{a} since if \tilde{a} is too small, the lightcurve amplitude will not be detected.

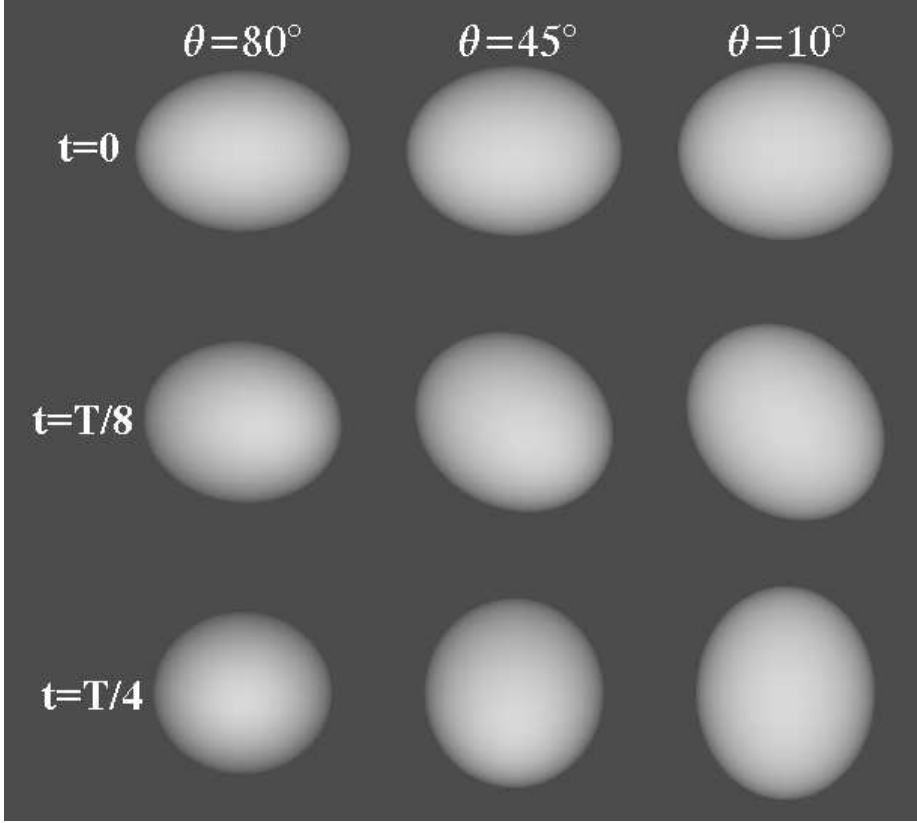


Figure 2.3 – Illustration of a rotating ellipsoid at different aspect angles. A quarter of a full rotation is represented. Rotational phase of ellipsoid increasing from top to bottom and θ decreasing from left to right. T is the period of rotation. Axes ratios are $\tilde{a} = 1.2$ and $\tilde{c} = 0.9$.

This constraint is thus

$$\tilde{a} < 10^{0.4\Delta m_{\min}} \Rightarrow \text{“flat” lightcurve} . \quad (2.4)$$

2. Observation geometry If the rotation axis is nearly aligned with the line of sight, i.e., if the aspect angle is sufficiently small, the object’s projected cross-section will hardly change with rotation, yielding no detectable brightness variations (see Fig. 2.3). The finite accuracy of the photometry defines a minimum aspect angle, θ_{\min} , within which the lightcurve will appear flat within the uncertainties. This angle rotated around the line of sight generates the “non-detectability cone” (see Fig. 2.2a), with the solid angle

$$\Omega(\theta_{\min}) = \int_0^{2\pi} \int_0^{\theta_{\min}} \sin \theta \, d\theta \, d\phi . \quad (2.5)$$

Any aspect angle θ which satisfies $\theta < \theta_{\min}$ falls within the “non-detectability cone” and results in a non-detectable lightcurve amplitude. Therefore, the probability that the lightcurve will be flat due to observing geometry is

$$p_{\tilde{a},\tilde{c}}(\text{non-detection}) = \frac{2 \times \Omega(\theta_{\min})}{4\pi} = 1 - \cos \theta_{\min} \quad (2.6)$$

$$p_{\tilde{a},\tilde{c}}(\text{detection}) = \cos \theta_{\min} . \quad (2.7)$$

The factor of 2 accounts for the fact that the axis might be pointing towards or away from the observer and still give rise to the same observations, and the 4π in the denominator represents all possible axis orientations.

From Eqn. (2.2) we can write $\cos \theta_{\min}$ as a function of \tilde{a} and \tilde{c} ,

$$\cos \theta_{\min} = \Psi(\tilde{a}, \tilde{c}) = \sqrt{\frac{\tilde{c}^2(\tilde{a}^2 - K)}{\tilde{c}^2(\tilde{a}^2 - K) + \tilde{a}^2(K - 1)}} , \quad (2.8)$$

where $K = 10^{0.8\Delta m_{\min}}$. The function $\Psi(\tilde{a}, \tilde{c})$, represented in Fig. 2.4, is the probability of detecting brightness variation from a given ellipsoid of axes ratios (\tilde{a}, \tilde{c}) . It is a geometry weighting function. For \tilde{a} in $[1, \sqrt{K}]$ we have $\Psi(\tilde{a}, \tilde{c}) = 0$ by definition, since in this case the KBO satisfies Eqn. (2.4) and its lightcurve amplitude will not be detected irrespective of the aspect angle. It is clear from Fig. 2.4 that it is more likely to detect brightness variation from an elongated body.

2.4 Detectability of Lightcurves

In order to generate a “non-flat” lightcurve, the KBO has to satisfy both the shape and observation geometry conditions. Mathematically this means that the probability of detecting brightness variation from a KBO is a function of the probabilities of the KBO satisfying both the sphericity and observing geometry conditions.

We will assume that it is possible to represent the shape distribution of KBOs by two independent probability density functions, $f(\tilde{a})$ and $g(\tilde{c})$, defined as

$$p(\tilde{a}_1 \leq \tilde{a} \leq \tilde{a}_2) = \int_{\tilde{a}_1}^{\tilde{a}_2} f(\tilde{a}) d\tilde{a}, \int_1^{\infty} f(\tilde{a}) d\tilde{a} = 1 , \quad (2.9)$$

$$p(\tilde{c}_1 \leq \tilde{c} \leq \tilde{c}_2) = \int_{\tilde{c}_1}^{\tilde{c}_2} g(\tilde{c}) d\tilde{c}, \int_0^1 g(\tilde{c}) d\tilde{c} = 1 , \quad (2.10)$$

where the integrals on the left represent the fraction of KBOs in the given ranges of axes ratios. This allows us to write the following expression for $p(\Delta m >$

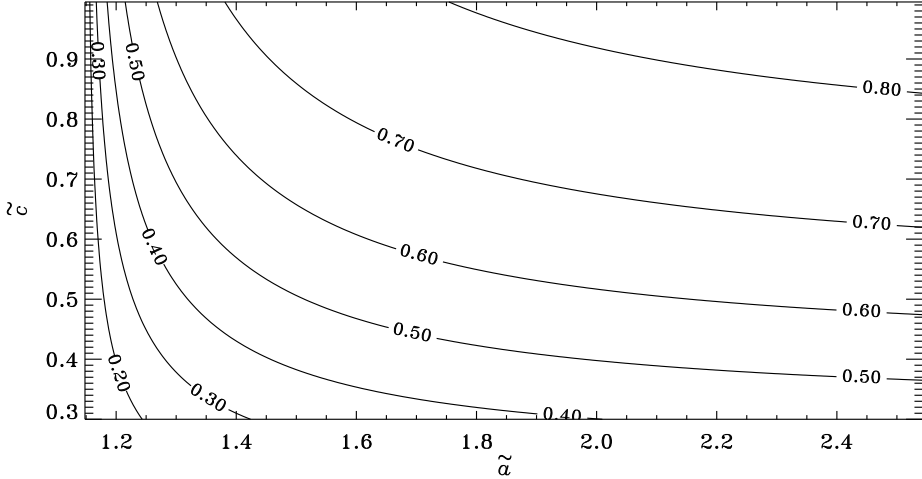


Figure 2.4 – The function $\Psi(\tilde{a}, \tilde{c})$ (Eqn. 2.8). This plot assumes photometric errors $\Delta m_{\min} = 0.15$ mag. The detection probability is zero when $\tilde{a} < 10^{0.4\Delta m_{\min}} \approx 1.15$.

Δm_{\min}), where both the shape and observation geometry constraints are taken into account,

$$p(\Delta m > \Delta m_{\min}) = \int_0^1 \int_1^\infty \Psi(\tilde{a}, \tilde{c}) f(\tilde{a}) g(\tilde{c}) d\tilde{a} d\tilde{c}. \quad (2.11)$$

The right hand side of this equation represents the probability of observing a given KBO with axes ratios between (\tilde{a}, \tilde{c}) and $(\tilde{a} + d\tilde{a}, \tilde{c} + d\tilde{c})$, at a large enough aspect angle, integrated for all possible axes ratios. This is also the probability of detecting brightness variation for an observed KBO.

The lower limit of integration for \tilde{a} in Eqn. (2.11) can be replaced by \sqrt{K} , with K defined as in Eqn. (2.8), since $\Psi(\tilde{a}, \tilde{c})$ is zero for \tilde{a} in $[1, \sqrt{K}]$. In fact, this is how the sphericity constraint is taken into account.

Provided that we know the value of $p(\Delta m > \Delta m_{\min})$ Eqn. (2.11) can test candidate distributions $f(\tilde{a})$ and $g(\tilde{c})$ for the shape distribution of KBOs. The best estimate for $p(\Delta m > \Delta m_{\min})$ is given by the ratio of “non-flat” lightcurves (N_D) to the total number of measured lightcurves (N), i.e.,

$$p(\Delta m > \Delta m_{\min}) \approx \frac{N_D}{N}. \quad (2.12)$$

Because N is not the total number of KBOs there will be an error associated with this estimate. Since we do not know the distributions $f(\tilde{a})$ and $g(\tilde{c})$ we will assume that the outcome of an observation can be described by a binomial distribution of probability $p(\Delta m > \Delta m_{\min})$. This is a good approximation given that N is very small compared with the total number of KBOs. Strictly speaking,

the hypergeometric distribution should be used since we will not unintentionally observe the same object more than once (sampling without replacement). However, since the total number of KBOs (which is not known with certainty) is much larger than any sample of lightcurves, any effects of repeated sampling will be negligible, thereby justifying the binomial approximation. This simplification allows us to calculate the upper (p_+) and lower (p_-) limits for $p(\Delta m > \Delta m_{\min})$ at any given confidence level, C . These values, known as the Clopper–Pearson confidence limits, can be found solving the following equations by trial and error (Barlow 1989),

$$\sum_{r=N_D+1}^N P(r; p_+(\Delta m > \Delta m_{\min}), N) = \frac{C+1}{2} \quad (2.13)$$

$$\sum_{r=0}^{N_D-1} P(r; p_-(\Delta m > \Delta m_{\min}), N) = \frac{C+1}{2}, \quad (2.14)$$

(see Table 2.2 for notation) where C is the desired confidence level and $P(r; p, N)$ is the binomial probability of detecting r lightcurves out of N observations, each lightcurve having a detection probability p . Using the values in Table 2.1 and $\Delta m_{\min} = 0.15$ mag we have $N_D = 5$ and $N = 13$ which yields

$$p(\Delta m > \Delta m_{\min}) = 0.38_{-0.15}^{+0.18}$$

at a $C = 0.68$ (1σ) confidence level. At $C = 0.997$ (3σ) we have

$$p(\Delta m > \Delta m_{\min}) = 0.38_{-0.31}^{+0.41}.$$

The value of $p(\Delta m > \Delta m_{\min})$ could be smaller since some of the flat lightcurves might not have been published.

Note that for moderately elongated ellipsoids (small \tilde{a}) the function $\Psi(\tilde{a}, \tilde{c})$ is almost insensitive to the parameter \tilde{c} (see Fig. 2.4), in which case the axisymmetric approximation with respect to \tilde{a} can be made yielding $\tilde{c} \approx 1$. Equation (2.11) then has only one unknown parameter, $f(\tilde{a})$.

$$p(\Delta m > \Delta m_{\min}) \approx \int_{\sqrt{K}}^{\tilde{a}_{\max}} \Psi(\tilde{a}, 1) f(\tilde{a}) d\tilde{a} \approx 0.38_{-0.31}^{+0.41}. \quad (2.15)$$

If we assume the function $f(\tilde{a})$ to be gaussian, we can use Eqn. (4.3) to determine its mean μ and standard deviation σ , after proper normalization to satisfy Eqn. (2.9). The result is represented in Fig. 2.5, where we show all possible pairs of (μ, σ) that would satisfy a given $p(\Delta m > \Delta m_{\min})$. For example, the line labeled "0.38" identifies all possible pairs of (μ, σ) that give rise to $p(\Delta m > \Delta m_{\min}) = 0.38$, the line labeled "0.56" all possible pairs of (μ, σ) that give rise to $p(\Delta m > \Delta m_{\min}) = 0.56$, etc.

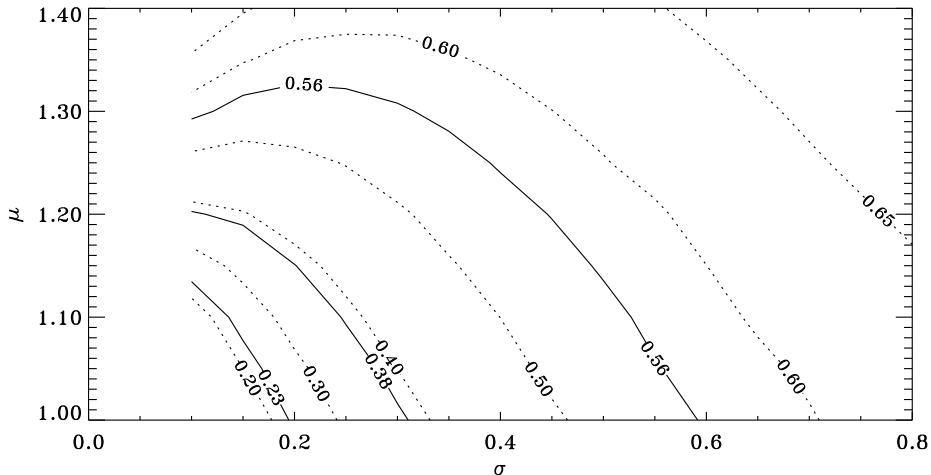


Figure 2.5 – Contour plot of the theoretical probabilities of detecting brightness variation in KBOs (assuming $\Delta m_{\min} = 0.15$ mag), drawn from gaussian shape distributions parameterized by μ and σ (respectively the mean and spread of the distributions). The solid lines represent the observed ratio of “non-flat” lightcurves (at 0.38) and 0.68 confidence limits (at 0.23 and 0.56 respectively).

Clearly, with the present number of lightcurves the uncertainties are too large to draw any relevant conclusions on the shape distribution of KBOs. With a larger dataset, this formulation will allow us to compare the distribution of KBO shapes with that of the main belt asteroids. The latter has been shown to resemble, to some extent, that of fragments of high-velocity impacts (Catullo *et al.* 1984). It deviates at large asteroid sizes that have presumably relaxed to equilibrium figures. A comparison of $f(\tilde{a})$ with asteroidal shapes should tell us, at the very least, whether KBO shapes are collisionally derived, as opposed to being accretional products.

The usefulness of this method is that, with more data, it would allow us to derive such quantitative parameters as the mean and standard deviation of the KBO shape distribution, if we assume *a priori* some intrinsic form for this distribution. The method’s strength is that it relies solely on the detectability of lightcurve amplitudes, which is more robust than other lightcurve parameters.

This paper focuses on the influence of the observation geometry and KBO shapes in the results of lightcurve measurements. In which direction would our conclusions change with the inclusion of albedo variegation and/or binary KBOs?

Non-uniform albedo would cause nearly spherical KBOs to generate detectable brightness variations, depending on the coordinates of the albedo patches on the KBO’s surface. This means that our method would overestimate the num-

ber of elongated objects by attributing all brightness fluctuations to asphericity.

Binary KBOs would influence the results in different ways depending on the orientation of the binary system’s orbital plane, on the size ratio of the components, and on the individual shapes and spin axis orientations of the primary and secondary. For example, an elongated KBO observed equator-on would have its lightcurve flattened by a nearly spherical moon orbiting in the plane of the sky, whereas two spherical KBOs orbiting each other would generate a lightcurve if the binary would be observed edge-on.

These effects are not straightforward to quantify analytically and might require a different approach. We intend to incorporate them in a future study. Also, with a larger sample of lightcurves it would be useful to apply this model to subgroups of KBOs based on dynamics, size, etc.

2.5 Conclusions

We derived an expression for the probability of detecting brightness variations from an ellipsoidal KBO, as a function of its shape and minimum detectable amplitude. This expression takes into account the probability that a “flat” lightcurve is caused by observing geometry.

Our model can yield such quantitative parameters as the mean and standard deviation of the KBO shape distribution, if we assume *a priori* an intrinsic form for this distribution. It concerns solely the statistical probability of detecting brightness variation from objects drawn from these distributions, given a minimum detectable lightcurve amplitude. The method relies on the assumption that albedo variegation and eclipsing binaries play a secondary role in the detection of KBO lightcurves. The effect of disregarding albedo variegation in our model is that we might overestimate the fraction of elongated objects. Binaries in turn could influence the result in both directions depending on the geometry of the problem, and on the physical properties of the constituents. We intend to incorporate these effects in a future, more detailed study.

Acknowledgments

We are grateful to Garrelt Mellema, Glenn van de Ven, and Prof. John Rice for helpful discussion.

References

- Barlow, R. 1989. *Statistics. A guide to the use of statistical methods in the physical sciences.* The Manchester Physics Series, New York: Wiley, 1989.
- Burns, J. A. and V. S. Safronov 1973. Asteroid nutation angles. *MNRAS* 165, 403-411.
- Burns, J. A. and E. F. Tedesco 1979. Asteroid lightcurves - Results for rotations and shapes. *Asteroids* 494-527.
- Catullo, V., V. Zappalà, P. Farinella, and P. Paolicchi 1984. Analysis of the shape distribution of asteroids. *A&A* 138, 464-468.
- Chandrasekhar, S. 1987. *Ellipsoidal figures of equilibrium.* New York : Dover, 1987. .
- Consolmagno, G. J., S. C. Tegler, T. Rettig, and W. Romanishin 2000. Size, Shape, Rotation, and Color of the Outer Solar System Object 1999 TD10. *AAS/Division for Planetary Sciences Meeting* 32, 21.07.
- Davis, D. R. and P. Farinella 1997. Collisional Evolution of Edgeworth-Kuiper Belt Objects. *Icarus* 125, 50-60.
- Farinella, P., P. Paolicchi, E. F. Tedesco, and V. Zappalà 1981. Triaxial equilibrium ellipsoids among the asteroids. *Icarus* 46, 114-123.
- Hainaut, O. R., C. E. Delahodde, H. Boehnhardt, E. Dotto, M. A. Barucci K. J. Meech, J. M. Bauer, R. M. West, and A. Doressoundiram 2000. Physical properties of TNO 1996 TO₆₆. Lightcurves and possible cometary activity. *A&A* 356, 1076-1088.
- Harris, A. W. 1994. Tumbling asteroids. *Icarus* 107, 209.
- Jewitt, D. and J. Luu 1993. Discovery of the candidate Kuiper belt object 1992 QB1. *Nature* 362, 730-732.
- Jewitt, D., J. Luu, and C. Trujillo 1998. Large Kuiper Belt Objects: The Mauna Kea 8K CCD Survey. *AJ* 115, 2125-2135.
- Jewitt, D. C. and J. X. Luu 2000. Physical Nature of the Kuiper Belt. *Protostars and Planets IV* 1201.
- Jewitt, D. C. and S. S. Sheppard 2002. Physical Properties of Trans-Neptunian Object (20000) Varuna. *AJ* 123, 2110-2120.
- Magnusson, P. 1989. Pole determinations of asteroids. *Asteroids II* 1180-1190.
- Michalowski, T. 1993. Poles, shapes, senses of rotation, and sidereal periods of asteroids. *Icarus* 106, 563.
- Romanishin, W. and S. C. Tegler 1999. Rotation rates of Kuiper-belt objects from their light curves. *Nature* 398, 129-132.
- Russell, H. N. 1906. On the light variations of asteroids and satellites. *ApJ* 24, 1-18.
- Stern, S. A. 1995. Collisional Time Scales in the Kuiper Disk and Their Implications. *AJ* 110, 856.
- Trujillo, C. A., J. X. Luu, A. S. Bosh, and J. L. Elliot 2001. Large Bodies in the Kuiper Belt. *AJ* 122, 2740-2748.

CHAPTER 3

The shape distribution

ABSTRACT

If we assume that the periodic brightness variations in a Kuiper Belt lightcurve are determined only by their aspherical shapes and the observing geometry (no spin rate bias is considered), the fraction of detectable Kuiper Belt lightcurves and the lightcurve amplitude distribution can be used to constrain the shapes of Kuiper Belt objects. The results indicate that most Kuiper Belt objects ($\sim 85\%$) have shapes that are close to spherical ($a/b \leq 1.5$), but there is a small but significant fraction ($\sim 12\%$) possessing highly aspherical shapes ($a/b \geq 1.7$). The distribution cannot be well fitted by a gaussian and is much better approximated by a power law.

Jane Luu & Pedro Lacerda
Earth Moon and Planets, **92**, 2007, (2003)

3.1 Introduction

SINCE their discovery in 1992, the Kuiper Belt objects (KBOs) have attracted a great deal of interest in planetary astronomy because of the information they might contain. Thought to be a relic from the original protoplanetary disk, they are expected to still bear signatures of their origin and evolution. In particular, they are believed to be much less evolved than other known solar system objects, and thus might show planetary formation at an early stage.

Although it has been a decade since their discovery, not much is known about the KBOs physical properties, mainly because most are too faint (red magnitude $m_R \geq 20$) for detailed studies. Most of the existing data are broadband photometry, with a few low-resolution optical and near-IR spectra. Broadband photometry indicates that the KBOs possess diverse colors, ranging from neutral to very red (Luu & Jewitt 1996; Tegler & Romanishin 2000; Jewitt & Luu 2001). The low-resolution KBO spectra are usually featureless, although a few show weak $2\mu\text{m}$ water ice absorption (Brown, Cruikshank & Pendleton 1999; Jewitt & Luu 2001). Some broadband photometric data have been obtained for the purpose of studying KBO rotational properties, and although reliable lightcurves are still sparse, the sample is sufficient for detailed analysis. In this paper we collect data from reliable lightcurves and examine their implications for the shape distribution of KBOs.

3.2 Observations

The largest and most systematic studies of KBO rotational properties were carried out by Sheppard & Jewitt (2002, hereafter SJ02) and Sheppard & Jewitt (2003, hereafter SJ03), which together present optical lightcurves of 27 KBOs. Their sample included most of the largest and brightest KBOs, with red absolute magnitude H_R in the range 6.0 – 7.5, corresponding to the diameter range 200 – 400 km. These large objects are unlikely to be collisional fragments. Interestingly, only 7 of the 27 yielded periodic lightcurves, which they defined as periodic brightness variations of amplitude $\Delta m \geq 0.15$. Other lightcurves exist besides those presented by SJ02 and SJ03, but they vary widely in quality and sometimes contradict each other. For example, Romanishin & Tegler (1999) report a flat lightcurve for 1996 TO66, while Hainaut et al. (2000) and SJ03 detected periodic lightcurve for the same object. Of the lightcurves in the literature that were not measured by them, SJ02 deemed 6 to be reliable and included them in their analysis. Of these 6, 2 showed periodic lightcurves. In this work we adopt the same practice and make use of the 27 lightcurves from Sheppard & Jewitt, plus the 6 reliable lightcurves from the literature. The KBO lightcurve statistics are thus as follows: out of 33 reliable lightcurves, 9 showed periodic lightcurves with amplitudes $\Delta m \geq 0.15$. The fraction of KBOs with detectable periodic

Table 3.1 – KBO rotational properties

KBO	P [hr]	Δm	Reference
KBOs lightcurves considered to have $\Delta m < 0.15$ mag			
1993 SC	–	0.04	RT99, DMcG97
1994 TB	–	-	SJ02
1996 GQ21	–	< 0.10	SJ02
1996 TL66	–	0.06	RT99, LJ98
1996 TP66	–	0.12	RT99, CB99
1997 CS29	–	< 0.08	SJ02
1998 HK151	–	< 0.15	SJ02
1998 VG44	–	< 0.10	SJ02
(Chaos) 1998 WH24	–	< 0.10	SJ02
1999 DE9	–	< 0.10	SJ02
(47171) 1999 TC36	–	< 0.10	SJ03
(Huya) 2000 EB173	–	< 0.06	SJ02
2000 YW134	–	< 0.10	SJ03
2001 CZ31	–	< 0.20	SJ02
2001 FP185	–	< 0.10	SJ03
2001 FZ173	–	< 0.06	SJ02
2001 KD77	–	< 0.10	SJ03
(28978) Ixion 2001 KX76	–	< 0.10	SJ03,O01
2001 QF298	–	< 0.10	SJ03
(42301) 2001 UR163	–	< 0.10	SJ03
(42355) 2002 CR46	–	< 0.10	SJ03
(55636) 2002 TX300	16.24 ± 0.08	0.08 ± 0.02	SJ03
(55637) 2002 UX25	–	< 0.10	SJ03
(55638) 2002 VE95	–	< 0.10	SJ03
KBO lightcurves considered to have $\Delta m \geq 0.15$ mag			
1995 QY9	–	0.60	SJ02, RT99
(24835) 1995 SM55	8.08 ± 0.03	0.19 ± 0.05	SJ03
1996 TO66	–	0.26 ± 0.03	SJ03, H00
1998 SM165	–	0.45	SJ02, R01
1998 BU48	9.8 ± 0.1	0.68 ± 0.04	SJ02
	12.6 ± 0.1		
1999 KR16	11.858 ± 0.002	0.18 ± 0.04	SJ02
	11.680 ± 0.002		
2000 GN171	8.329 ± 0.005	0.61 ± 0.03	SJ02
(Varuna) 2000 WR106	6.34	0.42 ± 0.03	SJ02
2003 AZ84	13.42 ± 0.05	0.14 ± 0.03	SJ03

CB99 = Collander-Brown *et al.* 1999, DMcG97 = Davies, McBride & Green 1997,
 H00 = Hainaut *et al.* 2000, LJ98 = Luu & Jewitt 1998, O01 = Ortiz *et al.* 2001, R01
 = Romanishin *et al.* 2001, RT99 = Romanishin & Tegler 1999, SJ02 = Sheppard &
 Jewitt 2002, SJ03 = Sheppard & Jewitt 2003.

lightcurves is then:

$$f(\Delta m \geq 0.15) = 9/33 = 27\%. \quad (3.1)$$

All 33 KBOs and their lightcurve parameters are listed in Table 1; the 9 KBOs considered in this work as having periodic lightcurves are clustered at the bottom of the Table. Assuming that the lightcurves are modulated by aspherical shapes and are therefore double-peaked, the periods range from 6 to 12 hrs.

3.3 Discussion

Lacerda & Luu (2003) show that the fraction of detectable KBO lightcurves can be used to infer these objects shape distribution, if certain (reasonable) assumptions are made. The assumptions are

1. *Asphericity.* The lightcurve modulations are assumed to arise from an aspherical shape, taken to be a triaxial ellipsoid with axes $a \geq b \geq c$. The minimum detectable lightcurve amplitude Δm_{\min} must be as large as the photometric error, or it will not be detected.
2. *Observation geometry.* The angle between the KBO spin axis and the line of sight – the aspect angle θ – should also be large enough to give rise to a detectable lightcurve amplitude, i.e., larger than Δm_{\min} .

Here we adopt SJ02’s photometric error of 0.15 mag, i.e., $\Delta m_{\min} = 0.15$. If a lightcurve does not show periodic modulations, it is assumed that this is because neither the asphericity nor the observation geometry criterion is satisfied. No spin rate bias is considered here.

With these assumptions, the probability p of detecting a lightcurve can be written as (Lacerda & Luu 2003)

$$p(\Delta m > \Delta m_{\min}) = \int_0^1 \int_1^\infty \Psi(\tilde{a}, \tilde{c}) f(\tilde{a}) g(\tilde{c}) d\tilde{a} d\tilde{c}. \quad (3.2)$$

where, for the sake of being concise, we define $\tilde{a} = a/b$, $\tilde{c} = c/b$, and $\Psi(\tilde{a}, \tilde{c})$ is the probability of detecting brightness variations from a given ellipsoid of axis ratio (\tilde{a}, \tilde{c}) . $\Psi(\tilde{a}, \tilde{c})$ is given by

$$\Psi(\tilde{a}, \tilde{c}) = \sqrt{\frac{\tilde{c}^2(\tilde{a}^2 - K)}{\tilde{c}^2(\tilde{a}^2 - K) + \tilde{a}^2(K - 1)}}, \quad (3.3)$$

where $K = 10^{0.8\Delta m_{\min}}$. The right hand side of Eqn. (3.2) represents the probability of observing a given KBO with axis ratios between (\tilde{a}, \tilde{c}) and $(\tilde{a}+d\tilde{a}, \tilde{c}+d\tilde{c})$ at a large enough aspect angle, integrated over all possible axis ratios. For moderately elongated ellipsoids (small \tilde{a}), the function $\Psi(\tilde{a}, \tilde{c})$ is almost independent of \tilde{c} . If we further assume $\tilde{c} \approx 1$, then $g(\tilde{c})$ is ≈ 1 , and Eqn. (3.2) becomes

$$p(\Delta m > \Delta m_{\min}) \approx \int_1^\infty \Psi(\tilde{a}, 1) f(\tilde{a}) d\tilde{a}. \quad (3.4)$$

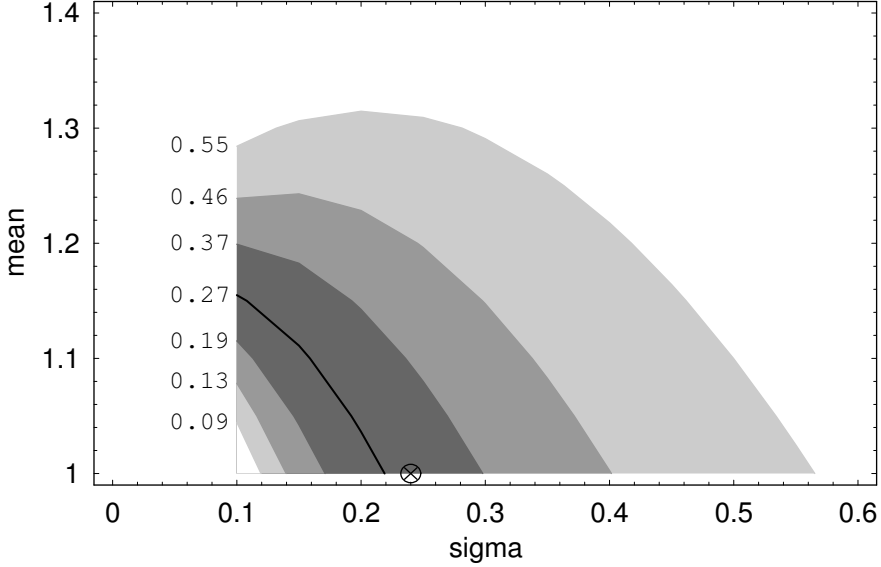


Figure 3.1 – The probability p as a function of the mean μ and standard deviation σ of a gaussian \tilde{a} distribution. The thick black line represents all $\mu - \sigma$ pairs that give rise to $p = 0.27$. The shaded areas immediately adjacent to the line represent the μ and σ values within the 1σ limits, the next shaded areas outward represent the 2σ limits, and the outermost shaded area the 3σ limits. The number to the left of each boundary line indicates the p value corresponding to that line. The circle with the cross marks the best-fit $\mu - \sigma$: $\mu = 1.00, \sigma = 0.24$.

From Eqn. (3.1), $p(\Delta m > \Delta m_{\min}) = 0.27$. Since the data did not sample the entire KBO population, there are necessarily errors associated with p . The 1-, 2- and 3σ error bars on p can be calculated based on the Clopper-Pearson confidence limits (Lacerda & Luu 2003):

$$\begin{aligned}
 1\sigma \quad p &= 0.27^{+0.10}_{-0.08} \\
 2\sigma \quad p &= 0.27^{+0.19}_{-0.14} \\
 3\sigma \quad p &= 0.27^{+0.28}_{-0.18}
 \end{aligned} \tag{3.5}$$

With p known, the problem then becomes inverting Eqn. (3.4) to determine the shape distribution $f(\tilde{a})$. This can be done if $f(\tilde{a})$ is assumed to be a simple analytical function.

3.3.1 Gaussian distribution

First we assume $f(\tilde{a})$ to be a gaussian with a mean denoted by μ and a standard deviation σ . All possible combinations of $\mu - \sigma$ that satisfy Eqn. (3.5) are plotted in Fig. 3.1. The thick black curve represents all possible combinations of $\mu - \sigma$ that give rise to $p = 0.27$, and the shaded regions represent the areas enclosed

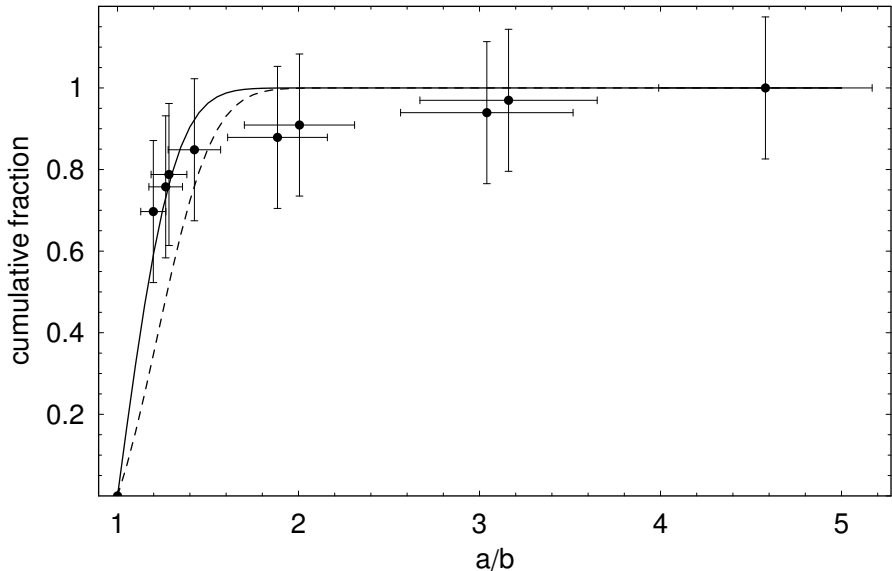


Figure 3.2 – Cumulative fractions of KBOs as a function of $a/b = \tilde{a}$. The solid line corresponds to the best-fit gaussian ($\mu = 1.00, \sigma = 0.24$), the dashed line a gaussian with $\mu = 1.22, \sigma = 0.24$. The data are from Table 1, with vertical error bars calculated from Poisson statistics. The horizontal error bars are calculated from 1σ deviation from the average aspect angle of 60° , assuming that the aspect angle is uniformly distributed in $\sin\theta$. Note: our x-axis is a/b , which is the inverse of SJ02’s x-axis, b/a .

by p ’s 1-, 2-, and 3σ error bars. The entire shaded regions thus represent all possible combinations of $\mu - \sigma$ that are consistent with $p = 0.27_{-0.18}^{+0.28}$.

We can constrain $\mu - \sigma$ further by making use of the observed axis ratios \tilde{a} . Using the data from Table 1, for each detected lightcurve, the observed Δm is converted to the axis ratio \tilde{a} by using the relation (Lacerda & Luu 2003)

$$\Delta m = 2.5 \log \sqrt{\frac{\tilde{a}^2 \cos^2 \theta + \tilde{a}^2 \tilde{c}^2 \sin^2 \theta}{\tilde{a}^2 \cos^2 \theta + \tilde{c}^2 \sin^2 \theta}}, \quad (3.6)$$

and by assuming an average aspect angle $\theta = 60^\circ$. ($\theta = 60^\circ$ is the average angle if θ is distributed uniformly in $\sin\theta$). The observed cumulative fractions of KBOs, as a function of \tilde{a} , are plotted in Fig. 3.2. These can then be compared with the cumulative fractions predicted by each allowed $\mu - \sigma$ pair to yield the best-fit gaussian. A grid search is performed through all possible $\mu - \sigma$ pairs allowed by Eqn. (3.5); using χ^2 as the comparison criterion, the best-fit gaussian is given by

$$\mu = 1.00(+0.22), \sigma = 0.24_{-0.13}^{+0.18}. \quad (3.7)$$

The error bars in Eqn. (3.7) are 1σ error bars. There is no lower error bar to

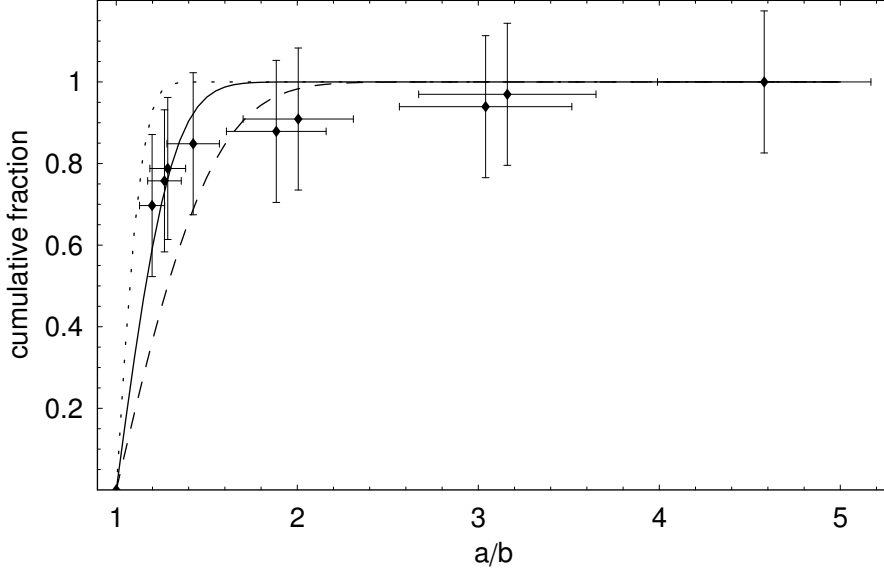


Figure 3.3 – Cumulative fractions of KBOs as a function of $a/b = \tilde{a}$. Same as Fig. 3.2, but this time with the dotted line representing a gaussian with $\mu = 1.00, \sigma = 0.11$, the dashed line a gaussian with $\mu = 1.00, \sigma = 0.42$.

μ since μ represents the mean \tilde{a} , defined to be ≥ 1 . The best-fit $\mu - \sigma$ is also marked in Fig. 3.1.

The goodness of the fit is shown graphically in Fig. 3.2 where we plot the observed cumulative fractions of KBOs, as a function of $\tilde{a} = a/b$, with the cumulative fractions predicted by the best-fit gaussian (Eqn. 3.7). The fit is good for $\tilde{a} \leq 1.5$ but poor at larger \tilde{a} 's. The Figure also shows that if we increase μ to $\mu = 1.22$ (1 standard deviation away from the best-fit μ), the theoretical curve comes closer to fitting the larger \tilde{a} 's, but misses practically all the data points. [Note: our x-axis is $\tilde{a} = a/b$, which is the inverse of SJ02's x-axis, b/a].

In Fig. 3.3 we try fitting the data with gaussians of different widths ($\sigma = 0.11$ and $\sigma = 0.42$, both being 1 standard deviation away from the best-fit σ), while keeping μ fixed at $\mu = 1.00$. The fit offered by $\sigma = 0.11$ is much poorer than those seen in Fig. 3.2; $\sigma = 0.42$ comes closer to fitting all the data, but still misses all the data points.

What can we infer from Figs. 3.2 and 3.3? The best-fit gaussian (solid line in Fig. 3.2) is skewed toward small axis ratios and predicts that 95% of KBOs have axis ratios $a/b \leq 1.48$ (within 2σ from the mean). This agrees reasonably well with the data which indicate that $\sim 85\%$ have axis ratios $a/b \leq 1.48$. However, the best-fit gaussian fails badly at larger a/b 's: it predicts that only 0.3% of

KBOs have axis ratios $a/b \geq 1.72$ (larger than 3σ from the mean), while the data indicate that $\sim 12\%$ have axis ratios in this range. Increasing μ to $\mu = 1.22$ (dashed line in Fig. 3.2) reduces some of this skewness but does not significantly improve the fit at larger a/b 's.

Keeping μ fixed and decreasing σ to $\sigma = 0.11$ (dotted line in Fig. 3.3) worsens the fit, as expected. Keeping μ fixed and increasing to $\sigma = 0.42$ (dashed line in Fig. 3.3) arguably produces the best fit yet (as judged by eye) since it tries to fit all the data points and does so equally well for all of them (or equally badly, depending on one's point of view). In short, none of the gaussians presented in Figs. 3.2 and 3.3 offers a good fit to the data. The conclusion to draw from the Figures is that the KBO shape distribution is not well approximated by a gaussian.

This is because the KBO shape distribution has two characteristics that cannot be met simultaneously by a standard gaussian: (1) a large fraction ($\sim 85\%$) has shapes that are close to spherical ($a/b \leq 1.5$), yet (2) there is a significant tail to the distribution ($\sim 12\%$) that has highly aspherical shapes ($a/b \geq 1.7$). In other words, most KBOs are nearly spherical, but a significant fraction is not. We note that, using a smaller data set, SJ02 came to the conclusion that a broad gaussian was needed to fit their available data. This is roughly consistent with our result here. With the benefit of a larger data sample, and the additional constraint from the detection probability p , we are able to improve SJ02's conclusion: the best description of the shape distribution is actually more like a moderately narrow peak with a long tail.

3.3.2 Power law distribution

Considering how poorly a gaussian fits the shape distribution, we try approximating $f(\tilde{a})$ with a power law, $f(\tilde{a}) \propto \tilde{a}^{-q}$. The solution is shown graphically in Fig. 3.4, where the thick horizontal line represents $p = 0.27$, and the solid black curve represents the detection probability p as a function of q :

$$p(\tilde{a})d\tilde{a} = \tilde{a}^{-q}d\tilde{a}. \quad (3.8)$$

In Eqn. (3.8), $p(\tilde{a})d\tilde{a}$ is the fraction of a KBO with axis ratios in the range \tilde{a} to $\tilde{a} + d\tilde{a}$. The probability is normalized so that the integral of $p(\tilde{a})$ from $\tilde{a} = 1$ to $\tilde{a} = 5$ is equal to 1. The shaded areas represent all possible values of p within its 1-, 2-, and 3σ error bars, so the allowed values of q are those that lie within these shaded areas. We note that the horizontal line and the curved line intersect at $q = 6.7$.

As was done in the previous section, we use the observed \tilde{a} 's to constrain q further. We compare the observed cumulative fractions of KBOs, as a function of \tilde{a} , with the cumulative fractions predicted by each possible q . A grid search is

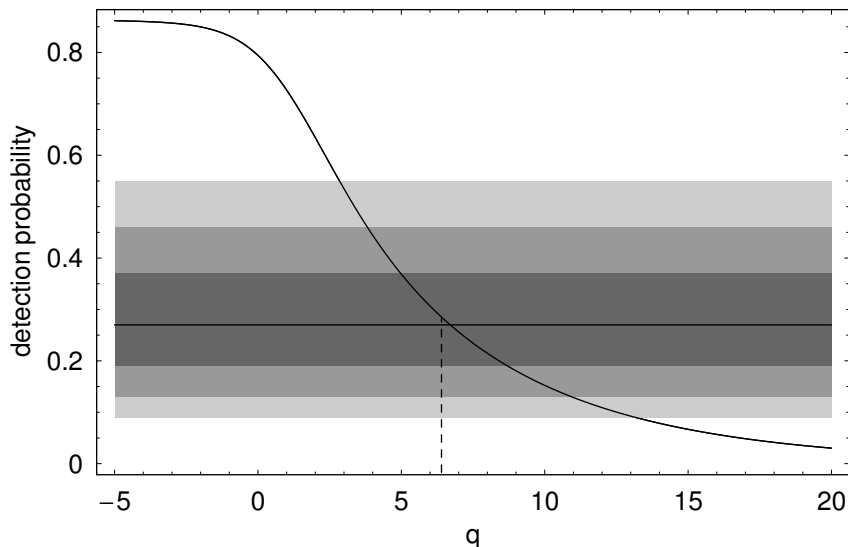


Figure 3.4 – The thick horizontal line represents all values of q that that give rise to $p = 0.27$. The shaded areas immediately adjacent to the line represent the p 's within the 1σ limits, the next shaded areas outward the 2σ limits, and the outermost shaded area the 3σ limits. The solid curve represents p as a function of the exponent q (Eqn. 3.8). The intersections of the shaded areas and the curve satisfy both Eqns. (3.2) and (3.8). The vertical line marks $q = 6.4$.

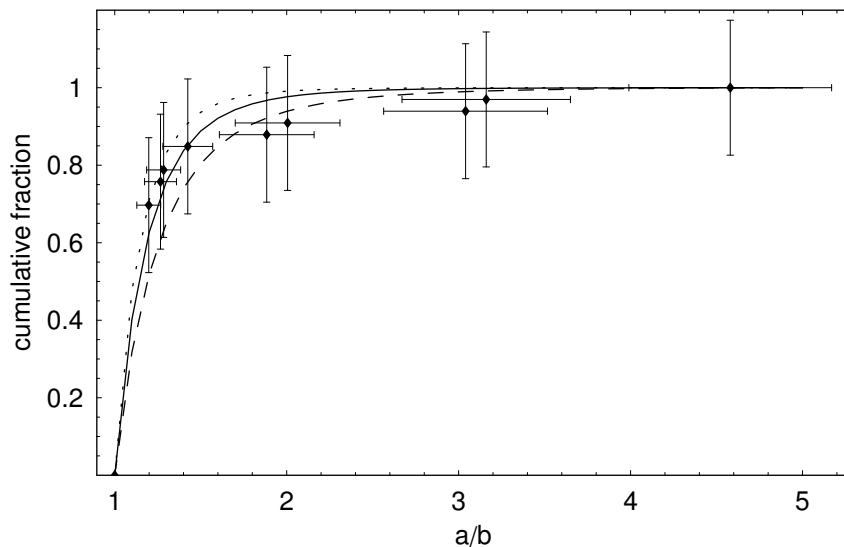


Figure 3.5 – Cumulative fractions of KBOs as a function of \tilde{a} . Same as Fig. 3.2, but this time with the curves representing power laws. The dotted line represents the exponent $q = 7.8$, solid line $q = 6.4$, and dashed line $q = 5.0$.

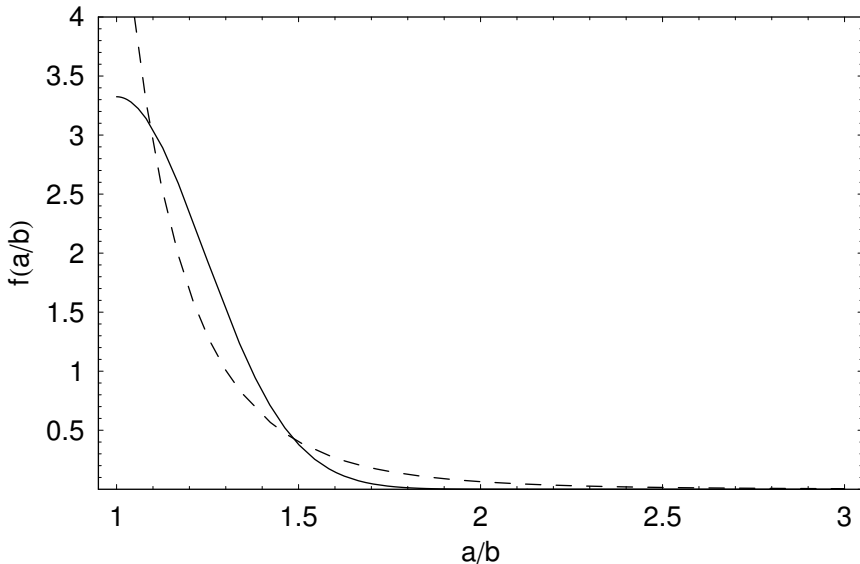


Figure 3.6 – Distribution of axis ratio \tilde{a} . The dashed line is the $q = 6.4$ power law (from Eqn. 3.9), the solid line a gaussian with $\mu = 1.00, \sigma = 0.24$ (from Eqn. 3.7). $f(\tilde{a})$ is normalized to 1 between $\tilde{a} = 1$ and $\tilde{a} = 5$.

performed through all possible values of q ; using χ^2 as the comparison criterion, we obtain the best-fit q :

$$q = 6.4 \pm 1.4 \text{ (1}\sigma \text{ error bars)}. \quad (3.9)$$

It is reassuring that χ^2 statistics yield $q = 6.4$ as the best fit, as this is very close to the $q = 6.7$ found independently by the Lacerda & Luu method. The fits offered by $q = 5.0, 6.4$ and 7.8 are shown in Fig. 3.5. It can be seen that the power laws generally fit the data better than the gaussians. The shape distribution $f(\tilde{a})$ as a gaussian and a power law is shown in Fig. 3.6.

As Fig. 3.6 shows, the KBO shape distribution is characterized by a large peak at small a/b 's, accompanied by a slow decline at larger a/b 's. The dominance of small a/b 's might be explained by (a) a preponderance of nearly spherical bodies, (b) a preponderance of very slow rotators whose lightcurve amplitudes could not be determined from the limited data, or some combination of these two factors. The likelihood of these scenarios will be evaluated in a future work. If the observational bias against slow rotators can be ruled out, the challenge will then be how to explain the dominance of nearly spherical bodies in the Kuiper Belt. As for the (small) fraction of KBOs with larger a/b 's, Jewitt & Sheppard (2002) and SJ02 have tentatively identified them as rotationally deformed "rubble piles," much like the "rubble piles" that have been proposed to exist among asteroids. If this hypothesis is correct, there should be a correlation between the

KBO shapes and spin rates (high spin rate \rightarrow large Δm). The data sample is as yet too small to confirm such a trend (e.g., see Fig. 13 of SJ02).

3.4 Summary

We have applied the method described in Lacerda & Luu (2003) to the available KBO lightcurve data to constrain the KBO shape distribution. The method assumes that the detectability of KBO lightcurves depends only on the KBO shape and the observing geometry; it does not take into account any spin frequency effect (e.g., the bias against very slow spinners). The results can be summarized as follows:

1. With 9 out of 33 reliable KBO lightcurves showing periodic brightness variations, the fraction of detectable KBO lightcurves is $f(\Delta m \geq 0.15) = 0.27$. This implies that the probability of detecting a KBO lightcurve is $p = 0.27_{-0.18}^{+0.28}$ (3σ error bars).
2. The KBO shape distribution has a steep peak at small axis ratios and drops off quickly to form a long tail: most of the distribution ($\sim 85\%$) has shapes that are close to spherical ($a/b \leq 1.5$), yet (2) there is also a significant fraction ($\sim 12\%$) that has highly aspherical shapes ($a/b \geq 1.7$).
3. Fitting the KBO a/b distribution with a gaussian yields the best-fit mean $\mu = 1.00(+0.22)$ and standard deviation $\sigma = 0.24_{-0.13}^{+0.18}$ (1σ error bars). However, this gaussian is strongly skewed toward small axis ratios ($a/b \leq 1.5$), and offers a bad fit for larger axis ratios. Increasing the standard deviation reduces the skewness, but then all data points are fitted equally poorly.
4. The KBO a/b distribution is better fitted with power law distributions of the form $f(a/b) \sim (a/b)^{-q}$, with the best-fit exponent $q = 6.4 \pm 1.4$ (1σ error bars).

Acknowledgments

We thank Ronnie Hoogerwerf and Dave Jewitt for helpful discussion; we especially appreciate RH's expertise with L^AT_EX and SM. PL also thanks Scott Kenyon for a very fruitful and enjoyable visit to the Center for Astrophysics.

References

- Brown, R. H., Cruikshank, D. P., & Pendleton, Y. 1999, *ApJ*, 519, L101
- Collander-Brown, S. J., Fitzsimmons, A., Fletcher, E., Irwin, M. J., & Williams, I. P. 1999, *MNRAS*, 308, 588
- Davies, J. K., McBride, N., & Green, S. F. 1997, *Icarus*, 125, 61
- Green, S. F., McBride, N., O Ceallaigh, D. P., Fitzsimmons, A., Williams, I. P., & Irwin, M. J. 1997, *MNRAS*, 290, 186
- Hainaut, O. R., et al. 2000, *A&A*, 356, 1076
- Jewitt, D. C. & Luu, J. X. 2001, *AJ*, 122, 2099
- Jewitt, D. C. & Sheppard, S. S. 2002, *AJ*, 123, 2110
- Lacerda, P. & Luu, J. 2003, *Icarus*, 161, 174
- Luu, J. & Jewitt, D. 1996, *AJ*, 112, 2310
- Luu, J. X. & Jewitt, D. C. 1998, *ApJ*, 494, L117
- Ortiz, J. L., Lopez-Moreno, J. J., Gutierrez, P. J., & Baumont, S. 2001, *Bulletin of the American Astronomical Society*, 33, 1047
- Romanishin, W. & Tegler, S. C. 1999, *Nature*, 398, 129
- Romanishin, W., Tegler, S. C., Rettig, T. W., Consolmagno, G., & Botthof, B. 2001, *Bulletin of the American Astronomical Society*, 33, 1031
- Sheppard, S. S. & Jewitt, D. C. 2002, *AJ*, 124, 1757
- Sheppard, S. S. & Jewitt, D. C. 2003, *Earth Moon and Planets*, 92, 207
- Tegler, S. C. & Romanishin, W. 2000, *Nature*, 407, 979

Analysis of the rotational properties

ABSTRACT

We use optical data of 10 Kuiper Belt objects (KBOs) to investigate their rotational properties. Of the 10, three (30%) exhibit light variations with amplitude $\Delta m \geq 0.15$ mag, and 1 out of 10 (10%) has $\Delta m \geq 0.40$ mag, which is in good agreement with previous surveys. These data, in combination with the existing database, are used to discuss the rotational periods, shapes, and densities of Kuiper Belt objects. We find that, in the sampled size range, Kuiper Belt objects have a higher fraction of low amplitude lightcurves and rotate slower than main belt asteroids. The data also show that the rotational properties and the shapes of KBOs depend on size. If we split the database of KBO rotational properties into two size ranges with diameter *larger* and *smaller* than 400 km, we find that: (1) the mean lightcurve amplitudes of the two groups are different with 98.5% confidence, (2) the corresponding power-law shape distributions are different, and (3) the two groups occupy different regions on a *spin period* vs. *lightcurve amplitude* diagram. These differences are interpreted in the context of KBO collisional evolution.

Pedro Lacerda and Jane Luu
to be submitted to Icarus

4.1 Introduction

THE Kuiper Belt (KB) is an assembly of small icy objects, orbiting the Sun beyond Neptune. Kuiper Belt objects (KBOs) are likely to be remnants of outer solar system planetesimals (Jewitt & Luu 1993). Their physical, chemical, and dynamical properties should therefore provide valuable information regarding both the environment and the physical processes responsible for planet formation.

At the time of writing, 763 KBOs are known, with 363 of them having been followed for more than one opposition. A total of $\approx 10^5$ objects larger than 50 km are thought to orbit the Sun beyond Neptune (Jewitt & Luu 2000). Studies of KB orbits has revealed an intricate dynamical structure, with signatures of interactions with Neptune (Malhotra 1995). The size distribution follows a differential power-law of index $q = 4$ for bodies $\gtrsim 50$ km (Trujillo et al. 2001a), becoming slightly shallower at smaller sizes (Bernstein et al. 2004).

KBO colours show a large diversity, from slightly blue to very red (Luu & Jewitt 1996; Tegler & Romanishin 2000; Jewitt & Luu 2001), and seem to correlate with inclination and perihelion distance (e.g., Jewitt & Luu 2001; Doressoundiram et al. 2002; Trujillo & Brown 2002). The few low-resolution optical and near-IR KBO spectra are mostly featureless, with the exception of a weak $2\ \mu\text{m}$ water ice absorption line present in some of them (Brown et al. 1999; Jewitt & Luu 2001).

About 4% of known KBOs are binaries with separations larger than $0''.15$ (Noll et al. 2002). All the observed binaries have primary-to-secondary mass ratios ≈ 1 . Two binary creation models have been proposed. Weidenschilling (2002) favours the idea that binaries form in three-body encounters. This model requires a 100 times denser Kuiper Belt at the epoch of binary formation, and predicts a higher abundance of large separation binaries. The alternative scenario (Goldreich et al. 2002), in which the energy needed to bind the orbits of two approaching bodies is drawn from the surrounding swarm of smaller objects, also requires a much higher density of KBOs than the present, but it predicts a larger fraction of close binaries. Recently, Sheppard & Jewitt (2004) have shown evidence that 2001 QG₂₉₈ could be a close or contact binary KBO, and estimated the fraction of similar objects in the Belt to be $\sim 10\%$ – 20% .

Other physical properties of KBOs, such as their shapes, densities, and albedos, are still poorly constrained. This is mainly because KBOs are extremely faint, with mean apparent red magnitude $m_R \sim 23$ (Trujillo et al. 2001b).

The study of KBO rotational properties through time-series broadband optical photometry has proved to be the most successful technique to date to investigate some of these physical properties. Light variations of KBOs are believed to be caused mainly by their aspherical shape: as KBOs rotate in space, their projected cross-sections change, resulting in periodic brightness variations.

One of the best examples to date of a KBO lightcurve—and what can be learned from it—is that of (20000) Varuna (Jewitt & Sheppard 2002). The authors explain the lightcurve of Varuna as a consequence of its elongated shape (axes ratio, $a/b \sim 1.5$). They further argue that the object is centripetally deformed by rotation because of its low density, “rubble pile” structure. The term “rubble pile” is generally used to refer to gravitationally bound aggregates of smaller fragments. The existence of rubble piles is thought to be due to continuing mutual collisions throughout the age of the solar system, which gradually fracture the interiors of objects. Rotating rubble piles can adjust their shapes to balance centripetal acceleration and self-gravity. The resulting equilibrium shapes have been studied in the extreme case of fluid bodies, and depend on the body’s density and spin rate (Chandrasekhar 1969).

Lacerda & Luu (2003, hereafter LL03a) showed that under reasonable assumptions the fraction of KBOs with detectable lightcurves can be used to constrain the shape distribution of these objects. A follow-up (Luu & Lacerda 2003, hereafter LL03b) on this work, using a database of lightcurve properties of 33 KBOs (Sheppard & Jewitt 2002, 2003), shows that although most Kuiper Belt objects ($\sim 85\%$) have shapes that are close to spherical ($a/b \leq 1.5$) there is a significant fraction ($\sim 12\%$) with highly aspherical shapes ($a/b \geq 1.7$).

In this paper we use optical data of 10 KBOs to investigate the amplitudes and periods of their lightcurves. These data are used in combination with the existing database to investigate the distributions of KBO spin periods and shapes. We discuss their implications for the inner structure and collisional evolution of objects in the Kuiper Belt.

4.2 Observations and Photometry

We collected time-series optical data of 10 KBOs at the Isaac Newton 2.5m (INT) and William Herschel 4m (WHT) telescopes. The INT Wide Field Camera (WFC) is a mosaic of 4 EEV 2048×4096 CCDs, each with a pixel scale of $0''.33/\text{pixel}$ and spanning approximately $11'.3 \times 22'.5$ in the plane of the sky. The targets are imaged through a Johnson R filter. The WHT prime focus camera consists of 2 EEV 2048×4096 CCDs with a pixel scale of $0''.24/\text{pixel}$, and covers a sky-projected area of $2 \times 8'.2 \times 16'.4$. With this camera we used a Harris R filter. The seeing for the whole set of observations ranged from 1.0 to $1.9''$ FWHM. We tracked both telescopes at sidereal rate and kept integration times for each object sufficiently short to avoid errors in the photometry due to trailing effects (see Table 4.1). No light travel time corrections have been made.

We reduced the data using standard techniques. The sky background in the flat-fielded images shows variations of less than 1% across the chip. Background variations between consecutive nights were less than 5% for most of the data. Cosmic rays were removed with the package LA-Cosmic (van Dokkum 2001).

Table 4.1 – Observing Conditions and Geometry

Object	Designation	ObsDate ^a	Tel. ^b	Seeing ^c ["]	MvtRt ^d ["/hr]	ITime ^e [sec]	RA ^f [hhmmss]	dec ^g [°"]	R ^h [AU]	Δ ⁱ [AU]	α ^j [deg]
(19308)	1996 TO ₆₆	01-Oct-99	WHT	1.8	2.89	500	23 59 46	+03 36 42	45.950	44.958	0.1594
	1996 TS ₆₆	30-Sep-99	WHT	1.3	2.62	400,600	02 26 06	+21 41 03	38.778	37.957	0.8619
	1996 TS ₆₆	01-Oct-99	WHT	1.1	2.67	600	02 26 02	+21 40 50	38.778	37.948	0.8436
	1996 TS ₆₆	02-Oct-99	WHT	1.5	2.70	600,900	02 25 58	+21 40 35	38.778	37.939	0.8225
(35671)	1998 SN ₁₆₅	29-Sep-99	WHT	1.5	3.24	360,400	23 32 46	−01 18 15	38.202	37.226	0.3341
(35671)	1998 SN ₁₆₅	30-Sep-99	WHT	1.4	3.22	360	23 32 41	−01 18 47	38.202	37.230	0.3594
(19521)	Chaos	01-Oct-99	WHT	1.0	1.75	360,400,600	03 44 37	+21 30 58	42.399	41.766	1.0616
(19521)	Chaos	02-Oct-99	WHT	1.5	1.79	400,600	03 44 34	+21 30 54	42.399	41.755	1.0484
	1999 DF ₉	13-Feb-01	WHT	1.7	3.19	900	10 27 04	+09 45 16	39.782	38.818	0.3124
	1999 DF ₉	14-Feb-01	WHT	1.6	3.21	900	10 26 50	+09 46 25	39.783	38.808	0.2436
	1999 DF ₉	15-Feb-01	WHT	1.4	3.22	900	10 26 46	+09 46 50	39.783	38.806	0.2183
	2000 CM ₁₀₅	11-Feb-01	WHT	1.5	3.14	600,900	09 18 48	+19 41 59	41.753	40.774	0.1687
	2000 CM ₁₀₅	13-Feb-01	WHT	1.4	3.12	900	09 18 39	+19 42 40	41.753	40.778	0.2084
	2000 CM ₁₀₅	14-Feb-01	WHT	1.5	3.11	900	09 18 34	+19 43 02	41.753	40.781	0.2303
	1999 RZ ₂₅₃	11-Sep-01	INT	1.9	2.86	600	22 02 57	−12 31 06	40.963	40.021	0.4959
	1999 RZ ₂₅₃	12-Sep-01	INT	1.4	2.84	600	22 02 53	−12 31 26	40.963	40.026	0.5156
	1999 RZ ₂₅₃	13-Sep-01	INT	1.8	2.82	600	22 02 49	−12 31 49	40.963	40.033	0.5381
(47171)	1999 TC ₃₆	11-Sep-01	INT	1.9	3.85	600	00 16 49	−07 34 59	31.416	30.440	0.4605
(47171)	1999 TC ₃₆	12-Sep-01	INT	1.4	3.86	900	00 16 45	−07 35 33	31.416	30.437	0.4359
(47171)	1999 TC ₃₆	13-Sep-01	INT	1.8	3.88	900	00 16 39	−07 36 13	31.416	30.434	0.4122
(38628)	Huya	28-Feb-01	INT	1.5	2.91	600	13 31 13	−00 39 04	29.769	29.021	1.2725
(38628)	Huya	01-Mar-01	INT	1.8	2.97	360	13 31 09	−00 38 23	29.768	29.009	1.2479
(38628)	Huya	03-Mar-01	INT	1.5	3.08	360	13 31 01	−00 36 59	29.767	28.987	1.1976
	2001 CZ ₃₁	01-Mar-01	INT	1.3	2.72	600,900	09 00 03	+16 29 23	41.394	40.522	0.6525
	2001 CZ ₃₁	03-Mar-01	INT	1.4	2.65	600,900	08 59 54	+16 30 04	41.394	40.539	0.6954

^a UT date of observation; ^b Telescope used for observations; ^c Average seeing of the data ["]; ^d Average rate of motion of KBO ["/hr]; ^e Integration times used; ^f Right ascension; ^g Declination; ^h KBO–Sun distance; ⁱ KBO–Earth distance; ^j Phase angle (Sun–Object–Earth angle) of observation.

Object Designation	Class ^a	H^b [mag]	i^c [deg]	e^d	a^e [AU]
(19308) 1996 TO ₆₆	C	4.5	27.50	0.12	43.20
1996 TS ₆₆	C	6.4	7.30	0.13	44.00
(35671) 1998 SN ₁₆₅	C ¹	5.8	4.60	0.05	37.80
(19521) Chaos	C	4.9	12.00	0.11	45.90
1999 DF ₉	C	6.1	9.80	0.15	46.80
2000 CM ₁₀₅	C	6.2	3.80	0.07	42.50
1999 RZ ₂₅₃	C	5.9	0.60	0.09	43.60
(47171) 1999 TC ₃₆	Pb	4.9	8.40	0.22	39.30
(38628) Huya	P	4.7	15.50	0.28	39.50
2001 CZ ₃₁	C	5.4	10.20	0.12	45.60

Table 4.2 – Properties of Observed KBOs. ^aDynamical class (C = classical KBO, P = Plutino, b = binary KBO); ^bAbsolute magnitude; ^cOrbital inclination; ^dOrbital eccentricity; ^eSemi-major axis.

We performed aperture photometry on all objects in the field using the SExtractor software package (Bertin & Arnouts 1996). This software performs circular aperture measurements on each object in a frame, and puts out a catalog of both the magnitudes and the associated errors. Below we describe how we obtained a better estimate of the errors. We used apertures ranging from 1.5 to 2.0 times the FWHM for each frame and selected the aperture that maximized signal-to-noise. An extra aperture of 5 FWHMs was used to look for possible seeing dependent trends in our photometry. The catalogs were matched by selecting only the objects that are present in all frames. The slow movement of KBOs from night to night allows us to successfully match a large number of stars in consecutive nights. We discarded all saturated objects as well as those identified to be galaxies.

The KBO lightcurves were obtained from differential photometry with respect to the brightest non-variable field stars. An average of the magnitudes of the brightest stars (the "reference" stars) provides a reference for differential photometry in each frame. This method allows for small amplitude brightness variations to be detected even under non-photometric conditions.

The uncertainty in the relative photometry was calculated from the scatter in the photometry of fainter field stars that are similar to the KBOs in brightness (the "comparison" stars, see Fig.4.1). This error estimate is more robust than the errors provided by SExtractor (see below), and was used to verify the accuracy of the latter. This procedure resulted in consistent time series brightness data for ~ 100 objects (KBO + field stars) in a time span of 2–3 consecutive nights.

We observed Landolt standard stars whenever conditions were photometric, and used them to calibrate the zero point of the magnitude scale. The extinction coefficient was obtained from the reference stars.

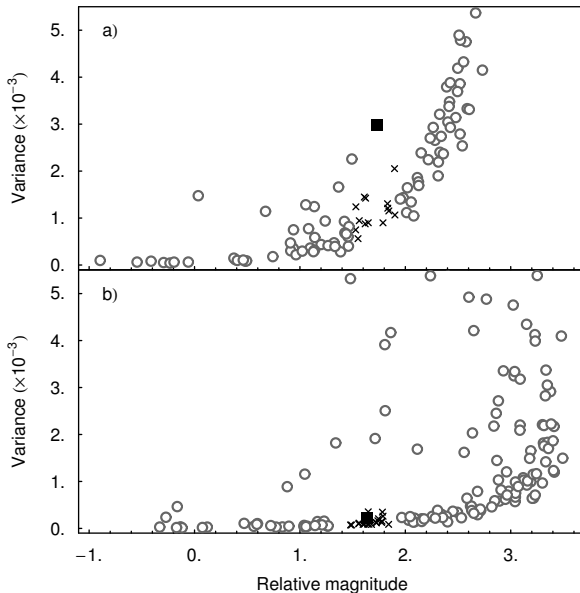


Figure 4.1 – Frame-to-frame photometric variances of all stars (gray circles and black crosses) in the 1998 SN₁₆₅ (a) and Huya (b) fields, plotted against their relative magnitude. The trend of increasing photometric variability with increasing magnitude is clear. The intrinsically variable stars clearly do not follow this trend, and are located towards the upper left region of the plot. The KBOs are shown as black squares. 1998 SN₁₆₅, in the top panel shows a much larger variability than the comparison stars (shown as crosses, see Section 4.3.1), while Huya is well within the expected variance range, given its magnitude.

UT Date	Julian Date	m_R [mag]
1999 Oct 1.84831	2451453.34831	21.24 ± 0.07
1999 Oct 1.85590	2451453.35590	21.30 ± 0.07
1999 Oct 1.86352	2451453.36352	21.20 ± 0.07
1999 Oct 1.87201	2451453.37201	21.22 ± 0.07
1999 Oct 1.87867	2451453.37867	21.21 ± 0.07
1999 Oct 1.88532	2451453.38532	21.28 ± 0.07
1999 Oct 1.89302	2451453.39302	21.27 ± 0.06
1999 Oct 1.90034	2451453.40034	21.30 ± 0.06
1999 Oct 1.90730	2451453.40730	21.28 ± 0.06
1999 Oct 1.91470	2451453.41470	21.31 ± 0.06

Table 4.3 – Photometric measurements of 1996 TO₆₆. Columns are UT date at the start of the exposure, Julian date at the start of the exposure, and apparent red magnitude. The errors include the uncertainties in relative and absolute photometry added quadratically.

Since not all nights were photometric the lightcurves are presented as variations with respect to the mean brightness. These yield the correct amplitudes and periods of the lightcurves but do not provide their absolute magnitudes.

The orbital parameters and other properties of the observed KBOs are given in Table 4.2. Tables 4.3, 4.4, 4.5, and 4.6 list the absolute R -magnitude photometric measurements obtained for 1996 TO₆₆, 1996 TS₆₆, 1998 SN₁₆₅, and Chaos, respectively.

4.3 Lightcurve Analysis

The results in this paper depend solely on the amplitude and period of the KBO lightcurves. It is therefore important to accurately determine these parameters and the associated uncertainties.

Table 4.4 – Photometric measurements of 1996 TS₆₆. Columns are UT date at the start of the exposure, Julian date at the start of the exposure, and apparent red magnitude. The errors include the uncertainties in relative and absolute photometry added quadratically.

UT Date	Julian Date	m_R [mag]
1999 Sep 30.06087	2451451.56087	21.94 ± 0.07
1999 Sep 30.06628	2451451.56628	21.83 ± 0.07
1999 Sep 30.07979	2451451.57979	21.76 ± 0.07
1999 Sep 30.08529	2451451.58529	21.71 ± 0.07
1999 Sep 30.09068	2451451.59068	21.75 ± 0.07
1999 Sep 30.09695	2451451.59695	21.67 ± 0.07
1999 Sep 30.01250	2451451.60250	21.77 ± 0.07
1999 Sep 30.10936	2451451.60936	21.76 ± 0.06
1999 Sep 30.11705	2451451.61705	21.80 ± 0.06
1999 Sep 30.12486	2451451.62486	21.77 ± 0.06
1999 Sep 30.13798	2451451.63798	21.82 ± 0.07
1999 Sep 30.14722	2451451.64722	21.74 ± 0.06
1999 Sep 30.15524	2451451.65524	21.72 ± 0.06
1999 Sep 30.16834	2451451.66834	21.72 ± 0.08
1999 Sep 30.17680	2451451.67680	21.83 ± 0.07
1999 Sep 30.18548	2451451.68548	21.80 ± 0.06
1999 Sep 30.19429	2451451.69429	21.74 ± 0.07
1999 Sep 30.20212	2451451.70212	21.78 ± 0.07
1999 Sep 30.21010	2451451.71010	21.72 ± 0.07
1999 Sep 30.21806	2451451.71806	21.76 ± 0.09
1999 Sep 30.23528	2451451.73528	21.73 ± 0.07
1999 Sep 30.24355	2451451.74355	21.74 ± 0.08
1999 Oct 01.02002	2451452.52002	21.81 ± 0.06
1999 Oct 01.02799	2451452.52799	21.82 ± 0.06
1999 Oct 01.03648	2451452.53648	21.81 ± 0.06
1999 Oct 01.04422	2451452.54422	21.80 ± 0.06
1999 Oct 01.93113	2451453.43113	21.71 ± 0.06
1999 Oct 01.94168	2451453.44168	21.68 ± 0.06
1999 Oct 01.95331	2451453.45331	21.73 ± 0.06
1999 Oct 01.97903	2451453.47903	21.69 ± 0.06
1999 Oct 01.99177	2451453.49177	21.74 ± 0.06
1999 Oct 02.00393	2451453.50393	21.73 ± 0.05
1999 Oct 02.01588	2451453.51588	21.78 ± 0.05
1999 Oct 02.02734	2451453.52734	21.71 ± 0.05

4.3.1 Can we detect the KBO brightness variation?

We begin by investigating if the observed brightness variations are intrinsic to the KBO, i.e., if the KBOs intrinsic brightness variations are detectable given our uncertainties. This was done by comparing the frame-to-frame scatter in the KBO optical data with that of ($\sim 10 - 20$) comparison stars.

To visually compare the scatter in the magnitudes of the reference stars (see Section 4.2), comparison stars, and KBOs, we plot a histogram of their frame-to-frame variances (see Fig. 4.2). In general such a histogram should show the reference stars clustered at the lowest variances, followed by the comparison stars spread over larger variances. If the KBO appears isolated at much higher variances than both groups of stars (e.g., Fig. 4.2-j), then its brightness modulations are significant. Conversely, if the KBO is clustered with the stars (e.g. Fig. 4.2-f), any periodic brightness variations would be below the detection threshold.

Figure 4.1 shows the dependence of the uncertainties on magnitude. Objects that do not fall on the rising curve traced out by the stars must have intrinsic

UT Date	Julian Date	m_R [mag]
1999 Sep 29.87384	2451451.37384	21.20 ± 0.06
1999 Sep 29.88050	2451451.38050	21.19 ± 0.05
1999 Sep 29.88845	2451451.38845	21.18 ± 0.05
1999 Sep 29.89811	2451451.39811	21.17 ± 0.05
1999 Sep 29.90496	2451451.40496	21.21 ± 0.05
1999 Sep 29.91060	2451451.41060	21.24 ± 0.05
1999 Sep 29.91608	2451451.41608	21.18 ± 0.05
1999 Sep 29.92439	2451451.42439	21.25 ± 0.05
1999 Sep 29.93055	2451451.43055	21.24 ± 0.05
1999 Sep 29.93712	2451451.43712	21.26 ± 0.06
1999 Sep 29.94283	2451451.44283	21.25 ± 0.06
1999 Sep 29.94821	2451451.44821	21.28 ± 0.06
1999 Sep 29.96009	2451451.46009	21.25 ± 0.06
1999 Sep 29.96640	2451451.46640	21.21 ± 0.06
1999 Sep 29.97313	2451451.47313	21.17 ± 0.05
1999 Sep 29.97850	2451451.47850	21.14 ± 0.05
1999 Sep 29.98373	2451451.48373	21.12 ± 0.06
1999 Sep 29.98897	2451451.48897	21.15 ± 0.06
1999 Sep 29.99469	2451451.49469	21.15 ± 0.06
1999 Sep 29.99997	2451451.49997	21.16 ± 0.06
1999 Sep 30.00521	2451451.50521	21.12 ± 0.06
1999 Sep 30.01144	2451451.51144	21.09 ± 0.06
1999 Sep 30.02164	2451451.52164	21.18 ± 0.06
1999 Sep 30.02692	2451451.52692	21.17 ± 0.06
1999 Sep 30.84539	2451452.34539	21.32 ± 0.06
1999 Sep 30.85033	2451452.35033	21.30 ± 0.06
1999 Sep 30.85531	2451452.35531	21.28 ± 0.06
1999 Sep 30.86029	2451452.36029	21.31 ± 0.06
1999 Sep 30.86550	2451452.36550	21.21 ± 0.06
1999 Sep 30.87098	2451452.37098	21.26 ± 0.06
1999 Sep 30.87627	2451452.37627	21.28 ± 0.06
1999 Sep 30.89202	2451452.39202	21.23 ± 0.05
1999 Sep 30.89698	2451452.39698	21.30 ± 0.06
1999 Sep 30.90608	2451452.40608	21.20 ± 0.05
1999 Sep 30.91191	2451452.41191	21.26 ± 0.05
1999 Sep 30.92029	2451452.42029	21.15 ± 0.05
1999 Sep 30.92601	2451452.42601	21.19 ± 0.05
1999 Sep 30.93110	2451452.43110	21.14 ± 0.05
1999 Sep 30.93627	2451452.43627	21.16 ± 0.05
1999 Sep 30.94858	2451452.44858	21.18 ± 0.05
1999 Sep 30.95363	2451452.45363	21.16 ± 0.05
1999 Sep 30.95852	2451452.45852	21.13 ± 0.05
1999 Sep 30.96347	2451452.46347	21.17 ± 0.05
1999 Sep 30.96850	2451452.46850	21.16 ± 0.05
1999 Sep 30.97422	2451452.47422	21.18 ± 0.05
1999 Sep 30.98431	2451452.48431	21.18 ± 0.05
1999 Sep 30.98923	2451452.48923	21.17 ± 0.06
1999 Sep 30.99444	2451452.49444	21.16 ± 0.05
1999 Sep 30.99934	2451452.49934	21.20 ± 0.05
1999 Oct 01.00424	2451452.50424	21.16 ± 0.05
1999 Oct 01.00992	2451452.50992	21.18 ± 0.06

Table 4.5 – Photometric measurements of 1998SN₁₆₅. Columns are UT date at the start of the exposure, Julian date at the start of the exposure, and apparent red magnitude. The errors include the uncertainties in relative and absolute photometry added quadratically.

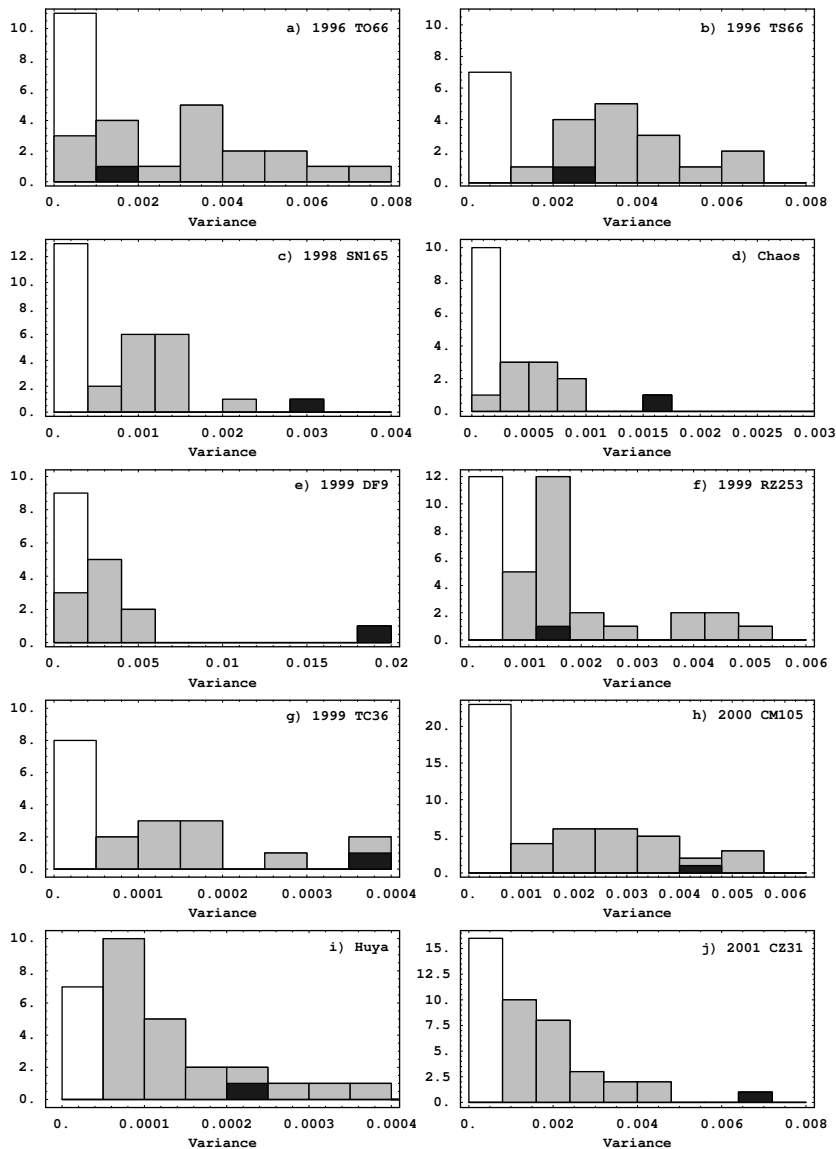


Figure 4.2 – Stacked histograms of the frame-to-frame variance in the optical data of the “reference” stars (in white), “comparison” stars (in gray), and the KBO (in black). In c), e), and j) the KBO shows significantly more variability than the comparison stars, whereas in all other cases it falls well within the range of photometric uncertainties of the stars of similar brightness.

UT Date	Julian Date	m_R [mag]
1999 Oct 01.06329	2451452.56329	20.82 ± 0.06
1999 Oct 01.06831	2451452.56831	20.80 ± 0.06
1999 Oct 01.07324	2451452.57324	20.80 ± 0.06
1999 Oct 01.07817	2451452.57817	20.81 ± 0.06
1999 Oct 01.08311	2451452.58311	20.80 ± 0.06
1999 Oct 01.08801	2451452.58801	20.76 ± 0.06
1999 Oct 01.09370	2451452.59370	20.77 ± 0.06
1999 Oct 01.14333	2451452.64333	20.71 ± 0.06
1999 Oct 01.15073	2451452.65073	20.68 ± 0.06
1999 Oct 01.15755	2451452.65755	20.70 ± 0.06
1999 Oct 01.16543	2451452.66543	20.72 ± 0.06
1999 Oct 01.17316	2451452.67316	20.72 ± 0.06
1999 Oct 01.18112	2451452.68112	20.71 ± 0.06
1999 Oct 01.18882	2451452.68882	20.73 ± 0.06
1999 Oct 01.19652	2451452.69652	20.70 ± 0.06
1999 Oct 01.20436	2451452.70436	20.69 ± 0.06
1999 Oct 01.21326	2451452.71326	20.72 ± 0.06
1999 Oct 01.21865	2451452.71865	20.72 ± 0.06
1999 Oct 01.22402	2451452.72402	20.74 ± 0.06
1999 Oct 01.22938	2451452.72938	20.72 ± 0.06
1999 Oct 01.23478	2451452.73478	20.71 ± 0.07
1999 Oct 01.24022	2451452.74022	20.72 ± 0.07
1999 Oct 02.04310	2451453.54310	20.68 ± 0.06
1999 Oct 02.04942	2451453.54942	20.69 ± 0.06
1999 Oct 02.07568	2451453.57568	20.74 ± 0.07
1999 Oct 02.08266	2451453.58266	20.73 ± 0.06
1999 Oct 02.09188	2451453.59188	20.74 ± 0.06
1999 Oct 02.10484	2451453.60484	20.75 ± 0.06
1999 Oct 02.11386	2451453.61386	20.77 ± 0.06
1999 Oct 02.12215	2451453.62215	20.77 ± 0.06
1999 Oct 02.13063	2451453.63063	20.78 ± 0.06
1999 Oct 02.13982	2451453.63982	20.79 ± 0.06
1999 Oct 02.14929	2451453.64929	20.71 ± 0.07

Table 4.6 – Photometric measurements of Chaos. Columns are UT date at the start of the exposure, Julian date at the start of the exposure, and apparent red magnitude. The errors include the uncertainties in relative and absolute photometry added quadratically.

sic brightness variations. By calculating the mean and spread of the variance for the comparison stars (shown as crosses) we can calculate our photometric uncertainties and thus determine whether the KBO brightness variations are significant.

4.3.2 Period determination

In the cases where significant brightness variations were detected in the light-curves, the phase dispersion minimization method was used (PDM, Stellingwerf 1978) to look for periodicities in the data. For each test period PDM computes a statistical parameter θ that compares the spread of data points in phase bins with the overall spread of the data. The period that best fits the data is the one that minimizes θ . The advantages of PDM are that it is non-parametric, i.e., it does not assume a shape for the lightcurve, and it can handle unevenly spaced data. Each data set was tested for periods ranging from 2 to 24 hours, in steps of 0.01 hr.

Table 4.7 – Lightcurve Properties of Observed KBOs. ^aMean red magnitude. Errors include uncertainties in relative and absolute photometry added quadratically; ^bNumber of nights with useful data. Numbers in brackets indicate number of nights of data from other observers used for period determination. Data for 1998 SN₁₆₅ taken from Peixinho et al. (2002) and data for 2001 CZ₃₁ taken from SJ02; ^cLightcurve amplitude; ^dLightcurve period.

Object Designation	m_R^a [mag]	Nts ^b	Δm_R^c [mag]	P^d [hr]
(35671) 1998 SN ₁₆₅	21.20±0.05	2(1)	0.16±0.01	8.84
1999 DF ₉	–	3	0.40±0.02	6.65
2001 CZ ₃₁		2(1)	0.21±0.02	4.71
(19308) 1996 TO ₆₆	21.26±0.06	1	?	
1996 TS ₆₆	21.76±0.05	3	<0.15	
(19521) Chaos	20.74±0.06	2	<0.10	
2000 CM ₁₀₅	–	2	<0.14	
1999 RZ ₂₅₃	–	3	<0.05	
(47171) 1999 TC ₃₆	–	3	<0.07	
(38628) Huya	–	2	<0.04	

4.3.3 Amplitude determination

We used a Monte Carlo experiment to determine the amplitude of the lightcurves for which a period was found. We generated several artificial data sets by randomizing each point within the error bar. Each artificial data set was fitted with a Fourier series, using the best-fit period, and the mode and central 68% of the distribution of amplitudes were taken as the lightcurve amplitude and 1σ uncertainty, respectively.

For the "null" lightcurves, i.e. those where no significant variation was detected, we subtracted the typical error bar size from the total amplitude of the data to obtain an upper limit to the amplitude of the KBO photometric variation.

In this section we present the results of the lightcurve analysis for each of the observed KBOs. We found significant brightness variations ($\Delta m > 0.15$ mag) for 3 out of 10 KBOs (30%), and $\Delta m \geq 0.40$ mag for 1 out of 10 (10%). This is consistent with previously published results: SJ02 found a fraction of 31% with $\Delta m > 0.15$ mag and 23% with $\Delta m > 0.40$ mag, both consistent with our results. The other 7 KBOs do not show detectable variations. The results are summarized in Table 4.7.

4.4 Results

4.4.1 1998 SN₁₆₅

The brightness of 1998 SN₁₆₅ varies significantly ($> 5\sigma$) more than that of the comparison stars (see Figs. 4.1 and 4.2-c). The periodogram for this KBO shows a very broad minimum around $P = 9$ hr (Fig. 4.3a). The degeneracy implied by the broad minimum would only be resolved with additional data. A slight weaker minimum is seen at $P = 6.5$ hr, which is close to a 24hr alias of 9 hr.

Peixinho et al. (2002, hereafter PDR02) observed this object in September 2000, but having only one night's worth of data, they did not succeed in determining this object's rotational period unambiguously. We used their data to solve the degeneracy in our PDM result. The PDR02 data have not been absolutely calibrated, and the magnitudes are given relative to a bright field star. To be able to combine it with our own data we had to subtract the mean magnitudes. Our periodogram of 1998 SN₁₆₅ (centered on the broad minimum) is shown in Fig. 4.3b and can be compared with the revised periodogram obtained with our data combined with the PDR02 data (Fig. 4.3c). The minima become much clearer with the additional data, but because of the 1-year time difference between the two observational campaigns, many close aliases appear in the periodogram. The absolute minimum, at $P = 8.84$ hr, corresponds to a double peaked lightcurve (see Fig. 4.4). The second best fit, $P = 8.7$ hr, produces a more scattered phase plot, in which the peak in the PDR02 data coincides with our night 2. We will use $P = 8.84$ hr in the rest of the paper, as this corresponds to the PDM absolute minimum.

The amplitude, obtained using the Monte Carlo method described in Section 4.3.3, is $\Delta m = 0.16 \pm 0.01$ mag. This value was calculated using only our data, but it did not change when recalculated adding the PDR02 data.

4.4.2 1999 DF₉

1999 DF₉ shows large amplitude photometric variations ($\Delta m_R \sim 0.4$ mag). The PDM periodogram for 1999 DF₉ is shown in Fig. 4.5. The best-fit period is $P = 6.65$ hr, which corresponds to a double-peak lightcurve (Fig. 4.6). Other PDM minima are found close to $P/2 \approx 3.3$ hr and 9.2 hr, a 24 hr alias of the best period. Phasing the data with $P/2$ results in a worse fit because the two minima of the double peaked lightcurve exhibit significantly different morphologies (Fig. 4.6); the peculiar shape of the brighter minimum, which is reproduced on two different nights, may be caused by an effect other than shape, e.g., a darker (lower albedo) region on the KBO's surface.

The amplitude of the lightcurve, estimated as described in Section 4.3.3, is $\Delta m_R = 0.4 \pm 0.02$ mag.

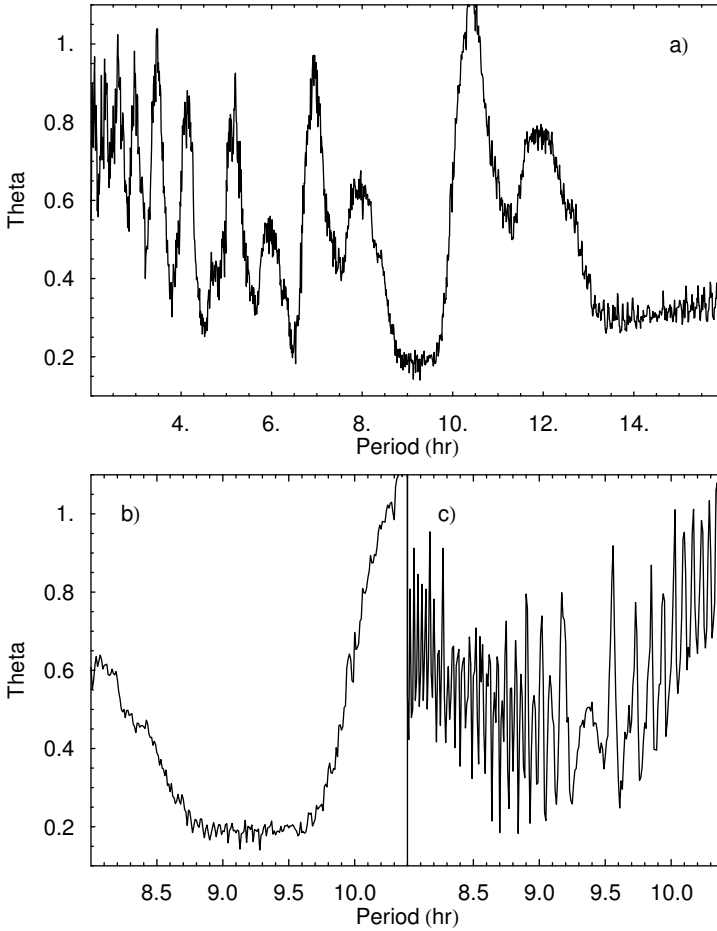


Figure 4.3 – Periodogram for the data of 1998 SN₁₆₅. The lower left panel (b) shows an enlarged section near the minimum calculated using only the data published in this paper, and the lower right panel (c) shows the same region recalculated after adding the PDR02 data.

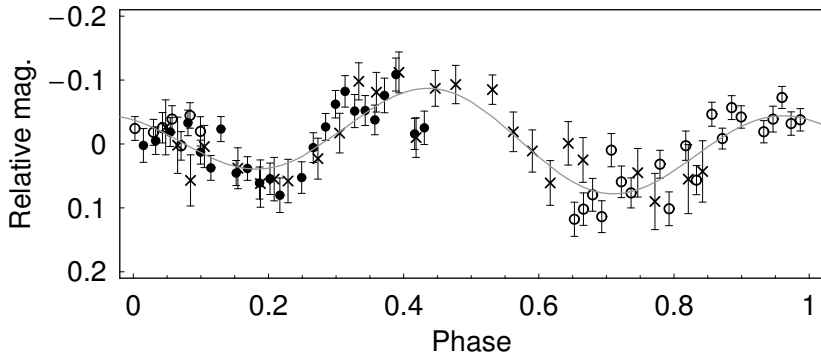


Figure 4.4 – Lightcurve of 1998 SN₁₆₅. The figure represents the data phased with the best fit period $P = 8.84$ hr. Different symbols correspond to different nights of observation. The gray line is a 2nd order Fourier series fit to the data. The PDR02 data are shown as crosses.

4.4.3 2001 CZ₃₁

This object shows substantial brightness variations (4.5σ above the comparison stars) in a systematic manner. The first night of data seems to sample nearly one complete rotational phase. As for 1998 SN₁₆₅, the 2001 CZ₃₁ data span only two nights of observations. In this case, however, the PDM minima (see Figs. 4.7a and 4.7b) are very narrow and only two correspond to independent periods, $P = 4.69$ hr (the minimum at 5.82 is a 24 hr alias of 4.69 hr), and $P = 5.23$ hr.

2001 CZ₃₁ has also been observed by Sheppard & Jewitt (2002, hereafter SJ02) in February and April 2001, with inconclusive results. We used their data to try to rule out one (or both) of the two periods we found. We subtracted the SJ02 mean magnitudes in order to combine it with our uncalibrated observations. Figure 4.7c shows the section of the periodogram around $P = 5$ hr, recalculated using SJ02’s first night plus our own data. The aliases are due to the 1 month time difference between the two observing runs. The new PDM minimum is at $P = 4.71$ hr—very close to the $P = 4.69$ hr determined from our data alone.

Visual inspection of the combined data set phased with $P = 4.71$ hr shows a very good match between SJ02’s first night (2001 Feb 20) and our own data (see Fig. 4.8). SJ02’s second and third nights show very large scatter and were not included in our analysis. Phasing the data with $P = 5.23$ hr yields a more scattered lightcurve, which confirms the PDM result. We will use $P = 4.71$ hr throughout the rest of the paper.

We measured a lightcurve amplitude of $\Delta m = 0.21 \pm 0.02$ mag. If we use both ours and SJ02’s first night data, Δm rises to 0.22 mag.

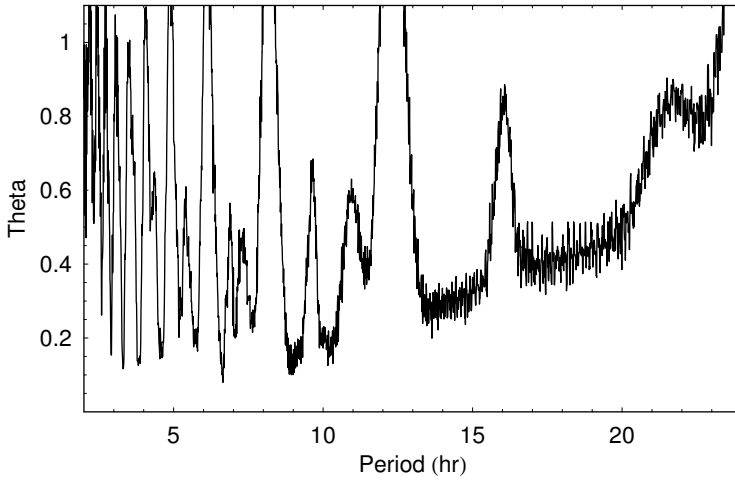


Figure 4.5 – Periodogram for the 1999 DF₉ data. The minimum corresponds to a lightcurve period $P = 6.65$ hr.

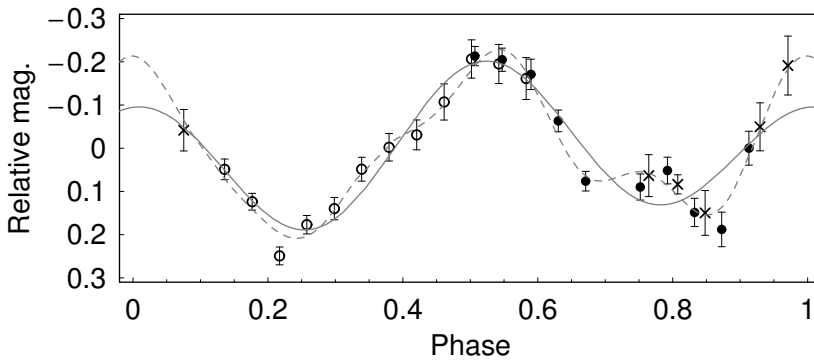


Figure 4.6 – Same as Figure 4.4 for KBO 1999 DF₉. The best fit period is $P = 6.65$ hr. The lines represent a 2nd order (solid line) and 5th (dashed line) order Fourier series fits to the data. Normalized χ^2 values of the fits are 2.8 and 1.3 respectively.

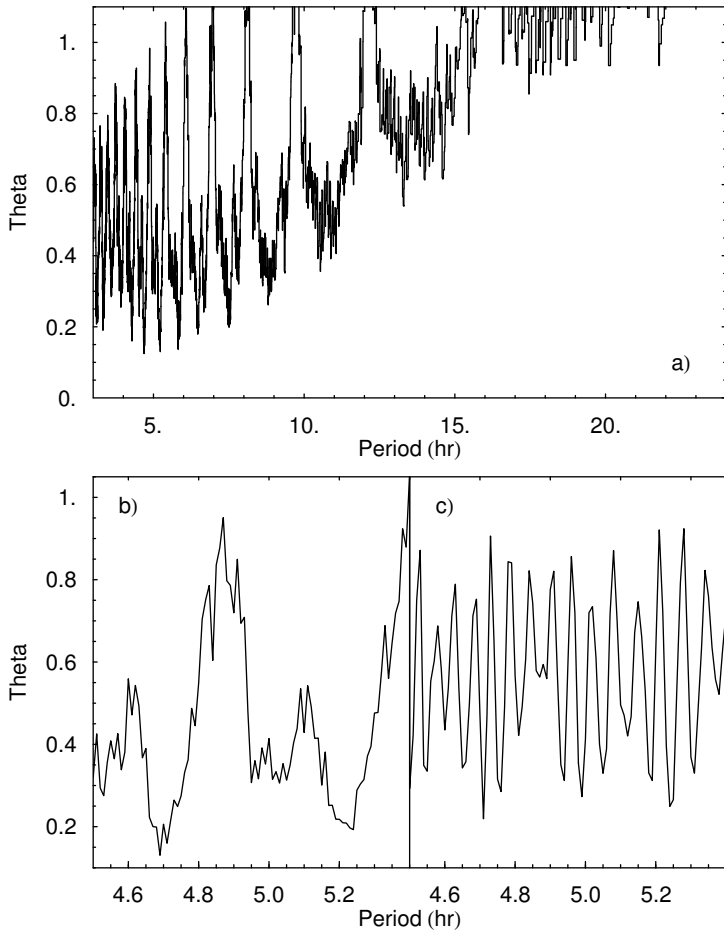


Figure 4.7 – Periodogram for the 2001 CZ₃₁ data. The lower left panel (b) shows an enlarged section near the minimum calculated using only the data published in this paper, and the lower right panel (c) shows the same region recalculated after adding the SJ02 data.

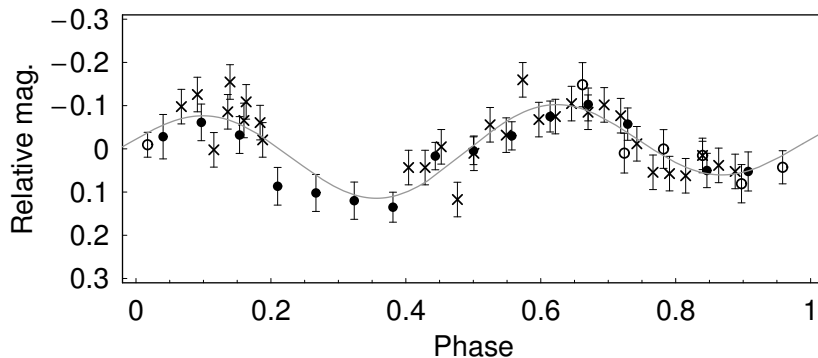


Figure 4.8 – Same as Figure 4.4 for KBO 2001 CZ₃₁. The data are phased with period $P = 4.71$ hr. The points represented by crosses are taken from SJ02.

4.4.4 Flat Lightcurves

The fluctuations detected in the optical data of KBOs 1996 TO₆₆, 1996 TS₆₆, 1999 TC₃₆, 1999 RZ₂₅₃, 2000 CM₁₀₅, and Huya, are well within the uncertainties. Chaos shows some variations with respect to the comparison stars but no period was found to fit all the data. See Table 4.7 and Fig. 4.9 for a summary of the results.

4.4.5 Other lightcurve measurements

The KBO lightcurve database has increased considerably in the last few years, largely due to the observational campaign of SJ02, with a recent updates in Sheppard & Jewitt (2003, hereafter SJ03) and Sheppard & Jewitt (2004). These authors have published observations and rotational data for a total of 30 KBOs (their SJ02 paper includes data for 3 other previously published lightcurves in the analysis). Other recently published KBO lightcurves include those for (50000) Quaoar (Ortiz et al. 2003) and the scattered KBO (29981) 1999 TD₁₀ (Rousselot et al. 2003). Of the 10 KBO lightcurves presented in this paper, 6 are new to the database, bringing the total to 41.

Table 4.8 lists the rotational data of the 41 KBOs that will be analyzed in the rest of the paper.

4.5 Analysis

In this section we examine the lightcurve properties of KBOs and compare them with those of main-belt asteroids (MBAs). The lightcurve data for these two families of objects cover different size ranges. MBAs, being closer to Earth, can be observed down to much smaller sizes than KBOs; in general it is very

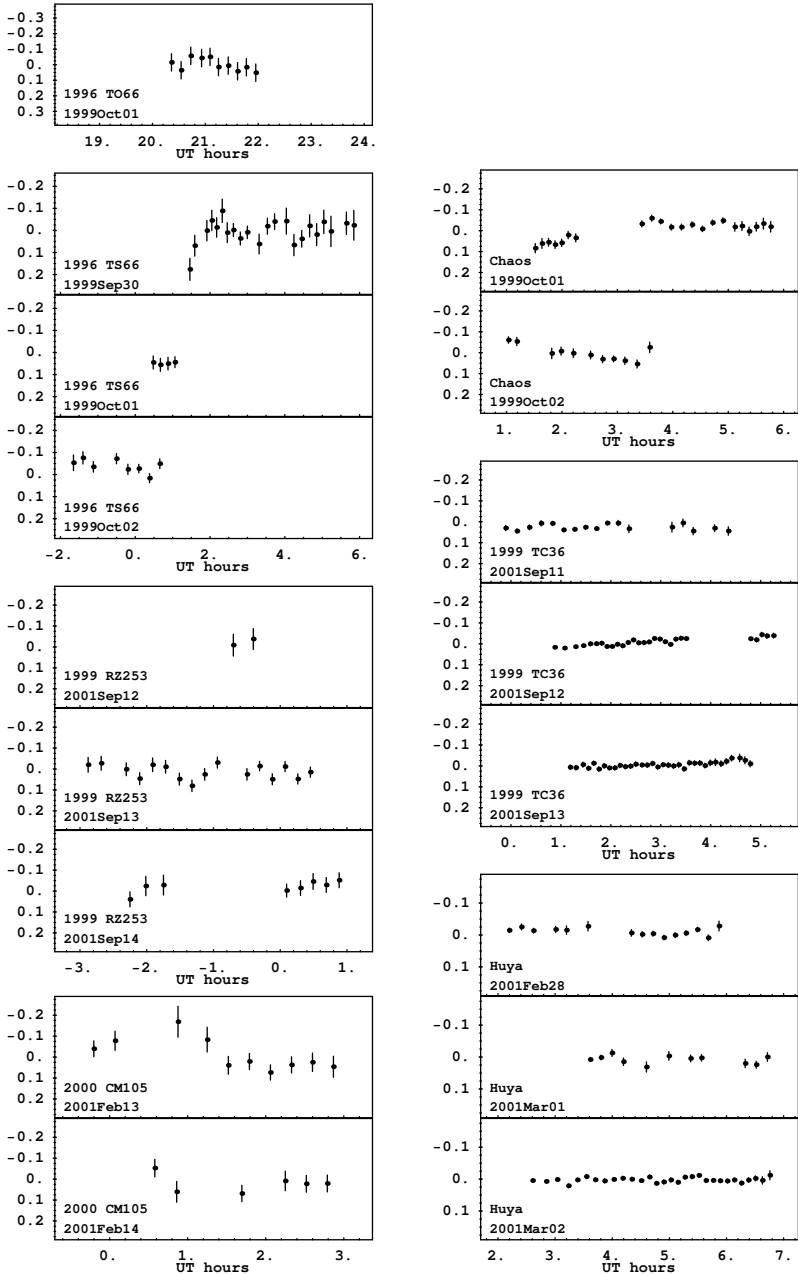


Figure 4.9 – The “flat” lightcurves are shown. The respective amplitudes are within the photometric uncertainties.

Table 4.8 – Database of KBOs Lightcurve Properties.

Object	Designation	Class ^a	Size ^b [km]	Period ^c [hr]	Δm_R ^d [mag]	Source ^e
KBOs considered to have $\Delta m < 0.15$ mag						
15789	1993 SC	P	240		0.04	RT99, DMcG97
15820	1994 TB	P	220		<0.04	SJ02
	1996 GQ ₂₁	S	730		<0.10	SJ02
	1996 TL ₆₆	S	480		0.06	RT99, LJ98
15875	1996 TP ₆₆	P	250		0.12	RT99, CB99
	1997 CS ₂₉	C	630		<0.08	SJ02
	1998 HK ₁₅₁	P	170		<0.15	SJ02
33340	1998 VG ₄₄	P	280		<0.10	SJ02
19521	Chaos	C	600		<0.10	LL, SJ02
	1999 DE ₉	S	700		<0.10	SJ02
47171	1999 TC ₃₆	Pb	600		<0.07	LL, SJ03
38628	Huya	P	740		<0.04	LL, SJ03
	2000 YW ₁₃₄	S	790		<0.10	SJ03
	2001 FP ₁₈₅	S	400		<0.10	SJ03
	2001 FZ ₁₇₃	S	430		<0.06	SJ02
	2001 KD ₇₇	P	430		<0.10	SJ03
28978	Ixion	P	1310		<0.10	SJ03, O01
	2001 QF ₂₉₈	P	580		<0.10	SJ03
42301	2001 UR ₁₆₃	S	1020		<0.10	SJ03
42355	2002 CR ₄₆	S	210		<0.10	SJ03
55636	2002 TX ₃₀₀	C	1250	16.24	0.08±0.02	SJ03
55637	2002 UX ₂₅	C	1090		<0.10	SJ03
55638	2002 VE ₉₅	P	500		<0.10	SJ03
	2000 CM ₁₀₅	C	330		<0.14	LL
	1999 RZ ₂₅₃	Cb	380		<0.05	LL
	1996 TS ₆₆	C	300		<0.14	LL
KBOs considered to have $\Delta m \geq 0.15$ mag						
32929	1995 QY ₉	P	180	7.3	0.60±0.04	SJ02, RT99
24835	1995 SM ₅₅	C	630	8.08	0.19±0.05	SJ03
19308	1996 TO ₆₆	C	720	7.9	0.26±0.03	SJ03, H00
26308	1998 SM ₁₆₅	R	400	7.1	0.45±0.03	SJ02, R01
33128	1998 BU ₄₈	S	210	9.8	0.68±0.04	SJ02, R01
40314	1999 KR ₁₆	C	400	11.858	0.18±0.04	SJ02
47932	2000 GN ₁₇₁	P	360	8.329	0.61±0.03	SJ02
20000	Varuna	C	980	6.34	0.42±0.03	SJ02
	2003 AZ ₈₄	P	900	13.44	0.14±0.03	SJ03
	2001 QG ₂₉₈	Pcb	240	13.7744	1.14±0.04	SJ04
50000	Quaoar	C	1300	17.6788	0.17±0.02	O03
29981	1999 TD ₁₀	S	100	15.3833	0.53±0.03	Rou03
35671	1998 SN ₁₆₅	C	400	8.84	0.16±0.01	LL
	1999 DF ₉	C	340	6.65	0.40±0.02	LL
	2001 CZ ₃₁	C	440	4.71	0.21±0.06	LL

^aDynamical class (C = classical KBO, P = Plutino, b = binary KBO).

^bDiameter in km assuming an albedo of 0.04, except for (20000) Varuna which has a known albedo of 0.07.

^cPeriod of the lightcurve in hours. For KBOs with both single and double peaked possible lightcurves the double peaked period is listed.

^dLightcurve amplitude in magnitudes.

^eDMcG97 = Davies et al. (1997), CB99 = Collander-Brown et al. (1999), H00 = Hainaut et al. (2000), LJ98 = Luu & Jewitt (1998), O01 = Ortiz et al. (2001), O03 = Ortiz et al. (2003), RT99 = Romanishin & Tegler (1999), R01 = Romanishin et al. (2001), Rou03 = Rousset et al. (2003), SJ02 = Sheppard & Jewitt (2002), SJ03 = Sheppard & Jewitt (2003), SJ04 = Sheppard & Jewitt (2004), LL = this work.

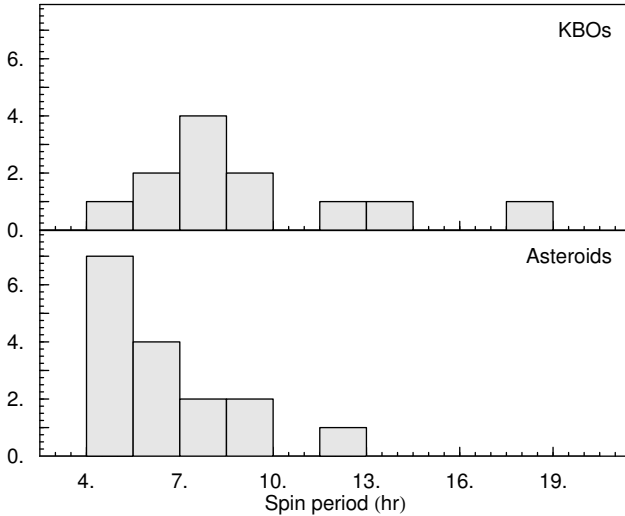


Figure 4.10 – Histograms of the spin periods of KBOs (upper panel) and main belt asteroids (lower panel) satisfying $D > 200$ km, $\Delta m \geq 0.15$ mag, $P < 20$ hr. The mean rotational periods of KBOs and MBAs are 9.23 hr and 6.48 hr, respectively. The y -axis in both cases indicates the number of objects in each range of spin periods.

difficult to obtain good quality lightcurves for KBOs with diameters $D < 50$ km. Furthermore, some KBOs surpass the 1000 km barrier—assuming a 0.04 albedo, 5 objects in the current database have diameters in excess of 1000 km—whereas the largest asteroid, Ceres, does not reach 900 km. This will be taken into account in the analysis.

The lightcurve data for asteroids was taken from the Harris Lightcurve Catalog², Version 5, while the diameter data were obtained from the Lowell Observatory database of asteroids orbital elements³. The sizes of KBOs were calculated from their absolute magnitude assuming an albedo of 0.04, except for Varuna for which simultaneous thermal and optical observations have yielded a red geometric albedo of $0.07^{+0.30}_{-0.17}$ (Jewitt et al. 2001).

4.5.1 Spin period statistics

As Fig. 4.10 shows, the spin period distributions of KBOs and MBAs are significantly different. Because the sample of KBOs of small size or large periods is poor, to avoid bias in our comparison we consider only KBOs and MBAs larger than 200 km and with periods below 20 hr. In this range the mean rotational periods of KBOs and MBAs are 9.23 hr and 6.48 hr, respectively, and the two are different with a 98.5% confidence according to Student's t -test. However, the different means do not rule that the underlying distributions are the same, and could simply mean that the two sets of data sample the same distribution differently. This is not the case, however, according to the Kolmogorov-Smirnov

²http://pdssbn.astro.umd.edu/sbnhtml/asteroids/colors_lc.html

³<ftp://ftp.lowell.edu/pub/elgb/astorb.html>

(K-S) test, which gives a probability that the periods of KBOs and MBAs are drawn from the same parent distribution of 0.7%.

Although it is clear that KBOs spin slower than asteroids, it is not clear why this is so. If collisions have contributed as significantly to the angular momentum of KBOs as they did for MBAs (Farinella et al. 1982; Catullo et al. 1984), then the observed difference should be related to how these two families react to collision events.

We will address the question of the collisional evolution of KBO spin rates in Chapter 5.

4.5.2 Lightcurve amplitudes and the shapes of KBOs

The cumulative distribution of KBO lightcurve amplitudes is shown in Fig. 4.11. It rises very steeply in the low amplitude range, and then becomes shallower reaching large amplitudes. In quantitative terms, $\sim 70\%$ of the KBOs possess $\Delta m < 0.15$ mag, while $\sim 12\%$ possess $\Delta m \geq 0.40$ mag, with the maximum value being $\Delta m = 0.68$ mag. [Note: Fig. 4.11 does not include the KBO 2001 QG₂₉₈ which has a lightcurve amplitude $\Delta m = 1.14 \pm 0.04$ mag, and would further extend the range of amplitudes. We do not include 2001 QG₂₉₈ in our analysis because it is thought to be a contact binary (Sheppard & Jewitt 2004)]. Figure 4.11 also compares the KBO distribution with that of MBAs. The distributions of the two populations are clearly distinct: in the low amplitude range ($\Delta m < 0.15$ mag) the KBO distribution is steeper than the MBA distribution and extends to larger values of Δm .

Figure 4.12 shows the lightcurve amplitude of KBOs and MBAs plotted against size. KBOs with diameters larger than $D = 400$ km seem to have lower lightcurve amplitudes than KBOs with diameters smaller than $D = 400$ km. Student's t -test confirms that the mean amplitudes in each of these two size ranges are different at the 98.5% confidence level. For MBAs the transition is less sharp and seems to occur at a smaller size ($D \sim 200$ km). In the case of asteroids, the accepted explanation is that small bodies ($D \lesssim 100$ km) are fragments of high-velocity impacts (Catullo et al. 1984), whereas their larger counterparts ($D > 200$ km) are not. The lightcurve data of small KBOs are still too sparse to permit a similar analysis.

The distribution of lightcurve amplitudes can be used to infer the shapes of KBOs, if certain reasonable assumptions are made (see, e.g., LL03a). Generally, objects with elongated shapes produce large brightness variations due to their changing projected cross-section as they rotate. Conversely, round objects, or those with the spin axis aligned with the line of sight, produce little or no brightness variations, resulting in "flat" lightcurves. Figure 4.12 shows that the lightcurve amplitudes of KBOs with diameters smaller and larger than $D = 400$ km are significantly different. Does this mean that the shapes of KBOs

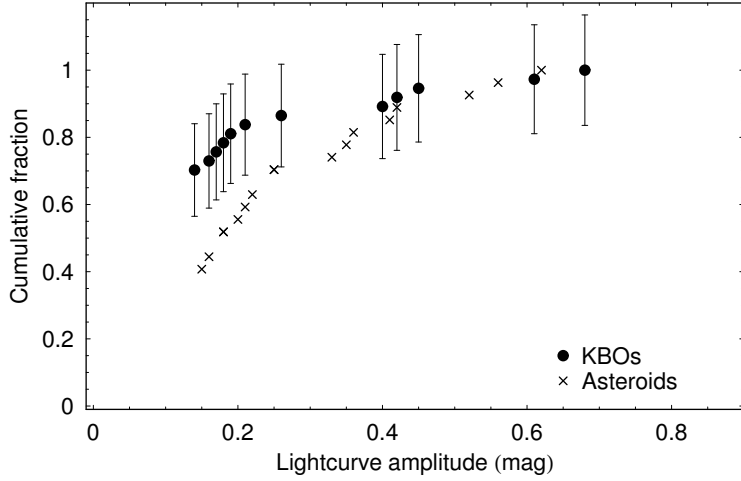


Figure 4.11 – Cumulative distribution of lightcurve amplitude for KBOs (circles) and asteroids (crosses) larger than 200 km. We plot only KBOs for which a period has been determined. KBO 2001 *QG*₂₉₈, thought to be a contact binary (Sheppard & Jewitt 2004), is not plotted although it may be considered an extreme case of elongation.

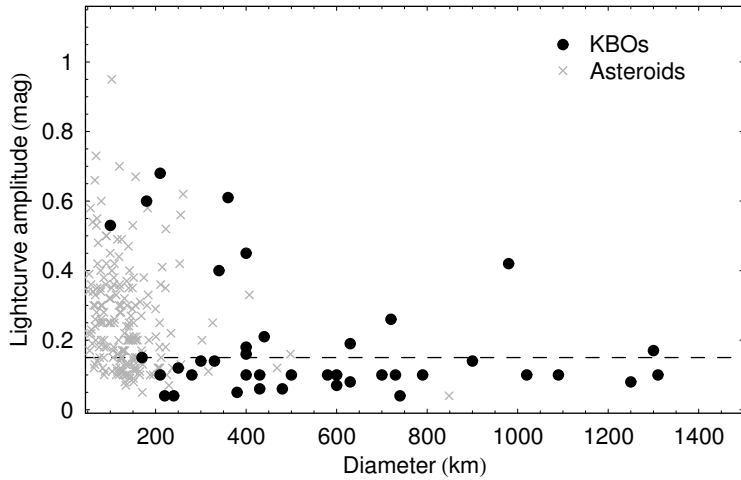


Figure 4.12 – Lightcurve amplitudes of KBOs (black circles) and main belt asteroids (gray crosses) plotted against object size. All sizes assume albedo of 0.04 except for Varuna, which has a known albedo of 0.07.

are also different in these two size ranges? To investigate this possibility of a size dependence among KBO shapes we will consider KBOs with diameter smaller and larger than 400 km separately. We shall loosely refer to objects with diameter $D > 400$ km and $D \leq 400$ km as *larger* and *smaller* KBOs, respectively.

We approximate the shapes of KBOs by triaxial ellipsoids with semi-axes $a > b > c$. For simplicity we consider the case where $b = c$ and use the axis ratio $\tilde{a} = a/b$ to characterize the shape of an object. The orientation of the spin axis is parameterized by the aspect angle θ , defined as the smallest angular distance between the line of sight and the spin vector. On this basis the lightcurve amplitude Δm is related to \tilde{a} and θ via the relation (Eqn. 2.2 with $\bar{c} = 1$)

$$\Delta m = 2.5 \log \sqrt{\frac{2\tilde{a}^2}{1 + \tilde{a}^2 + (\tilde{a}^2 - 1) \cos(2\theta)}}. \quad (4.1)$$

Following LL03b we model the shape distribution by a power-law of the form

$$f(\tilde{a}) d\tilde{a} \propto \tilde{a}^{-q} d\tilde{a} \quad (4.2)$$

where $f(\tilde{a}) d\tilde{a}$ represents the fraction of objects with shapes between \tilde{a} and $\tilde{a} + d\tilde{a}$. We use the measured lightcurve amplitudes to estimate the value of q by employing both the method described in LL03a, and by Monte Carlo fitting the observed amplitude distribution (SJ02; LL03b). The latter consists of generating artificial distributions of Δm (Eqn. 4.1) with values of \tilde{a} drawn from distributions characterized by different q 's (Eqn. 4.2), and selecting the one that best fits the observed cumulative amplitude distribution (Fig. 4.11). The values of θ are generated assuming random spin axis orientations. We use the K-S test to compare the different fits. The errors are derived by bootstrap resampling the original data set (Efron 1979), and measuring the dispersion in the distribution of best-fit power-law indexes, q_i , found for each bootstrap replication.

Following the LL03a method we calculate the probability of finding a KBO with $\Delta m \geq 0.15$ mag:

$$p(\Delta m \geq 0.15) \approx \int_{\sqrt{K}}^{\tilde{a}_{\max}} f(\tilde{a}) \sqrt{\frac{\tilde{a}^2 - K}{(\tilde{a}^2 - 1)K}} d\tilde{a}. \quad (4.3)$$

where $K = 10^{0.8 \times 0.15}$, $f(\tilde{a}) = C \tilde{a}^{-q}$, and C is a normalization constant. This probability is calculated for a range of q 's to determine the one that best matches the observed fraction of lightcurves with amplitude larger than 0.15 mag. These fractions are $f(\Delta m \geq 0.15 \text{ mag}; D \leq 400 \text{ km}) = 8/18$, and $f(\Delta m \geq 0.15 \text{ mag}; D > 400 \text{ km}) = 6/22$, and $f(\Delta m \geq 0.15 \text{ mag}) = 14/40$ for the complete set of data. The results are summarized in Table 4.9 and shown in Fig. 4.13.

Both methods yield steeper shape distributions for larger KBOs, implying more spherical shapes in this size range (Table 4.9). A distribution with $q = 9.8$

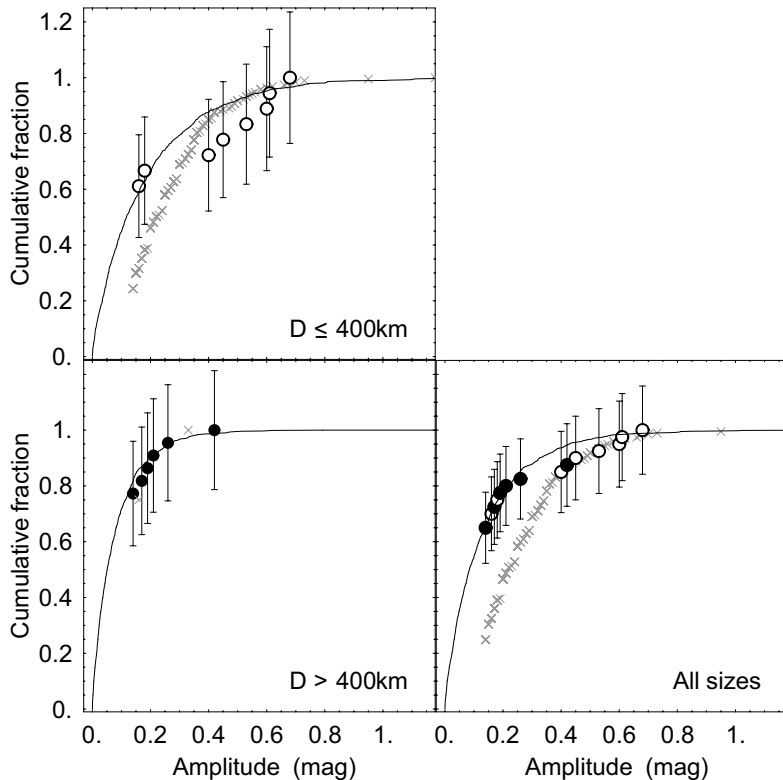


Figure 4.13 – Observed cumulative lightcurve amplitude distributions of KBOs (black circles) with diameter smaller than 400 km (upper left panel), larger than 400 km (lower left panel), and of all the sample (lower right panel) are shown as black circles. Error bars are poissonian. The best fit power-law shape distributions of the form $f(\bar{a}) d\bar{a} = \bar{a}^{-q} d\bar{a}$ were converted to amplitude distributions using a Monte Carlo technique (see text for details), and are shown as solid lines. The best fit q 's are listed in Table 4.9. The gray crosses show the distributions for asteroids in the same size ranges.

Size range	Method	
	LL03	MC
$D \leq 400$ km	$q = 4.0^{+2.0}_{-1.5}$	$q = 4.5 \pm 2.3$
$D > 400$ km	$q = 6.7^{+2.7}_{-2.1}$	$q = 9.8 \pm 2.6$
All sizes	$q = 5.8^{+1.4}_{-1.3}$	$q = 6.1 \pm 1.7$

Table 4.9 – Best fit parameter to the KBO shape distribution. Column 1 is the range of KBO diameters, in km, considered in each case. Columns 2 and 3 are the results from the method described in LL03, and from a Monte Carlo fit of the lightcurve amplitude distribution, respectively. See text for detailed discussion.

predicts that $\sim 80\%$ of the large KBOs have $a/b < 1.2$. For the smaller objects we find a shallower distribution, $q \sim 4 - 4.5$, which implies a significant fraction of very elongated objects: $\sim 15\%$ have $a/b > 1.7$. Although based on small

numbers, the shape distribution of large KBOs is well fit by a simple power-law (the K-S rejection probability is 0.3%). This is not the case for smaller KBOs for which the fit is poorer (K-S rejection probability is 61%, see Fig. 4.13). Our results are in agreement with previous studies of the overall KBO shape distribution, which had already shown that a simple power-law does not explain the shapes of KBOs as a whole (LL03b; SJ02).

The results presented in this section suggest that the shape distributions of smaller and larger KBOs are different. However, given the size of our sample, we cannot conclusively state that this difference is significant. Better observational constraints, particularly of smaller KBOs, are necessary to understand the origin of the KBO shape distribution. A comparison with asteroids suggests that the collisional evolution may have played an important role. Collisions in the asteroid belt have left different marks in smaller and larger bodies. The shapes of smaller asteroids ($D \leq 100$ km) are consistent with collisional fragments (Catullo et al. 1984), indicating that they are most likely by-products of disruptive collisions. Larger asteroids have in principle survived collisional destruction for the age of the solar system, but may nonetheless have been converted to rubble piles by repeated impacts. As a result of multiple collisions, the “loose” pieces of the larger asteroids may have reassembled into shapes close to triaxial equilibrium ellipsoids (Farinella et al. 1981).

4.5.3 The inner structure of KBOs

In this section we wish to investigate if the rotational properties of KBOs show any evidence that they have a rubble pile structure; a possible dependence on object size is also investigated.

Figure 4.14 plots the lightcurve amplitudes versus spin periods for the 15 KBOs whose lightcurve amplitudes and spin period are known. Open and filled symbols indicate the KBOs with diameter smaller and larger than $D = 400$ km, respectively. Clearly, the smaller and larger KBOs occupy different regions of the diagram. For the larger KBOs (black filled circles) the (small) lightcurve amplitudes are almost independent of the objects’ spin periods. In contrast, smaller KBOs span a much broader range of lightcurve amplitudes. Two object objects have very low amplitudes: 1998 SN₁₆₅ and 1999 KR₁₆, which have diameters $D \sim 400$ km and fall precisely on the boundary of the two size ranges. The remaining objects hint at a trend of increasing Δm with lower spin rates. The one exception is 1999 TD₁₀, a Scattered Disk Object ($e = 0.872$, $a = 95.703$ AU) that spends most of its orbit in rather empty regions of space and most likely has a different collisional history.

For comparison, Fig. 4.14 also shows results of N-body simulations of collisions between “ideal” rubble piles (gray filled circles; Leinhardt et al. 2000), and the lightcurve amplitude-spin period relation predicted by ellipsoidal figures of

hydrostatic equilibrium (dashed and dotted lines; Chandrasekhar 1969; Holsapple 2001). The latter is calculated from the equilibrium shapes that rotating uniform fluid bodies assume by balancing gravitational and centrifugal acceleration. The spin rate-shape relation in the case of uniform fluids depends solely on the density of the body. Although fluid bodies behave in many respects differently from rubble piles, they may, as an extreme case, provide insight on the equilibrium shapes of gravitationally bound agglomerates.

The simulations of Leinhardt et al. (2000, hereafter LRQ2000) consist of collisions between agglomerates of small spheres meant to simulate collisions between rubble piles. Each agglomerate consists of ~ 1000 spheres, held together by their mutual gravity, and has no initial spin. The spheres are indestructible, have no sliding friction, and have coefficients of restitution of ~ 0.8 . The bulk density of the agglomerates is 2000 kg m^{-3} . The authors collide two equal-size rubble piles for a range of impact velocities and impact parameters. The impact velocities range from \sim zero at infinity to a few times the critical velocity for which the impact energy would exceed the mutual gravitational binding energy of the two rubble piles. The impact geometries range from head-on collisions to grazing impacts. The mass, final spin period, and shape of the *largest remnant* resulting from each collision are registered and presented (see Table 1 of LRQ2000). From their results, we selected the outcomes for which the mass of the largest remnant is equal or larger than the mass of one of the colliding rubble piles, i.e., we selected only accreting outcomes. The spin periods and lightcurve amplitudes that would be generated by such remnants (assuming they are observed equator-on) are plotted in Fig. 4.14 as gray circles. Nine points, resulting from head-on collisions, are not visible because the periods are larger than 19 hr, up to ~ 650 hr. Note that the simulated rubble piles have radii of 1 km—much smaller than the sizes of the KBOs in our database. However, since the effects of the collision scale with the ratio of impact energy to gravitational binding energy of the colliding bodies (Benz & Asphaug 1999), the model results should apply to other sizes. Clearly, the LRQ2000 model makes several specific assumptions, and represents one possible idealization of what is usually referred to as “rubble pile”. Nevertheless, the results are illustrative of how collisions may affect this type of structures, and are useful for comparison with the KBO data.

The lightcurve amplitudes resulting from the LRQ2000 experiment are relatively small ($\Delta m < 0.25$ mag) for spin periods larger than $P \sim 5.5$ hr (see Fig. 4.14). Objects spinning faster than $P = 5.5$ hr have more elongated shapes, resulting in larger lightcurve amplitudes, up to 0.65 magnitudes. The latter are the result of collisions with higher angular momentum transfer than the former (see Table 1 of LRQ2000). The maximum spin rate attained by the rubble piles, as a result of the collision, is ~ 4.5 hr. This is consistent with the maximum spin expected for bodies in hydrostatic equilibrium with the same density as the rubble piles ($\rho = 2000 \text{ kg m}^{-3}$; see long-dashed line in Fig. 4.14). The results of LRQ2000 show that collisions between ideal rubble piles can produce elongated

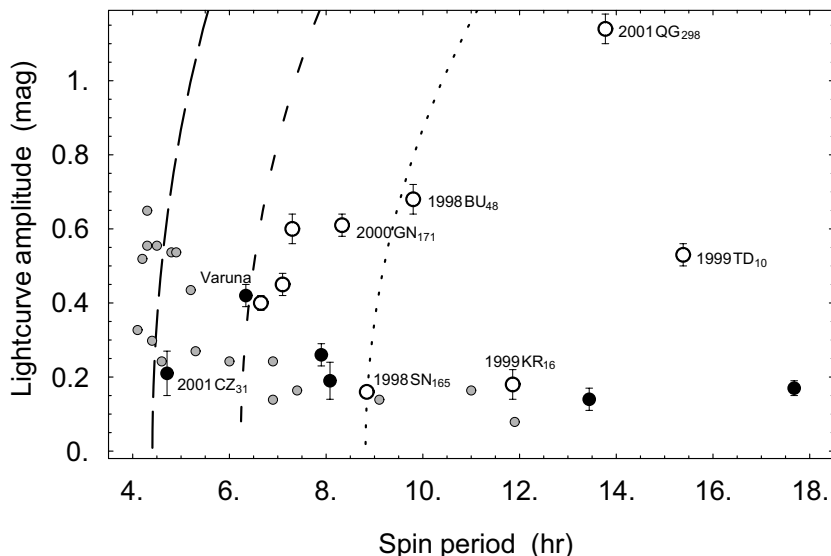


Figure 4.14 – Lightcurve amplitudes versus spin periods of KBOs. The black filled and open circles represent objects larger and smaller than 400 km, respectively. The smaller gray circles show the results of numerical simulations of “rubble-pile” collisions (Leinhardt et al. 2000). The lines represent the locus of rotating ellipsoidal figures of hydrostatic equilibrium with densities $\rho = 500 \text{ kg m}^{-3}$ (dotted line), $\rho = 1000 \text{ kg m}^{-3}$ (shorter dashes) and $\rho = 2000 \text{ kg m}^{-3}$ (longer dashes). The point towards the upper right corner of the plot corresponds to 2001 QG₂₉₈ ($P = 13.77 \text{ hr}$, $\Delta m = 1.14 \text{ mag}$), a likely contact binary KBO (Sheppard & Jewitt 2004).

remnants (when the projectile brings significant angular momentum into the target), and that the spin rates of the collisional remnants do not extend much beyond the maximum spin permitted to fluid uniform bodies with the same bulk density.

The distribution of KBOs in Fig. 4.14 is less clear. Indirect estimates of KBO bulk densities indicate values $\rho \sim 1000 \text{ kg m}^{-3}$ (Luu & Jewitt 2002). If KBOs are strengthless rubble piles with such low densities we would not expect to find objects with spin periods lower than $P \sim 6 \text{ hr}$ (as indicated by the dashed line in Fig. 4.14). However, one object (2001 CZ₃₁), is found to have a spin period below 5 hr. If this object has a rubble pile structure, its density must be at least $\sim 2000 \text{ kg m}^{-3}$ (see Fig. 4.14). The remaining 14 objects have spin periods below the expected upper limit, given their estimated density. Of the 14, 4 objects lie close to the line corresponding to equilibrium ellipsoids of density $\rho = 1000 \text{ kg m}^{-3}$. One of these objects, (2000) Varuna, has been studied in detail by Sheppard & Jewitt (2002). The authors conclude that Varuna is best interpreted as a rotationally deformed rubble pile with $\rho \leq 1000 \text{ kg m}^{-3}$. One object, 2001 QG₂₉₈, has an exceptionally large lightcurve amplitude ($\Delta m = 1.14 \text{ mag}$), indicative of a very elongated shape (axes ratio $a/b > 2.85$). Given

its modest spin rate ($P = 13.8$ hr) and approximate size ($D \sim 240$ km) it is unlikely that it would be able to keep such an elongated shape against the crush of gravity. Analysis of the lightcurve of this object (Sheppard & Jewitt 2004) suggests it is a contact (or very close) binary KBO. The same applies to two other KBOs, 2000 GN₁₇₁ and (33128) 1998 BU₄₈, also very likely to be contact binaries.

To summarize, based on the available rotational properties of KBOs, it is not clear if they have a rubble pile structure. Comparing the KBO data with results from computer simulations of rubble pile collisions (LRQ2000) we find that 11 out of 15 ($\sim 73\%$) KBOs have rotational data that follows essentially the same trends as the LRQ2000 results. Of the 11 KBOs, 5 (45%) have diameters $D \leq 400$ km, and 6 (55%) have diameters $D > 400$ km. If these KBOs are rubble piles then their spin rates set a lower limit to their bulk density: one object (2001 CZ₃₁) spins fast enough that its density must be at least $\rho \sim 2000$ kg m⁻³, while 4 other KBOs (including (20000) Varuna) must have densities larger than $\rho \sim 1000$ kg m⁻³. A better assessment of the inner structure of KBOs will require more observations, and detailed modelling of the collisional evolution of rubble-piles.

4.6 Conclusions

We have collected and analyzed R-band photometric data for 10 Kuiper Belt objects, 5 of which have not been studied before. No significant brightness variations were detected from KBOs 2000 CM₁₀₅, 1999 RZ₂₅₃, 1996 TS₆₆. Previously observed KBOs Chaos, 1999 TC₃₆, and Huya were confirmed to have very low amplitude lightcurves ($\Delta m \leq 0.1$ mag). 1998 SN₁₆₅, 1999 DF₉, and 2001 CZ₃₁ were shown to have periodic brightness variations. Our lightcurve amplitude statistics are thus: 3 out of 10 (30%) observed KBOs have $\Delta m \geq 0.15$ mag, and 1 out of 10 (10%) has $\Delta m \geq 0.40$ mag. This is consistent with previously published results.

The rotational properties that we obtained were combined with existing data in the literature and the total data set was used to investigate the distribution of spin period and shapes of KBOs. Our conclusions can be summarized as follows:

1. KBOs with diameters $D > 200$ km have a mean spin period of 9.23 hr, and thus rotate slower on average than main belt asteroids of similar size ($\langle P \rangle_{\text{MBAs}} = 6.48$ hr). The probability that the two distributions are drawn from the same parent distribution is 0.7%.
2. 26 of 37 KBOs (70%, $D > 200$ km) have lightcurve amplitudes below 0.15 mag. In the asteroid belt only 10 of the 27 (37%) asteroids in the same size range have such low amplitude lightcurves.
3. KBOs with diameters $D > 400$ km have lightcurves with significantly

- (98.5% confidence) smaller amplitudes ($\langle \Delta m \rangle = 0.13$ mag, $D > 400$ km) than KBOs with diameters $D \leq 400$ km ($\langle \Delta m \rangle = 0.26$ mag, $D \leq 400$ km).
4. The shape distributions are different for these two size ranges, and predict a larger fraction of round objects in the $D > 400$ km size range ($f(a/b > 1.2) \sim 80\%$) than in the group of smaller objects ($f(a/b > 1.2) \sim 50\%$).
 5. The rotational properties of KBOs suggest that some of these objects may have a rubble pile structure: 73% of KBOs with measured spin periods have lightcurve amplitudes and spin periods consistent with rubble piles of density $\rho \gtrsim 1000 \text{ kg m}^{-3}$. However, the data are too sparse to allow a conclusive assessment of the inner structure of KBOs.
 6. KBO 2001 CZ₃₁ has a spin period of $P = 4.71$ hr. If this object has a rubble pile structure then its density must be $\rho \gtrsim 2000 \text{ kg m}^{-3}$. If the object has a lower density then it must have internal strength.

Acknowledgments

This work was supported by grants from the Netherlands Foundation for Research (NWO), and the Leids Kerkhoven-Bosscha Fonds (LKBF). We are grateful to Scott Kenyon and Ivo Labbé for helpful discussion.

References

- Benz, W. & Asphaug, E. 1999, *Icarus*, 142, 5
- Bernstein, G. M., Trilling, D. E., Allen, R. L., Brown, M. E., Holman, M., & Malhotra, R. 2004, *AJ*, 128, 1364
- Bertin, E. & Arnouts, S. 1996, *A&AS*, 117, 393
- Brown, R. H., Cruikshank, D. P., & Pendleton, Y. 1999, *ApJ*, 519, L101
- Catullo, V., Zappala, V., Farinella, P., & Paolicchi, P. 1984, *A&A*, 138, 464
- Chandrasekhar, S. 1969, *Ellipsoidal figures of equilibrium (The Silliman Foundation Lectures, New Haven: Yale University Press, 1969)*
- Collander-Brown, S. J., Fitzsimmons, A., Fletcher, E., Irwin, M. J., & Williams, I. P. 1999, *MNRAS*, 308, 588
- Davies, J. K., McBride, N., & Green, S. F. 1997, *Icarus*, 125, 61
- Dobrovolskis, A. R. & Burns, J. A. 1984, *Icarus*, 57, 464
- Doressoundiram, A., Peixinho, N., de Bergh, C., Fornasier, S., Thébault, P., Barucci, M. A., & Veillet, C. 2002, *AJ*, 124, 2279
- Efron, B. 1979, *Annals of Statistics*, 7, 1
- Farinella, P., Paolicchi, P., Tedesco, E. F., & Zappala, V. 1981, *Icarus*, 46, 114
- Farinella, P., Paolicchi, P., & Zappala, V. 1982, *Icarus*, 52, 409
- Goldreich, P., Lithwick, Y., & Sari, R. 2002, *Nature*, 420, 643
- Hainaut, O. R., Delahodde, C. E., Boehnhardt, H., Dotto, E., Barucci, M. A., Meech, K. J., Bauer, J. M., West, R. M., & Doressoundiram, A. 2000, *A&A*, 356, 1076
- Holsapple, K. A. 2001, *Icarus*, 154, 432
- Jewitt, D., Aussen, H., & Evans, A. 2001, *Nature*, 411, 446
- Jewitt, D. & Luu, J. 1993, *Nature*, 362, 730
- Jewitt, D. C. & Luu, J. X. 2000, *Protostars and Planets IV*, 1201
- 2001, *AJ*, 122, 2099
- Jewitt, D. C. & Sheppard, S. S. 2002, *AJ*, 123, 2110
- Lacerda, P. & Luu, J. 2003, *Icarus*, 161, 174
- Leinhardt, Z. M., Richardson, D. C., & Quinn, T. 2000, *Icarus*, 146, 133
- Luu, J. & Jewitt, D. 1996, *AJ*, 112, 2310
- Luu, J. X. & Jewitt, D. C. 2002, *ARA&A*, 40, 63
- Luu, J. & Lacerda, P. 2003, *Earth Moon and Planets*, 92, 221
- Luu, J. X. & Jewitt, D. C. 1998, *ApJ*, 494, L117+
- Noll, K. S., Stephens, D. C., Grundy, W. M., Millis, R. L., Spencer, J., Buie, M. W., Tegler, S. C., Romanishin, W., & Cruikshank, D. P. 2002, *AJ*, 124, 3424
- Ortiz, J. L., Gutiérrez, P. J., Sota, A., Casanova, V., & Teixeira, V. R. 2003, *A&A*, 409, L13
- Ortiz, J. L., Lopez-Moreno, J. J., Gutierrez, P. J., & Baumont, S. 2001, *Bulletin of the American Astronomical Society*, 33, 1047
- Peixinho, N., Doressoundiram, A., & Romon-Martin, J. 2002, *New Astronomy*, 7, 359
- Romanishin, W. & Tegler, S. C. 1999, *Nature*, 398, 129
- Romanishin, W., Tegler, S. C., Rettig, T. W., Consolmagno, G., & Botthof, B. 2001, *Bulletin of the American Astronomical Society*, 33, 1031
- Rousselot, P., Petit, J.-M., Poulet, F., Lacerda, P., & Ortiz, J. 2003, *A&A*, 407, 1139
- Sheppard, S. S. & Jewitt, D. C. 2002, *AJ*, 124, 1757
- 2003, *Earth Moon and Planets*, 92, 207
- Sheppard, S. S. & Jewitt, D. 2004, *AJ*, 127, 3023

- Stellingwerf, R. F. 1978, *ApJ*, 224, 953
Tegler, S. C. & Romanishin, W. 2000, *Nature*, 407, 979
Trujillo, C. A., Jewitt, D. C., & Luu, J. X. 2001a, *AJ*, 122, 457
Trujillo, C. A., Luu, J. X., Bosh, A. S., & Elliot, J. L. 2001b, *AJ*, 122, 2740
Trujillo, C. A. & Brown, M. E. 2002, *ApJ*, 566, L125
van Dokkum, P. G. 2001, *PASP*, 113, 1420
Weidenschilling, S. J. 2002, *Icarus*, 160, 212

Origin and evolution of KBO spins

ABSTRACT

We present a numerical study of the collisional evolution of the masses and spins of Kuiper Belt objects (KBOs). Our model follows one KBO at a time (the target), as it collides with the surrounding bodies. The collisional environment, described by the total mass, size and velocity distributions of KBOs, determines the total number, and the character of individual collisions. Changes in the target's spin rate and mass are calculated for each collision, as a function of a several of parameters describing individual objects and the environment. We find that the spins of KBOs do not depend strongly on their bulk properties. Furthermore, the observed spins of KBOs larger than ~ 200 km cannot be explained by collisions, if the objects had no spin at the end of the primary growth phase. This suggests that the large KBOs must have attained their spin rates very early in their evolution. We investigate the possibility that the accretion process was not entirely isotropic, and contributed angular momentum to the growing KBOs. We find that a $\sim 10\%$ asymmetry in the net angular momentum of accreted particles would explain the observations. However, if the accreted particles were comparable in size to the growing body, no anisotropy is required because the accretion of individual particles can produce significant spin changes. These two scenarios make different predictions about the distribution of KBO spin rates and spin axis orientations: (1) Anisotropic accretion favours low scatter in the spin rates; (2) Isotropic accretion of larger building blocks predicts a large scatter in KBO spin rates and random spin axis orientations. The existing data is insufficient to discern between the two possibilities.

Pedro Lacerda, Carsten Dominik, Jane Luu & Scott Kenyon
To be submitted to Icarus

5.1 Motivation

COLLISIONS are the cause for many of the observed properties of our solar system, and of solar system objects. The craters on the Moon (Proctor 1873; Wegener 1975), the inclination of planetary spin axes (Safronov 1969), the zodiacal light and the meteoritic flux (Whipple 1967), and the very origin of the Earth-Moon system (Cameron 1997), to cite a few examples, are all thought to be related to impact events.

The asteroid belt is an example of a system shaped by collisions. This is apparent, for example, from the asteroid spin rate distribution (Harris 1979; Farinella et al. 1981), and from the distribution of shapes of asteroids smaller than $r \sim 100$ km, which is consistent with that of fragments of high-velocity impact experiments carried out in the laboratory (Catullo et al. 1984).

Kuiper Belt objects (KBOs, Luu & Jewitt 2002) collide on timescales comparable to those of asteroids of the same size (Davis & Farinella 1997). Their physical and dynamical properties should therefore show signatures of such encounters. The importance of collisions to the distribution of spins and shapes of KBOs is not known. The lack of significant amounts of rotational data has discouraged investigation of the collisional evolution of KBO spins. However, several recent surveys (Sheppard & Jewitt 2002, 2003; Lacerda and Luu 2005, references therein) have provided the community with a database of lightcurves of 41 KBOs, from which 15 spin periods have been derived. Analysis of the amplitudes of these lightcurves (Luu & Lacerda 2003; Lacerda and Luu 2005) has revealed a broad variety of KBO shapes, from round to very elongated.

Probably the most striking example is (20000) Varuna (Jewitt & Sheppard 2002). Nearly 500 km in radius, and with an axis ratio $a/b \sim 1.5$, it completes one full rotation every 6.3 hours. The authors interpret this object's high spin angular momentum as the result of a collision. In the current low density Kuiper Belt the chance that (20000) Varuna could hit a body large enough to significantly alter its spin and shape is very low. This collision must have happened soon after the largest bodies formed.

KBOs grew by accretion of dust condensates. Numerical models yield a formation timescale of the largest KBOs of ~ 100 Myr (Kenyon & Luu 1999). The bulk of the population was essentially formed by that time. If accretion was isotropic, i.e., if the accreted material supplied zero average torque to the growing body, angular momentum conservation should lead to these objects having little spin by the end of the growth phase. This is very different from the what is observed today, where 10 of the 15 KBOs have spin periods below 10 hr.

In this paper we wish to investigate how collisions between Kuiper Belt objects may have changed their spin rates, in the last ~ 4 Gyr. Attempting to fit the observed distribution of KBO spins is not realistic at this point. The number of measured periods is small, and many aspects of KBOs are poorly understood.

Our goal is to explore the role of several parameters in the collisional evolution of KBO spins, and to gauge the overall importance of collisions in the KBO spin distribution.

5.2 Spin evolution model

We start by giving a general, qualitative explanation of how the model works, and below we describe in more detail what our assumptions are, and how individual steps are calculated.

5.2.1 General description

We want to investigate how collisions might contribute to the observed spins of KBOs. Our computation starts when the KBO population is already formed. We place the transition between the epoch of formation and the epoch of collisions at ≈ 4 Gyr ago. The particular value 4 Gyr is a safe order-of-magnitude estimate based on the best current models of KBO formation, which claim the population is essentially formed in $\lesssim 100$ Myr (Kenyon & Luu 1999). We assume, as a first order approximation, that the population of KBOs has a total mass and size distribution that do not change throughout the collisional evolution. This is clearly a simplified version of what happened since the Kuiper Belt has changed much over the last 4 Gyr. We adopt this simplification because we want to focus on the effects of collisions; the bulk properties of the Belt, such as the total mass, distribution of sizes, number of collisions, etc., are treated in a statistical, time-averaged way.

The KBO population is in Keplerian orbit around the Sun. For KBOs to collide, they must have random velocities relative to circular Keplerian orbits. Hereafter, when we refer to the velocities of the KBOs, we mean the random velocities in a Keplerian reference frame.

To simulate each collision, our model follows one individual KBO (the target) as it collides with other KBOs (the projectiles), for 4 Gyr time. The population of projectiles is binned according to size. By making assumptions about the total mass and the size distribution of the projectiles, we estimate how many projectiles fall in each size bin. Assuming KBOs to be spherical, with a given density, we can translate the size bins into mass bins. In general, and as a consequence of energy equipartition, which tries to make each object contribute a similar fraction to the total kinetic energy of the system, KBO velocities are a function of size: the smaller the mass, the higher the velocity.

First we calculate the total number of collisions experienced by the target KBO. These collisions occur with projectiles from different bins, so we need to determine how many collisions will come from a given bin. This depends on how many projectiles there are in the bin, as well as the size and velocity of

these projectiles. Then we need to determine in what sequence the collisions will occur, i.e., which projectile from which bin collides with the target first, which collides second, and so on. This collisional sequence is randomly selected.

Once the collisional sequence is established we are ready to initiate the spin evolution. Starting with an initial size and spin rate for the target body, for each collision (in the predetermined sequence), we calculate the change in the target's spin rate and mass (size) resulting from the collision. In each collision a projectile hits the surface of the target at a random location, with a random orientation. Depending on the impact energy, the target may lose or gain mass. An important assumption in how we compute each collision is that all the angular momentum¹ transferred by the projectile to the target stays in the target, i.e., that the ejecta leaves the target body with no angular momentum. This assumption maximizes the spin rate change of the target per collision.

A catastrophic collision can have two possible outcomes: (1) the ejected mass may be equal to the total mass of projectile plus target or (2) the target may reach a critical spin rate where centrifugal acceleration is equal to the gravitational acceleration at the surface. If outcome 1 occurs the calculation stops. If outcome 2 occurs the calculation is not stopped—since an object can spin faster than the critical spin rate without flying apart, depending on its material properties—but the target is flagged. Since the exact critical spin is uncertain we choose to let the calculation continue and simply register the fact.

After all collisions have been accounted for and if the target still survives, we register the final spin and mass of the target, and can start the process all over again. By running the model several times with the same initial conditions, we obtain a Monte Carlo estimate of the distribution of spins that a particular set of initial set of parameters generates. Randomness is introduced in the collisional sequence and the individual collisional geometries.

5.2.2 Model Details

The input parameters of the model are listed in Table 5.1; these parameters are used by default, unless mentioned otherwise. The collisional environment is characterized by (1) the total mass in the projectiles, (2) the total volume accessible to all projectiles, (3) the size distribution of the projectiles, and (4) the velocity distribution of the projectiles. As a first order approximation we keep the total mass, and the size and velocity distributions constant throughout the ~ 4 Gyr of collisional evolution. The particular choice of 4 Gyr was made based on models of KBO accretion (Kenyon & Luu 1998, 1999) which estimate that Pluto-size objects finished forming by $\tau_P \approx 100$ Myr. By choosing a starting

¹The projectile's angular momentum has an orbital component and a spin component. Since the latter is much smaller than the former, we assume that the projectiles have no spin angular momentum.

Parameter	Symbol	Value
<i>General simulation and Belt parameters</i>		
Total mass in KBOs	M_{KBO}	$1 M_{\oplus}$
Distance Sun–Center of Kuiper Belt	a	40 AU
Width of Kuiper Belt	$2 \times \Delta a$	20 AU
Simulation timescale	Δt	4 Gyr
<i>Size distribution of KBOs</i>		
Number of size bins	N_b	64
Small body power-law exponent	q_S	2.5
Large body power-law exponent	q_L	3.5
Intermediate body power-law exponent	q_I	0.0
Small body size interval	$R_{\text{min}} \cdots R_1$	$10^0 \cdots 10^2$ m
Large body size interval	$R_2 \cdots R_{\text{max}}$	$10^{3.5} \cdots 10^6$ m
<i>Individual KBO bulk properties</i>		
Density	ρ	1000 kg m^{-3}
	Q_b	0
Disruption energy parameters	Q_g	$1.5 \times (10^5)^{1.25-\beta_g}$
	β_g	1.25

Table 5.1 – Model input parameters. These parameters are used by default, unless mentioned otherwise.

time $t_i = 5 \tau_P$, we place our model safely beyond the formation epoch. Kenyon & Bromley (2004a) have modelled the evolution of the size distribution of KBOs. Based on their estimate of the mass loss rate from the Kuiper Belt in the last ≈ 4 Gyr we assign a total mass of $1 M_{\oplus}$ to all KBOs, and use a set of power laws to parameterize the size distribution:

$$n(r) = \begin{cases} n_S r^{-q_S} & r \leq R_1, \\ n_I r^{-q_I} & R_1 < r \leq R_2, \\ n_L r^{-q_L} & r > R_2, \end{cases} \quad (5.1)$$

where $n(r) dr$ is the number of objects with radius between r and $r + dr$. The power law slopes are $q_S = 2.5$, $q_I = 0$, and $q_L = 3.5$, and break radii $R_1 = 10^2$ m and $R_2 = 10^{3.5}$ m.

The KBOs occupy a belt of width $2\Delta a = 20$ AU, whose center lies at a distance $a = 40$ AU from the Sun. The vertical extent of the belt is determined by the velocities of the projectiles and is specified below. The projectiles are binned according to their radius in N_b intervals whose centers form a geometric series defined as

$$\begin{aligned} r_0 &= R_{\text{max}}, \\ r_{i+1} &= (R_{\text{min}}/R_{\text{max}})^{1/N_b} r_i, \quad i = 1, \dots, N_b - 1 \end{aligned} \quad (5.2)$$

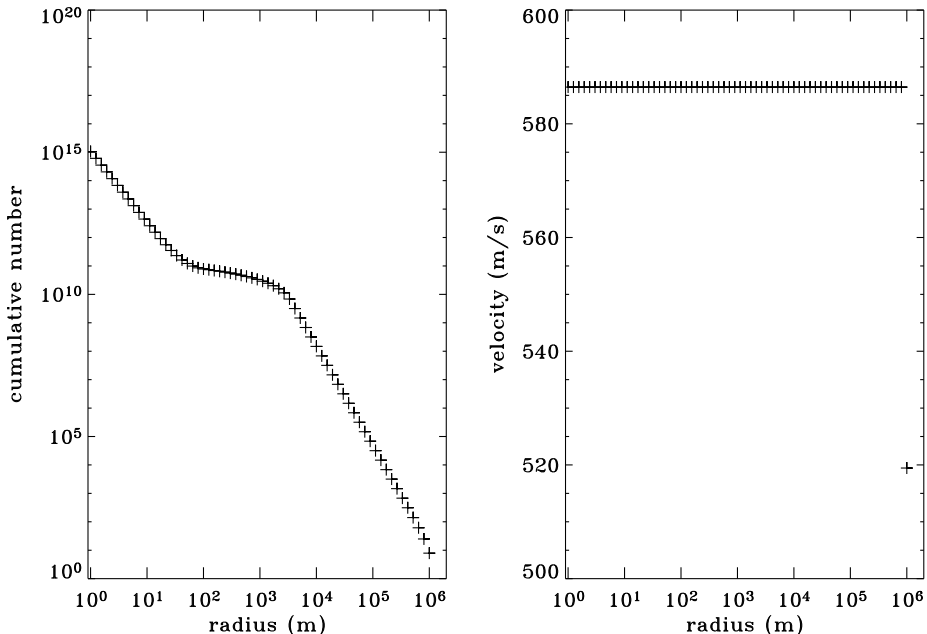


Figure 5.1 – The cumulative size distribution and the distribution of velocities for parameters, $M_{\text{KBO}} = 1 M_{\oplus}$, $q_S = 2.5$, $q_I = 0$, $q_L = 3.5$, break radii, $R_1 = 10^2$ m and $R_2 = 10^{3.5}$ m, and $\rho = 1000 \text{ kg m}^{-3}$.

where R_{min} and R_{max} are the minimum and maximum radius of the bodies. The number of objects in each bin, n_i , is determined from Eqn. (5.1).

We calculate the distribution of random velocities (measured relative to a reference frame in Keplerian rotation around the Sun) using the “two-group” approximation (Wetherill & Stewart 1989; Goldreich et al. 2004). This simplification considers the velocity evolution of only two groups of bodies, the small and the large, and provides an expression for the velocities of bodies of intermediate sizes. The approximation is in agreement with numerical simulations of the velocity evolution of a disk of planetesimals (Kenyon & Bromley 2004b). The velocity v of a body of radius r is then given by (Goldreich et al. 2004)

$$v(r) = \begin{cases} (\Sigma/\sigma)^{1/2} V_e & r < (\Sigma/\sigma)^{1/3} R_{\text{max}} \\ (\Sigma/\sigma)^{3/4} (r/R_{\text{max}})^{-3/4} V_e & \text{otherwise} \end{cases} \quad (5.3)$$

where Σ and σ are the surface mass densities of the large and small bodies, respectively, R_{max} is the radius of the large bodies, and V_e is the escape velocity from the surface of the large bodies.

The size and velocity distributions (Fig. 5.1), together with the total mass of the Belt, M_{KBO} , and the minimum and maximum radii of the bodies, R_{min} and

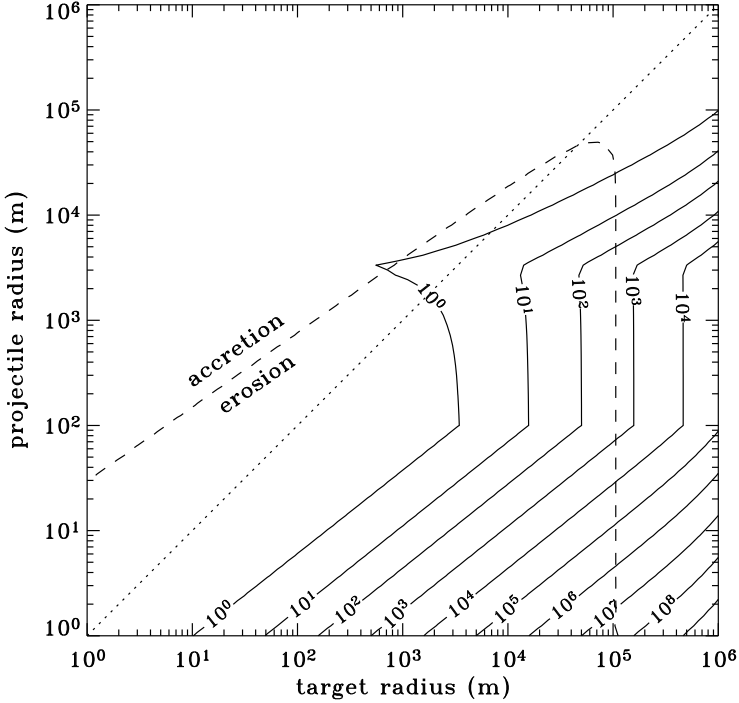


Figure 5.2 – The average number of collisions per target of a given size (solid contours) occurring in 4 Gyr with projectiles of different sizes. The dotted diagonal line indicates collisions between equal sized bodies. The dashed line confines the region where collisions are erosive. The figure was calculated using parameters listed in Table 5.1.

R_{\max} , completely define the collisional environment. Since the KBOs are binned according to their radii, their masses (calculated from the radii assuming spheres of density ρ) and the random velocities (Eqn. 5.3) are discretized accordingly.

The number of collisions between the target body and projectiles from the i th bin that occur in the time interval Δt , is estimated using a particle-in-a-box approach (Safronov 1969), and is given by

$$C_i = \frac{n_i}{4\pi a \Delta a h_i} \pi (R_t + r_i)^2 \left[1 + \frac{2G(M_t + m_i)}{(R_t + r_i)v_{\text{rel}}^2} \right] v_{\text{rel}} \Delta t, \quad (5.4)$$

where G is the universal gravitational constant, a and Δa are the radius and half-width of the Kuiper Belt, R_t and M_t are the mass and radius of the target body, n_i , m_i , and r_i are the number, mass, and radius of the projectiles in the i th bin, and v_{rel} is the relative velocity at infinity. The relative velocity is obtained from

$$v_{\text{rel}}^2 = v_t^2 + v_i^2$$

with v_t and v_i are the target and projectile velocities, respectively, given by Eqn. (5.3). The vertical extent of the orbits of the i th bin is given by (Kenyon & Luu 1998)

$$h_i \approx (a - \Delta a) \frac{v_i}{\sqrt{3} v_{\text{Kep}}},$$

where v_{Kep} is the Keplerian velocity, and assumes the eccentricities and inclinations of the orbits are related by $e \approx 2i$. Figure 5.2 shows the number of collisions in a 4 Gyr interval, as a function of target and projectile radius. Once the total number of collisions per size bin is known, the collisional sequence is randomized.

The collisional evolution is then initiated, with each collision being evaluated in turn. For each collision, the model computes the change in target mass and spin rate. The post-collision target mass depends on the ratio Q_I/Q_d , where Q_I is the center-of-mass impact energy per total (target+projectile) mass, and Q_d (the disruption energy per total mass) is defined as the energy needed to disperse 50% of the combined mass of the two bodies to infinity (see, e.g. Melosh & Ryan 1997; Benz & Asphaug 1999, and references therein). Q_I is given by (Wetherill & Stewart 1993)

$$Q_I = \frac{\mu v_I^2}{4(M_t + m_i)}, \quad (5.5)$$

where M_t is the target mass, $\mu = M_t m_i / (M_t + m_i)$ is the reduced mass, and v_I is the impact velocity, given by

$$v_I^2 = v_t^2 + v_i^2 + v_{\text{esc}}^2 \quad (5.6)$$

where v_{esc} is the mutual escape speed. Q_d has a bulk strength component and a gravitational component (Benz & Asphaug 1999):

$$Q_d = Q_b r^{\beta_b} + \rho Q_g r^{\beta_g}. \quad (5.7)$$

The value of r in the equation above is the radius of a sphere of mass $M_t + m_i$. This expression ignores a weak dependence of Q_d on the impact velocity (see, e.g., Benz & Asphaug 1999). We will consider two extreme cases for the bulk strength component, $Q_b = 0$ and $Q_b = 10^8$ erg/g, both size independent ($\beta_b = 0$), and show below that, in the target size range we choose to study, this property does not significantly influence the results. As for the gravity component, we follow Kenyon & Bromley (2004a) and normalize it at $r = 1$ km by making

$$Q_g = 1.5 \times (10^5)^{1.25 - \beta_g}, \quad (5.8)$$

and make use of scaling laws corresponding to icy targets ($\beta_g = 1.25$), rocky targets ($\beta_g = 1.40$) (Benz & Asphaug 1999), and asteroids ($\beta_g = 2$) (Durda et al. 1998). The mass remaining in the target after the impact is given by (Davis et al. 1985; Benz & Asphaug 1999)

$$M'_t = (M_t + m_i) [1 - 0.5(Q_I/Q_d)^{\beta_e}] \quad (5.9)$$

where β_e is a constant of order unity. The dashed line in Fig. 5.2 indicates collisions for which $M'_t = M_t$. Below the line the target's post-impact mass is smaller than its pre-impact mass, whereas for pairs target-projectile above the line the target mass increases.

The post-impact spin vector, $\vec{\omega}'_t$, is calculated by solving

$$\frac{8\pi}{15}\rho R'_t{}^5 \vec{\omega}'_t = \frac{8\pi}{15}\rho R_t^5 \vec{\omega}_t + m_i \vec{r} \times \vec{v}_I, \quad (5.10)$$

where ρ is the target and projectile density, R_t and R'_t are the target radii before and after the collision, $\vec{\omega}$ is the target spin frequency vector before the collision, \vec{r} is the radius vector of the impact point on the surface of the target, in the target's reference frame, and \vec{v}_I is the impact velocity vector. The post-impact target radius, R'_t , is calculated from Eqn. (5.9), assuming a spherical shape and density ρ . The impact point is chosen randomly on the surface of the target (entry point), and the impact velocity direction is determined by randomly picking another point on the surface (exit point). This process generates an isotropic distribution of collision geometries, from head-on to grazing. Equation (5.10) assumes that the ejected mass carries no angular momentum. This assumption maximizes the change in target spin per collision.

The change in mass and spin rate is computed for each collision. Catastrophic impacts can have two outcomes: (1) disintegration of the target, i.e., $Q_I > 2Q_d$, or (2) centripetal disruption of the target, i.e., if the spin frequency exceeds the critical spin frequency, given by

$$\omega_{\text{crit}} = \sqrt{(4/3)\pi G\rho}. \quad (5.11)$$

If the target is completely destroyed by a collision, the calculation stops. If the target exceeds the critical spin rate the calculation is not stopped but the object is flagged. As mentioned in Section 5.2.1, we choose not to stop the calculation at the critical spin rate because the latter, as given by Eqn. (5.11), is only a lower limit for the range of spin rate that can cause an object to blow itself apart. We thus choose to let the calculation continue and simply register the fact for statistical purposes.

If the target survives all collisions, we register its final spin and mass. The simulation can then begin all over, to yield a statistically significant distribution. Although the model follows all three components of $\vec{\omega}$, at the end of the calculation only the norm of the spin vector is registered. Only one parameter is changed at a time, and the model is run several times using each value of that particular parameter; in this way we obtain a Monte Carlo estimate of how the distribution of spins depends on a given parameter.

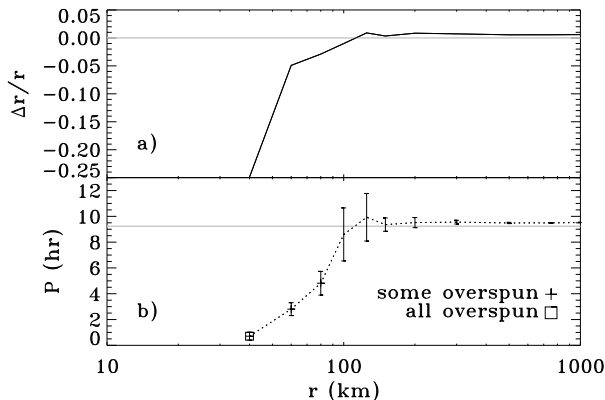


Figure 5.3 – Collisional evolution results for the parameters listed in Table 5.1. (a) The change in target radius, after 4 Gyr of collisional evolution, as a function of initial size. (b) The mean final spin rate of the target, as a function of initial size. Each point represents the mean of 50 model runs. 1σ dispersion bars are shown. Plus (square) symbols indicate that a fraction (all) of the 50 bodies have exceeded the critical spin (Eqn. 5.11).

5.3 Results and Discussion

The results yielded by the simulations are described below. A few are nearly independent of the choice of parameters:

1. Collisions do not change the spins of bodies with radii larger than roughly 200 km. In ~ 4 Gyr, these objects do not collide with enough large projectiles to alter their mass or spin angular momentum (see Fig. 5.2). Farinella et al. (1992) derived a similar result for the largest asteroids ($r > 100$ km).
2. The relative velocities of KBOs, \sim a few $\times 100$ m s $^{-1}$, are low enough to allow bodies $\gtrsim 100$ km to grow via collisions, albeit very slowly.
3. Most bodies with initial radii of 50 km or smaller do not survive 4 Gyr of collisional evolution. Catastrophic collisions destroy many of these bodies. Most of the rest reach spin rates larger than the critical spin rate and must lose mass to remain stable.

Figure 5.3 summarizes the results of our simulations for the parameters listed in Table 5.1. Figure 5.3a shows the change in size of KBOs due to 4 Gyr of collisional evolution, as a function of initial size. The horizontal gray line corresponds to the case where initial and final size are the same. With our standard parameters, the transition radius from net accretion to net erosion is $r_{\text{tr}} \sim 100$ km. Each point in Fig. 5.3a is the mean change obtained from 50 simulations. The bottom panel (5.3b) shows the final spin period of KBOs as a function of their initial size and spin. The horizontal gray line shows the initial spin period of the objects in the simulation. Here we use $P = 9.23$ hr, which is the observed mean spin period of KBOs with $r > 100$ km (Lacerda and Luu 2005, see Chapter 4). As in Fig. 5.3a, each point represents the mean final spin period, obtained from 50 simulations. The error bars show the 1σ dispersion. In the following sections we investigate how different parameters affect the trends shown in Fig. 5.3.

5.3.1 Effect of disruption energy scaling laws

We varied parameters Q_b and β_g to simulate different material properties. Given the large size of our targets ($r \gtrsim 50$ km), the bulk strength component of the disruption energy must play a less significant role than the gravitational component. Nevertheless we explored two extreme values, $Q_b = 0$ and $Q_b = 10^8$, with no dependence on target size ($\beta_b = 0$), to test how our result might depend on material strength. For the gravity component we considered values representative of different materials: $\beta_g = 1.25$ and $\beta_g = 1.40$, for ice and rock, respectively (Benz & Asphaug 1999), and $\beta_g = 2.00$ for asteroids (Durda et al. 1998).

Figures 5.4 and 5.5 show the change in radius and spin rate, respectively, as a function of initial size. Each point on the figures corresponds to the mean value obtained from 50 model runs. Parameter Q_b has little impact on the results, aside from rendering objects $\lesssim 40$ km more resistant to destruction. As for β_g , only $\beta_g = 2$ results in net accretion for all simulated initial radii, from 20 km to 1000 km. For $\beta_g = 1.25$ and $\beta_g = 1.40$ the transition radii from net erosion to net accretion are approximately $r_{\text{tr}} = 100$ km and $r_{\text{tr}} = 70$ km, respectively, and in both cases all bodies initially smaller than 40 km have been centrifugally disrupted. The values obtained for r_{tr} are consistent with previous simulations of KBO collisional evolution (Davis & Farinella 1997; Kenyon & Bromley 2004a).

The spin properties of KBOs do not seem to depend significantly on how strong they are, especially for bodies $\gtrsim 100$ km. Smaller, weaker objects (smaller β_g) are spun up more easily by collisions, mainly because of mass loss. Being weaker, these objects are easily eroded by the average collision, and thus spin up to conserve angular momentum, because the ejected material carries none (see Section 5.2.2).

5.3.2 Effect of density

Figures 5.6 and 5.7 summarize the results for three different body densities. In all three cases we obtain $r_{\text{tr}} \approx 100$ km. Changing the density has an opposite effect on bodies above and below r_{tr} : smaller bodies are more easily eroded if their density is lower, whereas for bodies $\gtrsim 100$ km, the lower the density the larger the growth. The reason is that, since all realizations of the model have the same total mass and same size distribution, lower bulk densities imply a larger number of bodies, and thus more collisions (see Fig. 5.8). For large targets (higher disruption energies), the extra collisions result in accretion, while at small sizes they result in erosion.

The spin properties as a function of size follow a similar trend. At sizes $r \gtrsim 100$ km, where collisions are accreting, lower density objects end up with slower spins, while the contrary is true for sizes where collisions are erosive $\lesssim 100$ km. This raises the question whether the change in spin might simply be due to conservation of spin angular momentum. To verify this we recompute

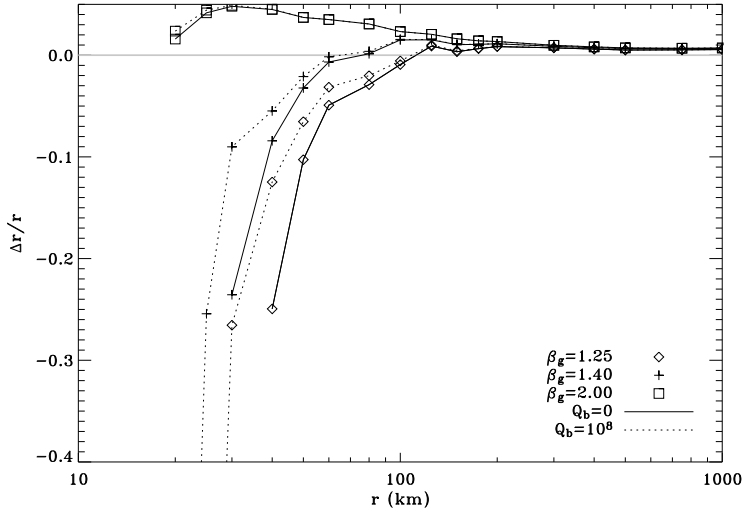


Figure 5.4 – The change in target radius, after 4 Gyr of collisional evolution, as a function of initial size, for different combinations of material properties. The lines simply connect the points. The horizontal gray line indicates no size change.

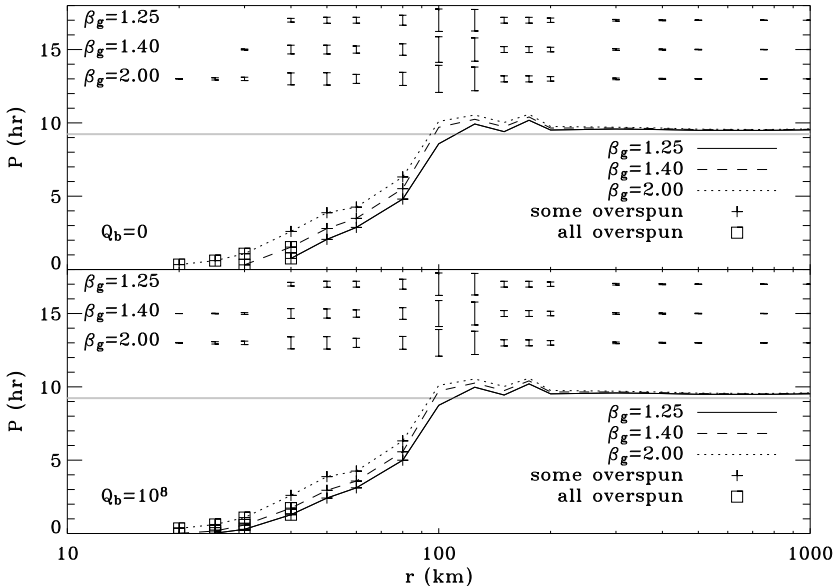


Figure 5.5 – The mean final spin rate of the target, after 4 Gyr of collisional evolution, as a function of initial size. Different lines indicate different combinations of material strength properties. Points represent the mean of 50 model runs. 1σ dispersion bars are shown at the top for each curve. Plus (square) symbols indicate that a fraction (all) of the 50 bodies have exceeded the critical spin (Eqn. 5.11).

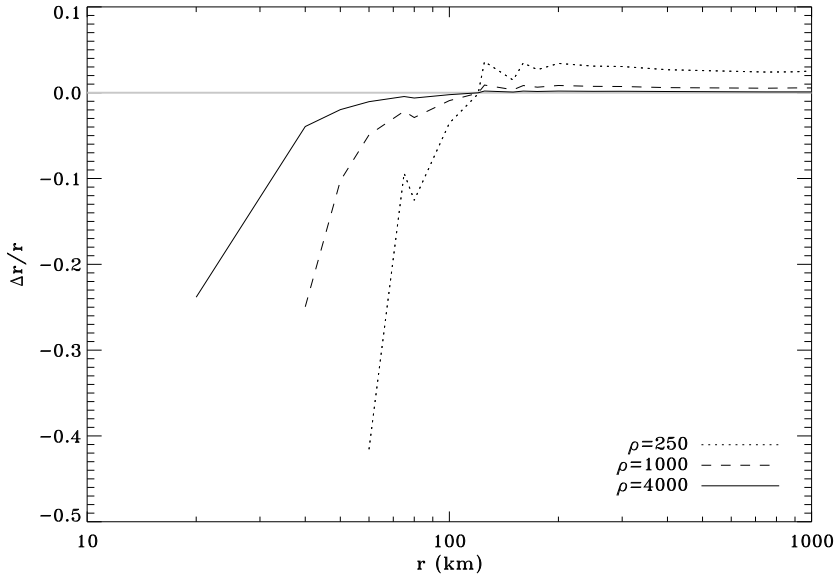


Figure 5.6 – Same as Fig. 5.4 but for different body densities, $\rho = 250 \text{ kg m}^{-3}$ (dotted line), $\rho = 1000 \text{ kg m}^{-3}$ (dashed line), and $\rho = 4000 \text{ kg m}^{-3}$ (solid line). The remaining body parameters are $Q_b = 0$ and $\beta_g = 1.25$.

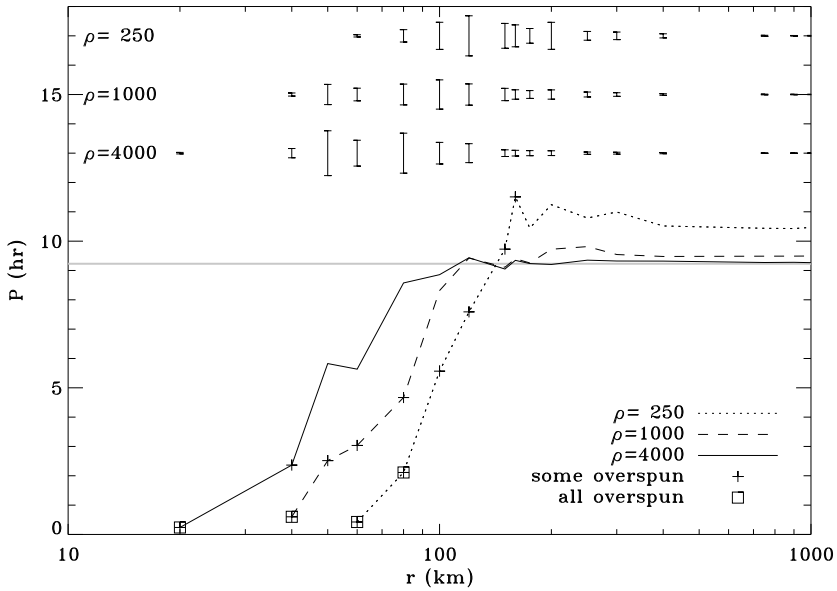


Figure 5.7 – The same as Fig. 5.5, but for different bulk densities.

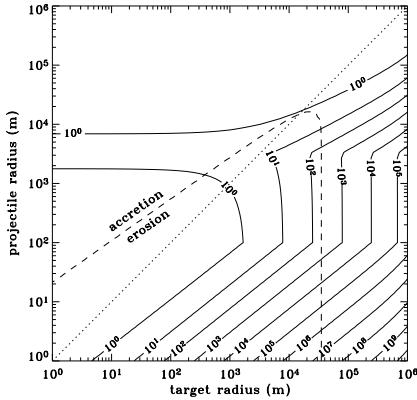


Figure 5.8 – The same as Fig. 5.2 but for a bulk density of bodies $\rho = 250 \text{ kg m}^{-3}$.

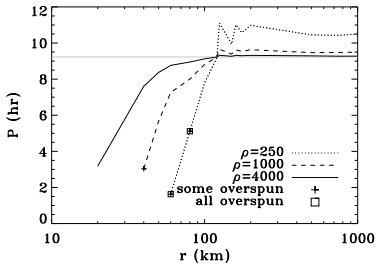


Figure 5.9 – The same as Fig. 5.7, but with every collision made head-on collisions, i.e., bringing no spin angular momentum to the target.

Fig. 5.7 but making every impact head-on. In this way collisions add (or remove) mass to the target, but no spin angular momentum. The result is shown in Fig. 5.9. Indeed, angular momentum conservation alone is enough to explain the spin-down for bodies larger than 100 km. This is not the case for smaller objects, where the contribution from collisions is more noticeable.

5.3.3 High angular momentum collisions

Figures 5.5 and 5.7 show that in the size range $r = 50 - 120 \text{ km}$, for some parameters, a fraction of the targets does not survive the high spin rates attained as a result of high angular momentum collisions (generally with projectiles of comparable size). The plus (+) signs in Figs. 5.5 and 5.7 mark sizes for which a fraction of the model runs resulted in bodies exceeding the critical spin (Eqn. 5.11). Square symbols indicate sizes for which all of the bodies exceed this limit.

These high angular momentum collisions could be responsible for the formation of fast spinning KBOs with elongated shapes (e.g., (33128) 1998 BU₄₈). Table 5.2 lists the KBOs from the current lightcurve database (Lacerda and Luu 2005, see Chapter 4) that meet this description. (Note: the listed sizes are based on the assumption that the albedo of KBOs is 0.04—assuming an albedo twice as large would result in sizes smaller by a factor $\sqrt{2}$). Based on our results, only

Object Designation	Radius ^a [km]	P^b [hr]	Δm^c [mag]	$a : b^d$	Ref. ^e
32929 1995 QY ₉	90	7.3	0.60 ± 0.04	1.7 : 1	1, 2
33128 1998 BU ₄₈	105	9.8	0.68 ± 0.04	1.9 : 1	1, 3
1999 DF ₉	170	6.65	0.40 ± 0.02	1.5 : 1	4
47932 2000 GN ₁₇₁	180	8.33	0.61 ± 0.03	1.8 : 1	1
26308 1998 SM ₁₆₅	200	7.1	0.45 ± 0.03	1.5 : 1	1, 3
20000 Varuna	490	6.34	0.42 ± 0.03	1.5 : 1	1

Table 5.2 – KBOs with high amplitude lightcurve and high spin rate. ^aThe radii assume an albedo of 0.04, except for Varuna which has a known albedo of 0.07 (Jewitt et al. 2001); ^bSpin period in hours; ^cLightcurve amplitude in magnitudes; ^dAxis ratio calculated from Δm assuming an aspect angle $\theta = \pi/2$; ^eReferences: (1) Sheppard & Jewitt (2002), (2) Romanishin & Tegler (1999), (3) Romanishin et al. (2001), (4) Lacerda and Luu (2005).

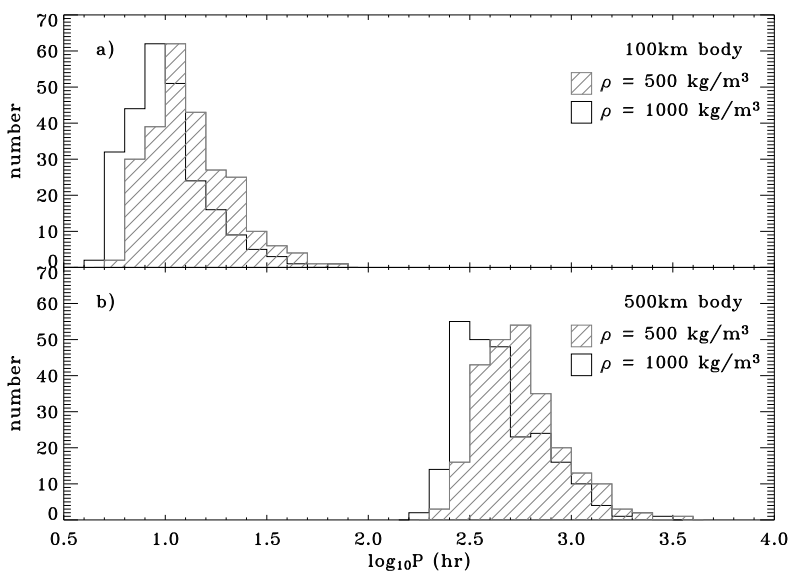


Figure 5.10 – The spin distribution of KBOs initially 100 km (top), and 500 km in radius (bottom). All bodies start with no spin. Different densities are shown as different fill patterns. Histograms are based on 250 runs of the model.

Varuna is too large to have suffered a high angular momentum collision in the last 4 Gyr of collisional evolution. If Varuna’s spin rate is due to a collision with a similar sized body, then it must have happened at a very early stage, just after it formed, when the Kuiper Belt was more massive (Jewitt & Sheppard 2002).

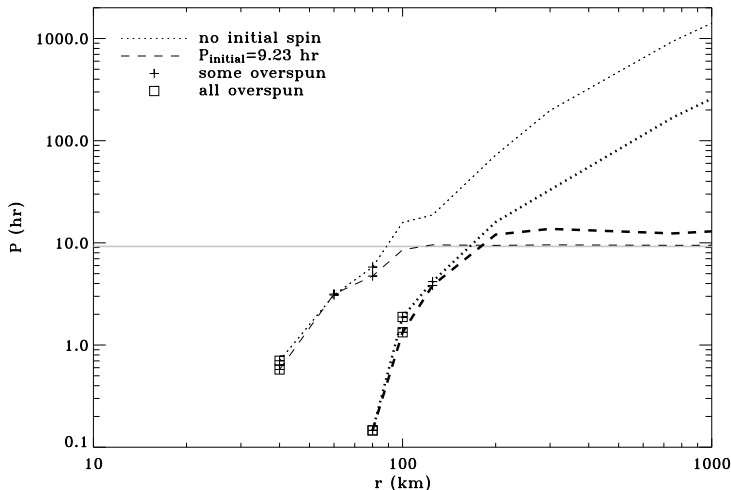


Figure 5.11 – The final mean spin period after 4 Gyr of collisional evolution, as a function of initial size, for bodies with no initial spin (dotted lines), and with initial spin period $P = 9.23$ hr (dashed lines). The effect of the total mass in the KBO region is also shown: thick lines are for $M_{\text{KBO}} = 10 M_{\oplus}$, and thin lines are for $M_{\text{KBO}} = 1 M_{\oplus}$. The result for each size represents the mean of 50 runs.

5.4 The origin of KBO spin rates

Can collisions in the last 4 Gyrs explain the observed spins of KBOs? For bodies in the size range $r = 50 - 100$ km they can. Figure 5.10 shows the distribution of spin rates for 100 km- and 500 km-radius KBOs predicted by our simulations. Note that these KBOs have no spin angular momentum initially. The Figure shows that 100 km bodies can be spun to $P \sim 10$ hr by collisions, but this is not the case for 500 km bodies. If these bodies have negligible spin by the end of the formation epoch (when our simulations start), collisions would only spin them up to $P \sim 500$ hr after 4 Gyr.

To test the robustness of this result we repeated the simulations, this time using a total KBO mass of $10 M_{\oplus}$ throughout the 4 Gyr of collisions, i.e., we assumed that the Kuiper Belt lost no mass since the formation epoch, 4 – 4.5 Gyr ago. This increases the total number of collisions, including those between large KBOs. The results for two distinct initial conditions, zero spin angular momentum and $P = 9.23$ hr (Note: $P = 9.23$ hr is the mean spin period of KBOs with $r > 100$ km (Lacerda and Luu 2005, see Chapter 4), are shown in Fig. 5.11. As expected, a more massive Kuiper Belt spins up KBOs more efficiently on average, resulting in mean periods of order $P \approx 100$ hr for $r = 500$ km bodies. But the consequences of a more intense collisional environment extend to all sizes: KBOs with $r = 100$ km are centripetally disrupted in such a massive environment (see

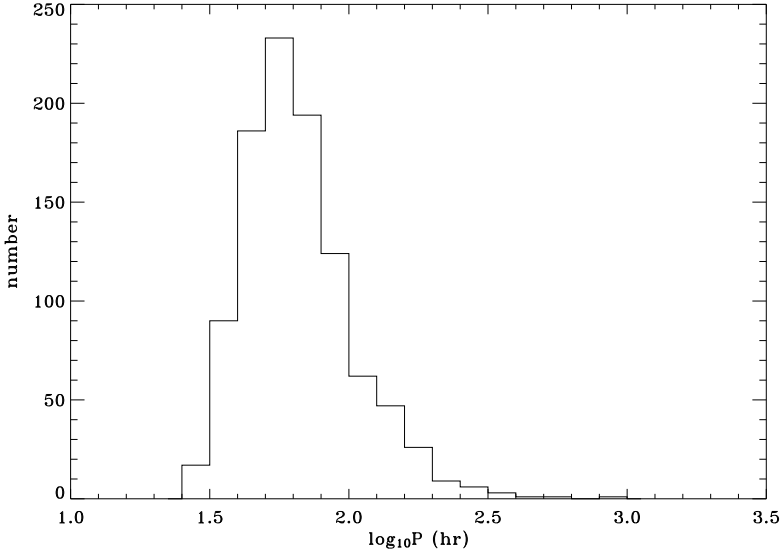


Figure 5.12 – The distribution of spins for 1000 bodies of initial radius $R = 500$ km. The histogram was calculated for $M_{\text{KBO}} = 10 M_{\oplus}$.

Fig. 5.11), which is not consistent with the observations. Besides, mean periods of ~ 100 hr still do not explain the spins of the largest KBOs (see Table 5.3). To assess the statistical significance of our result, we repeat the simulations for $r = 500$ km KBOs 1000 times, assuming a $10 M_{\oplus}$ Kuiper Belt. As before we consider KBOs with no initial spin. The result is shown in Fig. 5.12. None of the 1000 objects attained spin rates $P < 25$ hr. This implies that the probability of finding an object spinning that fast (with no initial spin) is $p < 0.001$. However, existing KBO data show that 4/7 (57%) of KBOs ~ 500 km in radius have spin periods $P < 20$ hr. The remaining 3/7 have “flat” lightcurves, which makes it impossible to measure their spins. Note that flat lightcurves may indicate very low spin periods, round shapes, or unfavourable observing geometry (Lacerda & Luu 2003, see Chapter 2).

As our simulations fail to reproduce the observed spin rates, it is therefore logical to conclude that, if a large fraction of 500 km KBOs spin today with a ~ 10 hr period, they must have had similar spins at the start of the collisional evolution. But if KBOs grew from isotropic accretion, angular momentum conservation would argue in favour of them having very little spin by the time they reached several hundreds of kilometers in size. It has been suggested that the high angular momentum of (20000) Varuna was the result of a collision with a similar size body, occurring very shortly after the largest KBOs had formed, while the KB was still massive (Jewitt & Sheppard 2002). The high fraction of

Object Designation	Radius [km]	P [hr]	Ref.
2003 AZ ₈₄	450	13.44	1
20000 Varuna	490	6.34	2
42301 2001 UR ₁₆₃	510	–	1
55637 2002 UX ₂₅	545	–	1
55636 2002 TX ₃₀₀	625	16.24	1
50000 Quaoar	650	17.69	3
28978 Ixion	655	–	1, 4

Table 5.3 – Spin rates of large KBOs. The radii were calculated assuming an albedo of 0.04, except for Varuna which has a known albedo of 0.07 (Jewitt et al. 2001); References: (1) Sheppard & Jewitt (2003), (2) Sheppard & Jewitt (2002), (3) Ortiz et al. (2003), (4) Chapter 4 of this thesis.

large KBOs with spin periods $P \sim 15$ hr would require this type of collisions to be very common.

5.4.1 Anisotropic accretion

An alternative explanation for the high fraction of large KBOs with high angular momentum is that accretion was not entirely isotropic. How anisotropic would accretion need to be to explain the spins of the largest KBOs? To try to answer this question we devised the following experiment: a body initially 5 km in radius is grown by accretion of smaller projectiles, until it reaches a radius of 500 km. The mass of each particle is set to be equal to a constant fraction k of the instantaneous mass of the growing body. The projectiles impact with a velocity equal to the escape velocity of the target, and always adhere to the target, i.e., no mass is ejected in the impacts. This is appropriate for simulating the runaway accretion phase, where relative velocities are small. The impact point and velocity are determined by randomly selecting two points on the surface of the target. The first (entry point) is the impact point, and the second (exit point) defines the direction of the impact velocity vector.

To parameterize anisotropy during accretion we define a parameter α , $0 \leq \alpha \leq 1$, where $\alpha = 1$ corresponds to completely isotropic accretion and $\alpha = 0$ completely anisotropic accretion. The regions allowed for the “entry” and “exit” points² of each projectile depend on α , and are given by

$$\begin{aligned}
 \theta_{\text{entry}}(x) &= \arccos(2x\alpha - 1), \\
 \psi_{\text{entry}}(y) &= \pi\alpha(2y - 1) + \pi/2, \\
 \theta_{\text{exit}}(z) &= \arccos(2z\alpha - 1), \\
 \psi_{\text{exit}}(w) &= \pi\alpha(2w - 1) + 3\pi/2,
 \end{aligned}
 \tag{5.12}$$

where x, y, z , and w are random real numbers selected in the $[0, 1]$ interval. These regions are illustrated in Fig. 5.13.

²The exit point defines, together with the entry point, the direction of the impact velocity. See Section 5.2.2.

Figure 5.13 – Allowed impact geometries for different values of the parameter α . The transparent mesh represents the entry region, i.e., the fraction of the target’s surface allowed to entry points, and the opaque grayscale section represents the exit region, i.e., fraction of the target’s surface allowed to exit points. When $\alpha > 0.5$ the exit region is not shown because it partly overlaps with the entry region.

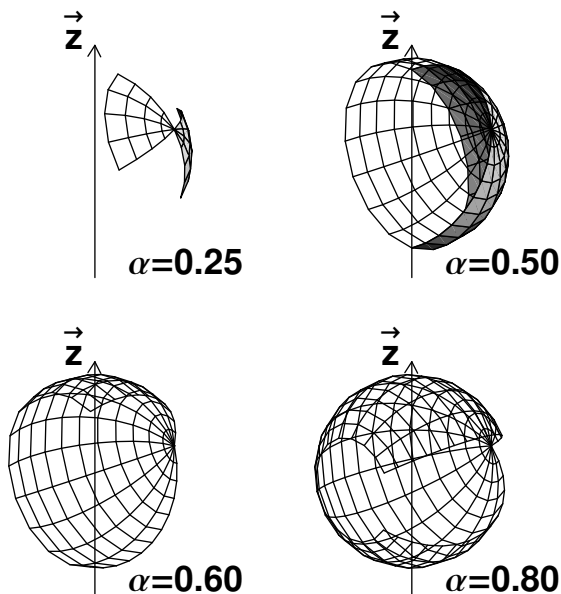
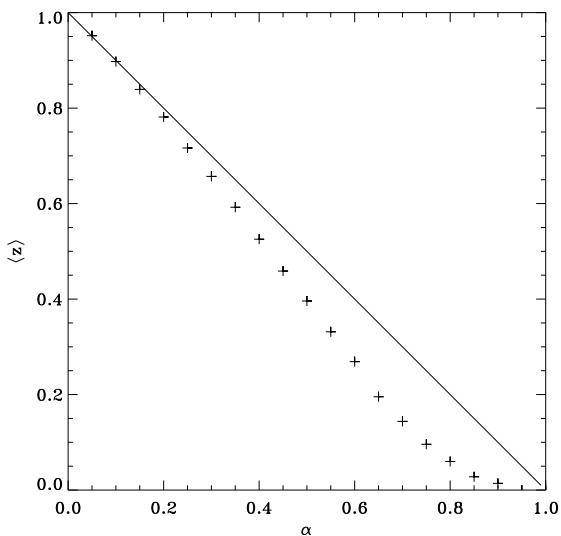


Figure 5.14 – The mean z -projection of the torque due to accreting projectiles, in arbitrary units, as a function of the anisotropy parameter α . The solid line, $\langle z \rangle = -\alpha$, is shown for reference. See text and Fig. 5.13.



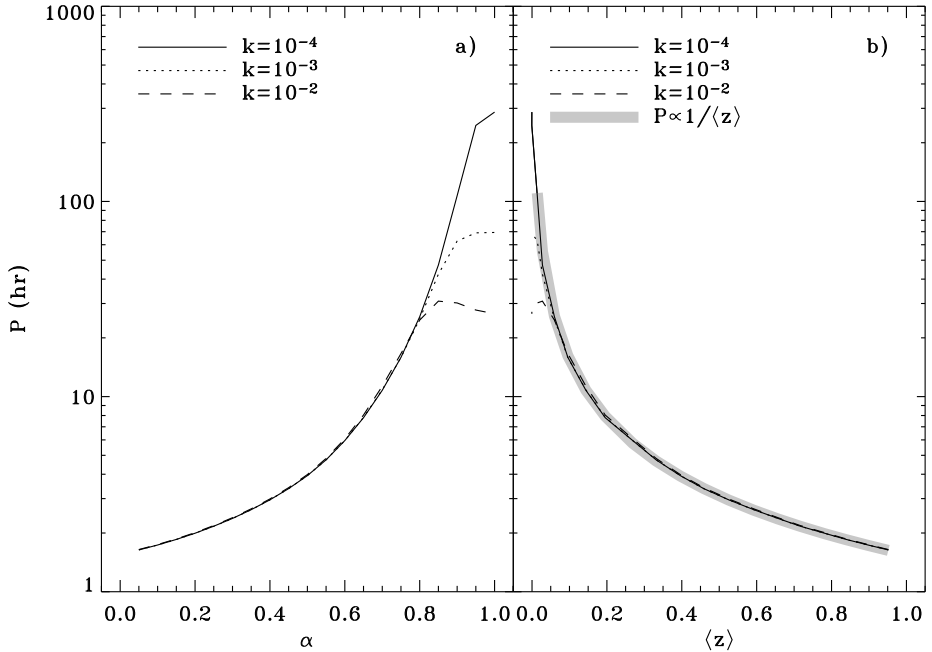


Figure 5.15 – The mean final spin of full grown ($r = 500$ km) bodies, as a function of α (left) and $\langle z \rangle$ (right). Different lines indicate different ratios of projectile mass to target mass, k . The thick gray line is a fit “by eye” of the form $P \propto 1/\langle z \rangle$.

Figure 5.14 illustrates how α translates into a more physically intuitive, torque-like, quantity. The vertical axis shows the mean z -projected (see Fig. 5.13) angular momentum brought into the target by each collision, in arbitrary units. For each different value of α (each point in Fig. 5.14) we generated 5000 pairs of vectors, each pair consisting of (1) the position vector of the impact point, connecting the origin with a randomly generated point on the surface of the target (entry point, Eqn. 5.12), and (2) the impact velocity vector, connecting the impact point with a second randomly chosen on the surface of the target (exit point, Eqn. 5.12, see above). Then we calculated the cross product of each pair of vectors³. The mean of the z -axis projections, $\langle z \rangle$, of all 5000 cross products is plotted. A value $\langle z \rangle \approx 0$ corresponds to nearly isotropic accretion where projectiles bring no preferential spin direction. If all projectiles tend to spin the target in the same direction then $\langle z \rangle \approx 1$.

In Fig. 5.15 we show the final spin period of the fully grown 500 km KBO as a function of α and as a function of $\langle z \rangle$. It is clear that the closer α is to 0, the faster the final spin. The Figure points out that accretion does not need to

³To normalize the result, we used the corresponding unit vectors instead of the vectors themselves.

be very anisotropic to make a 500 km body spin with a $\sim 10 - 20$ hr period by the time it reached full size. Values $\alpha = 0.7 - 0.8$ (corresponding to $\langle z \rangle \approx 0.1$) would explain the spin rates shown in Table 5.3. The ratio of projectile mass to target mass, k , also has an influence in the final spin of the growing KBO, but only if the accretion is nearly isotropic, i.e., if $\alpha \approx 1$ (see Fig. 5.15a). For values $\alpha < 0.8$ the final spin period is independent of how massive the accreted projectiles are with respect to the target. If accretion is isotropic, however, the final spin of the target depends considerably on k . Ratios of projectile mass to target mass of $k \gtrsim 0.01$ could explain the measured spin periods, even under completely isotropic growth. This corresponds to a ratio of projectile to target radius of $k^{1/3} \approx 0.2$.

Figures 5.16 and 5.17 show the evolution of the spin rate as the KBO grows. An equilibrium spin rate is attained very quickly in all cases, and it does not depend on the initial spin rate. The fluctuations in the spin rate due to individual projectiles are considerably smaller both with decreasing α (more anisotropic accretion), and with decreasing mass ratio of projectile to target. If the spin rate fluctuates the object tends to spend more the time at the higher spin rate. The reason for this is geometrical. Only collisions with a very specific impact geometry can slow down the spin rate; most impact geometries either change the spin direction or contribute to increase (or maintain) it. Moreover, if a collision happens to have the right geometry to slow down the spin, then *any* next collision will most likely increase the spin rate again. This is why the slower spin states are not lasting.

These results have the following implications:

1. Slight anisotropies in the accretion process can result in considerable spin angular momentum for the full grown bodies. A $\sim 10\%$ asymmetry in the angular momentum brought by accreted particles is enough to explain the observed spin rates. Anisotropic accretion also implies that the scatter in the final spin distribution of large KBOs should be small.
2. Isotropic accretion can explain the observed spin rates if the accreted particles are comparable in size to the growing object. If the particles are small, isotropic growth can only produce very slowly spinning objects ($P \sim 1000$ hr). Another consequence of isotropic accretion is that the scatter in the final spin distribution should be large.
3. Isotropic and anisotropic accretion should produce very different distribution of spin axis orientations. Isotropic accretion produces random axis orientations ($\langle z \rangle \approx 0$). Anisotropic accretion aligns the spin axes of KBOs, in the z -direction (see Fig. 5.13). Since the material from which KBOs accreted had cold, low inclination orbits (Malhotra 1995), it is reasonable to assume that any asymmetry originating in such a flat disk will favour an alignment of KBO spin axes perpendicular to the ecliptic. This is also what is observed for the majority of planets.

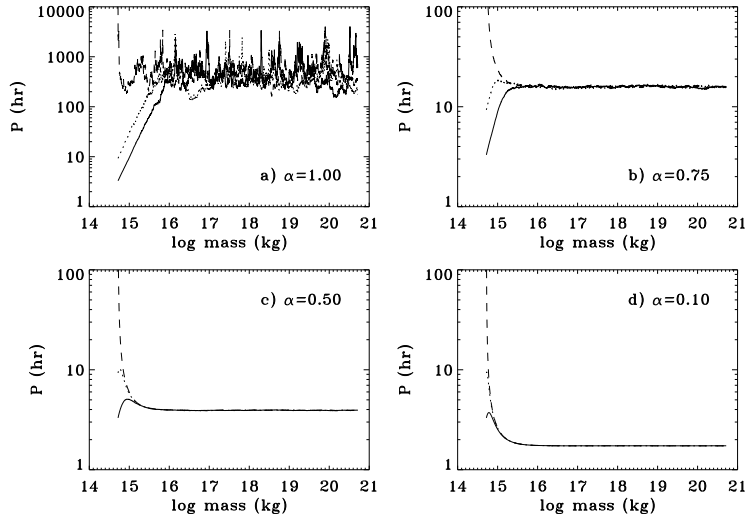


Figure 5.16 – The evolution of the target’s spin period as it grows for different values of α . Solid lines mean that the target is initially spinning with the critical spin period for its density, $P \approx 3.3$ hr ($\rho = 1000 \text{ kg m}^{-3}$), the dotted lines correspond to an initial spin period $P = 9.23$ hr, and dashed lines correspond to no initial spin. Parameter k was set to 0.5×10^{-4} .

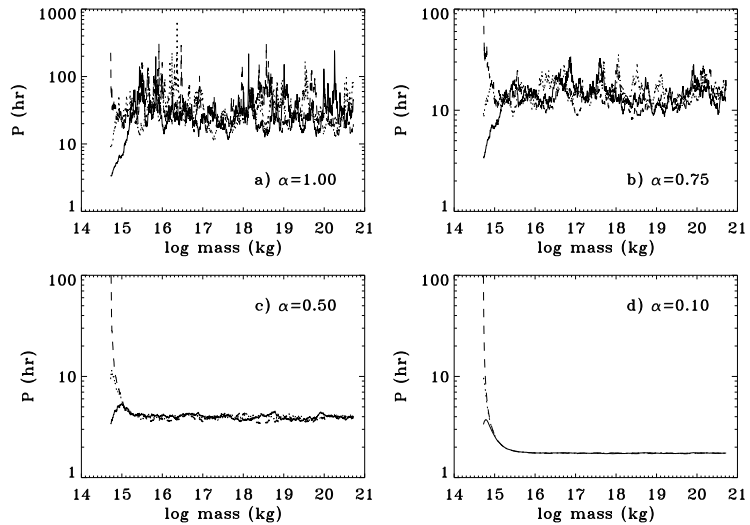


Figure 5.17 – The same as Fig. 5.16 but for $k = 10^{-2}$.

Speculating on the origin of anisotropies in the process of accretion is beyond the scope of this work. However, the explanation may lie in the dynamics of accreted particles close to and inside the region of gravitational influence of the growing bodies. We plan to investigate this in the future.

5.5 Limitations and future improvements

One of the main assumptions of the model is that each collision leaves all the angular momentum in the target. If this assumption is dropped, the conclusion that large KBOs have not had their spins significantly altered by 4 Gyr of collisions is only reinforced. However, the sizes for centrifugal disruption may change under more a detailed treatment of angular momentum partition in an impact event.

Another assumption is that we adopt a constant total mass and size distribution for KBOs. In reality the KB has probably lost $\sim 99\%$ of its original mass in the last 4 Gyr, and the size distribution has changed as a result of the collisional cascade (Kenyon & Bromley 2004a). An obvious extension to the model is to parameterize the time evolution of the KBO size distribution. Our results are a good first-order approximation, but collisions in a very early phase are not well accounted for. The results of Section 5.4.1 of this chapter give a hint of the effect of collisions with similar size bodies in an early KB.

Finally, the total number of collisions is calculated in a very deterministic way, i.e., a body of a given size always experiences the same number of collisions. KBOs exist in different dynamical classes, with different orbital properties. Bodies from different classes should thus have different collisional probabilities, and this is not accounted for. The data, however, are not numerous enough to distinguish between the spin properties of bodies in different dynamical classes.

5.6 Summary and Conclusions

We presented results of numerical simulations of KBO collisions. The time scale of our calculation starts when the bulk of the Kuiper Belt population is formed, 4 Gyr ago, and ends in the current epoch. In this period collisions are assumed to be the main type of interaction between KBOs. Each simulation follows a single target body as it collides with the surrounding bodies. Changes in the target's spin rate and mass are calculated for each collision. We studied the influence of various properties of the Kuiper Belt on the final distribution of spin rates. Our conclusions are as follows:

1. The spins of KBOs do not depend strongly on their bulk strength parameters.
2. KBOs with initial radius < 50 km do not survive the collisional evolution. They are disrupted into smaller pieces either by high energy collisions, or

by centripetal disruption due to the high spin rates attained. This is true for low tensile strength, icy material, as well as for moderately strong rocky composition. Therefore, most KBOs with $r < 50$ km are in principle not primordial, and should be by-products of collisions between larger bodies.

3. Collisions are slightly accreting for bodies with radius $r > 100 - 200$ km, resulting in a size growth of a few percent in the last 4 Gyr.
4. KBO with initial radii $\sim 50 - 120$ km lose 25–85% of their mass (10–50% decrease in size) as a result of collisions. Although not disrupted, these objects have suffered high angular momentum collisions capable of producing fast spin rates and rather elongated shapes. The current database of KBO spin properties indicates that, out of the 7 KBOs with fast spin rates and elongated shapes, 6 have sizes in this range.
5. The spins of KBOs larger than ~ 200 km cannot be explained by collisions if the objects had no spin angular momentum at the end of accretion. This suggests that the large KBOs must have attained their spin rates during, or very shortly after the accretion period.

The last point led us to the investigation of anisotropic accretion, as an explanation of the observed spins. We found that a $\sim 10\%$ asymmetry in the net angular momentum of accreted particles is enough to explain the observed mean spin rate. However, if the accreted particles were comparable in size to the growing body, no anisotropy is required. These two scenarios, anisotropic accretion of small particles, and isotropic accretion of large particles, make different predictions about the distribution of KBO spin rates and spin axis orientations: (1) Anisotropic accretion favours low scatter in the spin rates; (2) Isotropic accretion of larger building blocks predicts a large scatter in KBO spin rates and random spin axis orientations. The existing data are not large enough to discern between the two possibilities.

Acknowledgments

We would like to thank Ronnie Hoogerwerf for helpful discussion, and assistance with L^AT_EX.

References

- Benz, W. & Asphaug, E. 1999, *Icarus*, 142, 5
- Cameron, A. G. W. 1997, *Icarus*, 126, 126
- Catullo, V., Zappala, V., Farinella, P., & Paolicchi, P. 1984, *A&A*, 138, 464
- Davis, D. R. & Farinella, P. 1997, *Icarus*, 125, 50
- Durda, D. D., Greenberg, R., & Jedicke, R. 1998, *Icarus*, 135, 431
- Davis, D. R., Chapman, C. R., Weidenschilling, S. J., & Greenberg, R. 1985, *Icarus*, 62, 30
- Farinella, P., Davis, D. R., Paolicchi, P., Cellino, A., & Zappala, V. 1992, *A&A*, 253, 604
- Farinella, P., Paolicchi, P., & Zappala, V. 1981, *A&A*, 104, 159
- Goldreich, P., Lithwick, Y., & Sari, R. 2004, *ARA&A*, 42, 549
- Harris, A. W. 1979, *Icarus*, 40, 145
- Jewitt, D., Aussel, H., & Evans, A. 2001, *Nature*, 411, 446
- Jewitt, D. C. & Sheppard, S. S. 2002, *AJ*, 123, 2110
- Kenyon, S. J. & Luu, J. X. 1998, *AJ*, 115, 2136
- Kenyon, S. J. & Luu, J. X. 1999, *AJ*, 118, 1101
- Kenyon, S. J. & Bromley, B. C. 2004a, *AJ*, 128, 1916
- Kenyon, S. J. & Bromley, B. C. 2004b, *AJ*, 127, 513
- Lacerda, P. & Luu, J. 2003, *Icarus*, 161, 174
- Lacerda, P. and Luu, J. 2005, in preparation.
- Luu, J. X. & Jewitt, D. C. 2002, *ARA&A*, 40, 63
- Luu, J. & Lacerda, P. 2003, *Earth Moon and Planets*, 92, 221
- Malhotra, R. 1995, *AJ*, 110, 420
- Melosh, H. J. & Ryan, E. V. 1997, *Icarus*, 129, 562
- Ortiz, J. L., Gutiérrez, P. J., Sota, A., Casanova, V., & Teixeira, V. R. 2003, *A&A*, 409, L13
- Proctor, R. A. 1873, London, Longmans, Green, and co., 1873.
- Safronov, V. S. 1969, *Evoliutsiia doplanetnogo oblaka*.
- Romanishin, W. & Tegler, S. C. 1999, *Nature*, 398, 129
- Romanishin, W., Tegler, S. C., Rettig, T. W., Consolmagno, G., & Botthof, B. 2001, *Bulletin of the American Astronomical Society*, 33, 1031
- Sheppard, S. S. & Jewitt, D. C. 2003, *Earth Moon and Planets*, 92, 207
- Sheppard, S. S. & Jewitt, D. C. 2002, *AJ*, 124, 1757
- Wegener, A. 1975, *Moon*, 14, 211
- Wetherill, G. W. & Stewart, G. R. 1989, *Icarus*, 77, 330
- Wetherill, G. W. & Stewart, G. R. 1993, *Icarus*, 106, 190
- Whipple, F. L., Southworth, R. B., & Nilsson, C. S. 1967, *SAO Special Report*, 239

Nederlandse samenvatting

Het zonnestelsel

NEGEN planeten, Mercurius, Venus, Aarde, Mars, Jupiter, Saturnus, Uranus, Neptunus en Pluto, samen met de ster die wij de Zon noemen, vormen ons zonnestelsel. Tenminste, dat is wat we leren op school. De bovengenoemde planeten zijn geordend volgens hun afstand tot de Zon: van de dichtstbijzijnde tot de meest verafstaande. De eerste vier — Mercurius, Venus, Aarde en Mars — bestaan uit vaste materie, voornamelijk rotsgesteente, en zijn relatief klein, met diameters variërend van 4900 km (Mercurius) tot 12800 km (Aarde); zij zijn de zogenaamde “rotsachtige planeten”. Als we ons wegbewegen van de Zon zijn de vier die daarop volgen Jupiter, Saturnus, Uranus en Neptunus. Zij zijn enorme gasbollen, zonder een begaanbaar oppervlak. Deze “gasreuzen” zijn veel groter dan de rotsachtige planeten. Neptunus, de kleinste van de giganten, meet een diameter van bijna vier “Aardes”, en Jupiter, de grootste van alle planeten, heeft een diameter die elf keer groter is dan die van de Aarde. Als Jupiter de grootte had van een voetbal, dan zou Neptunus die van een tennisbal hebben en de Aarde die van een knikker. Op deze schaal zou de Zon een diameter van meer dan twee meter hebben.

De eerste acht planeten lijken een patroon te volgen — vier kleine rotsachtige in de binnenste regio en vier gigantische gasachtige in de buitenste regio. Bovendien zijn er grote overeenkomsten tussen de banen die planeten volgen: alle banen liggen in bijna hetzelfde vlak, de ecliptica, ze zijn bijna cirkelvormig en de banen worden allemaal in dezelfde richting doorlopen. De zes planeten die het dichtst bij de Zon staan, van Mercurius tot Saturnus, zijn met het blote oog waarneembaar en waren derhalve al bekend bij de eerste mensen die naar de hemel begonnen te turen. De twee verste planeten, Uranus en Neptunus, werden ontdekt met behulp van telescopen in respectievelijk 1781 en 1846. De ontdekking van Pluto, in 1930, compliceerde enigszins de ogenschijnlijke eenvoud

van het zonnestelsel. Pluto draait op hetzelfde vlak als de andere planeten rond de Zon, zijn baanvlak is nogal geheld ten opzichte van de ecliptica en de baan is zoveel langgerekter dat Pluto's baan gedeeltelijk ligt binnen die van Neptunus. Verder bestaat Pluto voornamelijk uit ijs en hij is heel klein. Was de Aarde zo groot als een knikker, dan zou Pluto iets kleiner zijn dan een peperkorrel. Deze gegevens tonen duidelijk aan dat Pluto verschilt van de andere planeten. Verderop in de tekst zullen we nog op deze planeet terugkomen.

Het zonnestelsel kent naast de Zon en de planeten ook nog andere families van objecten. Tussen de banen van Mars en Jupiter bestaat een ring vol kleine rotsachtige lichamen die asteroïden worden genoemd. Deze "kleine planeten" vormen de zogenaamde "asteroïdengordel". Ceres, de grootste van de asteroïden, meet een diameter van ongeveer 900 km en werd als eerste ontdekt, in 1801. Daarna werden nog enkele honderdduizenden asteroïden ontdekt, waarvan er slechts 26 een diameter hebben van meer dan 200 km. Het merendeel van de asteroïden is heel klein, en hoe kleiner, hoe talrijker ze zijn. Stel je voor dat alle asteroïden samengeperst zijn in een enorme bal van fimo; deze bal zou kleiner zijn dan de Maan. Als we deze bal verdelen in vier ballen van gelijke grootte, dan zou een van hen de grootte van Ceres hebben. Vervolgens maken we van een andere bal nog 25 asteroïden, degenen die samen met Ceres groter dan 200 km in doorsnee zijn. Uiteindelijk kunnen we met de laatste twee ballen alle andere, kleinere asteroïden maken.

Kometen

Een andere belangrijke familie van objecten in het zonnestelsel is die van de kometen. Vanwege hun spookachtige verschijning hebben deze hemellichamen altijd bewondering en zelfs angst opgeroepen. Zoals doorgaans gebeurt met wetenschappelijk onverklaarbare natuurlijke fenomenen, werden kometen beschouwd als gevreesde boodschappers van de goden en als voortekenen van catastrofes. Het was de invloedrijke Griekse filosoof Aristoteles die ze rond het jaar 340 v.C. voor het eerst als iets fysisch probeerde te duiden. Hij dacht dat het om lichtgevendende wolken ging die, gegeven hun veranderlijke gedrag, geen deel uit konden maken van het firmament, maar thuis hoorden in het ondermaanse. Aristoteles doopte hen "kometes" ("harig" in het Oud-Grieks). Eeuwen later, in 1577, gebruikte de Deense astronoom Tycho Brahe waarnemingen van een komeet, die op verschillende plaatsen in Europa waren gedaan, om aan te tonen dat er geen sprake kon zijn van een wolk in de dampkring. De komeet verscheen steeds in dezelfde positie in relatie tot de sterren, waar de waarnemingen ook waren gedaan. Als het een wolk in de dampkring was geweest en deze zou zich bijvoorbeeld boven Parijs bevinden, dan zou hij vanuit Lissabon in het noordoosten te zien zijn en vanuit Amsterdam in het zuiden. Brahe concludeerde dat de komeet zich verder van de Aarde moest bevinden dan de Maan.

In de 17de eeuw ontwikkelde de Engelse wis- en natuurkundige Isaac Newton een theorie die fundamenteel is gebleken voor de studie van het zonnestelsel en de gehele Kosmos. Hij kwam erachter dat alle objecten elkaar aantrekken met een kracht die proportioneel is aan hun massa. Op onze planeet geeft deze kracht betekenis aan de richtingen “naar boven” en “naar beneden”. De theorie van Newton, die de Universele Wet van de Zwaartekracht heet, verklaart waarom dingen vallen, waarom er getijden zijn, waarom de Maan om de Aarde draait, waarom de Aarde om de Zon draait, etcetera. Circa 20 jaar nadat Newton zijn theorie publiceerde, gebruikte Edmund Halley haar om de banen van kometen te berekenen. Deze banen zijn ellipsvormig. Een ellips¹ is een soort cirkel met twee middelpunten, die “brandpunten” worden genoemd. Hoe verder deze uit elkaar liggen, hoe langwerpiger de ellips is. In de banen van kometen en planeten² is de Zon een van die brandpunten. De berekeningen van Halley brachten hem tot de voorspelling dat een bepaalde komeet, die in 1456, 1531 en 1607 was verschenen, opnieuw in 1758 te zien zou moeten zijn. De komeet verscheen inderdaad met Kerst van dat jaar en staat sindsdien bekend als de komeet van Halley — Halley zelf was toen al 12 jaar dood. De laatste verschijning van de komeet van Halley was in 1986.

Men wist echter nog steeds niet waar de kometen vandaan kwamen of waaruit ze bestonden. Aan het eind van de 18de eeuw formuleerden de Duitse filosoof Immanuel Kant en de Franse wetenschapper Pierre Laplace de hypothese dat alle lichamen van het zonnestelsel afkomstig waren van een enorme draaiende wolk van gas en stof. Deze wolk zou zich door de zwaartekracht hebben samengetrokken en de Zon in het middelpunt hebben gecreëerd. Maar een deel van de materie kwam terecht in een sneldraaiende schijf om de Zon en uit de materie daarvan ontstonden de planeten. Dit idee, dat 250 jaar geleden voor het eerst onder woorden werd gebracht, wordt tegenwoordig ondersteund door tal van waarnemingen en is een algemeen aanvaarde theorie geworden. Dit scenario zou suggereren dat kometen op dezelfde manier als planeten worden gevormd, namelijk vanuit die opeenhopingen. Maar waarom zijn ze dan geen planeten geworden? Meer aanwijzingen voor het doorgronden van deze mysteries werden ontdekt rond 1950 door Fred Whipple en Jan Hendrik Oort.

De eerste, een Amerikaanse astronoom, kwam tot de conclusie dat kometen een soort vuile, stoffige sneeuwballen zijn. De uitdrukking “dirty snowball” is van Whipple zelf afkomstig. Dankzij hun sterk elliptische banen bevinden deze objecten van ijs zich voor een groot deel van de tijd ver van de Zon, daar waar de temperaturen het absolute nulpunt, -273°C , naderen. Wanneer een komeet richting het centrum van het zonnestelsel beweegt, dan stijgt de temperatuur door de nabijheid van de Zon en gaat zijn bevroren oppervlak direct over van vast naar gasvormig. Een deel van dit gas omgeeft de bevroren kern van de

¹De figuur op de voorkant van dit boek bestaat uit zeven, binnen elkaar liggende ellipsen.

²In het geval van de planeten liggen de brandpunten zo dicht bij elkaar dat de ellips haast een cirkel is.

komeet in de vorm van een lichtgevende halo, die “coma” wordt genoemd. De rest wordt door het zonlicht weggeduwd, waardoor de komeet een staart krijgt die altijd van de Zon af wijst. Het stof dat inmiddels is vrijgekomen uit het ijs bij diens overgang van vast naar gas, vormt een tweede staart die bijna samenvalt met de eerste, maar die vanwege zijn “zwaardere gewicht” enigszins naar achteren helt.

In het jaar 1950 gebruikte de Nederlandse astronoom Jan Oort twee observatieve gegevens om de oorsprong van kometen te verklaren. Terwijl de astronomen de banen bepaalden van meer en meer van deze objecten, werd duidelijk dat er twee verschillende subgroepen bestonden: kortperiodieke kometen, die iedere 5 tot 200 jaar terugkeren naar het centrum van het zonnestelsel (hierbij hoort de komeet van Halley, met een periode van ± 75 jaar), en langperiodieke kometen die er meer dan 200 jaar over doen om terug te keren. Bij deze laatste groep horen ook kometen die sinds het ontstaan van de mensheid slechts één keer de Zon genaderd zijn — kometen die maar eens in de 10 miljoen jaar terugkeren. Deze kometen hebben extreem langgerekte banen, wier uiterste punten meer dan 100 000 astronomische eenheden³ van de Zon verwijderd zijn. Oort merkte op dat: (1) een grote hoeveelheid kometen van dergelijke afstanden kwamen, dus van meer dan 100 000 AU, en (2) deze kometen in de nabijheid van de Zon vanuit alle richtingen kwamen. Deze constatering brachten Oort ertoe het bestaan voor te stellen van een grote bol om de schijf van het zonnestelsel heen, van waaruit de kometen naar de kern, dus naar de Zon vallen. Deze grote bol, gelegen op een afstand van meer dan 100 000 AU van de Zon, zou de bron zijn van de kometen die ons in de kern van het zonnestelsel bezoeken. Als erbetoon aan de man die dit alles bedacht had, werd deze bron de “Oortwolk” gedoopt. Het woord “wolk” werd gekozen als een verwijzing naar een bolvormige stofwolk, waarin de kometen de stofdeeltjes zijn.

Toch is het vreemd dat kometen zo ver van de Zon ontstaan. De wolk van gas en stof die door Kant en Laplace voorzien was, van waaruit zich het zonnestelsel gevormd zou hebben, zou mogelijk een te lage dichtheid hebben op die afstand voor de vorming van de opeenhopingen. Een Nederlandse astronoom, die genaturaliseerd was tot Amerikaan, Gerard Kuiper, was zich ook bewust van dit probleem en had een ander idee. Als kometen uit ijs bestaan worden ze in principe ver van de warmte van de Zon gevormd — maar er niet zo ver vandaan als de Oortwolk. Kuiper bedacht het volgende: misschien werden kometen dichtbij de grens van ons planetaire stelsel “geboren”, voorbij Neptunus, en werden ze na verloop van tijd de Oortwolk in geslingerd door de gigantische gasplaneten. Als de ruimte voorbij Neptunus inderdaad de wieg van de kometen was, dan zouden er zich daar veel meer moeten bevinden en die zouden dan Pluto in zijn baan rond de Zon gezelschap houden. Deze potentiële kometen waren waarschijnlijk bevroren en wachtten het moment af waarop ze de warmte van de Zon konden opzoeken, of gelanceerd werden richting de Oortwolk. Er is in-

³Een astronomische eenheid (AU) komt overeen met de afstand van de Aarde naar de Zon.

derdaad gezocht naar deze “trans-Neptuniaanse” kometen, maar dit bracht geen succes. Op zo’n afstand van de Zon, ongeveer 40 AU, gaf alleen Pluto een teken van leven. De mislukte pogingen leidden ertoe dat de hypothese van Kuiper aan kracht verloor.

In 1988 zorgde een andere kwestie, die van de banen van de kortperiodieke kometen, ervoor dat drie onderzoekers, Martin Duncan, Thomas Quinn en Scott Tremaine weer in het idee van Kuiper gingen geloven. De kortperiodieke kometen hebben banen die bijna liggen in het baanvlak van de planeten. Daarnaast zijn er de langperiodieke kometen die, zoals reeds is gezegd, komen van de verre Oortwolk en de Zon vanuit allerlei richtingen naderen. Met deze twee groepen van kometen voor zich werd de vraag — zoals de kwestie van de kip en het ei — welke van de twee de eerstgeborene was. Kon het zo zijn dat de langperiodieke kometen, vanuit alle richtingen afkomstig en met een afwijkende baan, “getemd” konden worden, om zo kortperiodieke kometen te worden, met een weinig afwijkende baan? Of waren het toch de brave kortperiodieke kometen, die zo nu en dan richting de Oortwolk gelanceerd werden in langgerekte en afwijkende banen? Duncan, Quinn en Tremaine testten deze eerste hypothese met een computersimulatie. De conclusie was dat je de langperiodieke kometen niet kunt temmen; bovendien concludeerden de drie dat de kortperiodieke kometen vanuit een “donut” vormig gebied moesten komen, die aan de rand van het zonnestelsel gelegen was, precies zoals Kuiper het had bedacht. In het artikel dat zij publiceerden, doopten Duncan en zijn collega’s deze hypothetische gordel van kometen de “Kuiper Belt”.

De technologische revolutie aan het eind van de 20ste eeuw bracht grote voordelen voor de astronomie met zich mee. Telescopen die telkens groter werden en beter uitgerust waren, lieten ons tot in detail het Heelal zien, iets wat tot dan toe onmogelijk was geweest. Dave Jewitt en Jane Luu, twee astronomen van de Universiteit van Hawaï, waren zich bewust van dit feit. Zij besloten de jacht te openen op deze kometengordel van Kuiper met behulp van de telescopen op de top van de vulkaan Mauna Kea, op 4000 m hoogte. Geduldig zochten zij nacht na nacht een lichtpunt waarvan de beweging zou aangeven dat het om een trans-Neptuniaans object ging. Maar de jaren gingen voorbij en Jewitt en Luu zagen niets. Tot in 1992, vijf jaar nadat ze aan hun zoektocht waren begonnen, zij een klein object zagen dat een diameter had van ongeveer 200 km. Dit object bewoog zich in een bijna perfect circulaire baan, niet ver van die van Pluto. Zes maanden later vonden ze een ander object in een soortgelijke baan, aan de andere zijde van het zonnestelsel.

Sindsdien zijn er bijna duizend “Kuiper Belt Objects” ontdekt. Deze nieuwe familie van trans-Neptuniaanse objecten veranderde de status van Pluto in de hiërarchie van het zonnestelsel. De vreemde, kleine en bevroren planeet blijkt de grootste van de KBO’s te zijn, zoals Ceres de grootste van de asteroïden is. De ontdekking van de Kuiper Belt riep een nieuw onderzoeksgebied in het leven. Hoewel de trans-Neptuniaanse objecten de oplossing lijken te zijn van het

probleem van de oorsprong van kometen, is wat men over ze weet eigenlijk bijna niets. Opdat we een van die objecten vanaf de Aarde kunnen zien, moet het zonlicht, in de vorm van minuscule deeltjes genaamd fotonen, meer dan vijf uur reizen, weerkaatsen op het oppervlak van het object en terugkeren om ons te bereiken. Het is niet zo dat de fotonen hier *moe* aankomen. Het probleem is dat er maar *weinig* ons bereiken — het overgrote deel gaat tijdens de tocht verloren. In de astronomie zijn de fotonen de boodschappers van alle informatie die ons bereikt. Hoe meer fotonen we ontvangen van een bepaald object, des te meer informatie we kunnen bemachtigen. Doordat er maar weinig arriveren van de trans-Neptuniaanse objecten weten we zo weinig over hen. Waarschijnlijk zullen we op een dag sondes kunnen zenden, zoals die welke naar Mars gaan, opdat we meer over deze kleine bevroren werelden te weten kunnen komen.

Dit proefschrift

In de wetenschappelijke literatuur worden de Kuiper Belt objecten aangeduid met KBO's. Soms worden ze ook wel TNO's genoemd, "Trans-Neptunian Objects". KBO's lijken een soort babyplaneten te zijn. In het al genoemde model van Kant-Laplace klonteren de opeenhopingen die rond de Zon achterblijven samen en groeien ze tot ze planeten worden. Astronomen noemen deze opeenhopingen in de groeifase "planetesimals". De regio van de KBO's bevindt zich ver van de Zon, waar minder materiaal aanwezig was om planetesimals te vormen. Daarom groeiden de KBO's langzamer. Toen het materiaal op was, waren de KBO's nog in hun kindertijd, dus nog lang geen planeten. En zo zijn ze gebleven, bevroren. Om deze reden is de bestudering van de KBO's van groot belang voor meer inzicht in het formatieproces van planeten.

Dit proefschrift presenteert een studie van de vormen en rotaties van de KBO's. Om uit te leggen waarin het belang ligt de vormen van de KBO's te kennen, kunnen we het voorbeeld van de asteroïden gebruiken. De vorm van de kleinste asteroïden komt overeen met die van stukken die erafvliegen wanneer je een steen breekt. Dit geeft aan dat deze objecten inderdaad dergelijke dingen zijn: brokstukken als gevolg van zeer krachtige botsingen tussen grote asteroïden. De hoofdstukken 3 en 4 van dit proefschrift laten zien dat een groot deel van de KBO's relatief rond is, maar dat een aanzienlijk percentage ovale of langwerpige vormen heeft. Waarom dit zo is, is nog niet bekend. Wel geeft de snelheid waarmee een KBO om zijn as draait ons informatie over diens interne structuur, vooral als we de vorm van de KBO weten. Bijvoorbeeld: als een object massief is, kan het vrij snel draaien, zonder dat zijn vorm verandert. Maar als een KBO een opeenhoping van kleine fragmenten is (een "afvalhoop" of "rubble pile"), dan maken de rotaties het object ovaler. Als het te snel draait kan het zelfs uiteenspatten. In hoofdstuk 4 worden de vormen en rotaties van de KBO's samen geanalyseerd en die lijken aan te tonen dat de KBO's inderdaad opeenhopingen van veel kleinere brokken zijn die alleen bij elkaar blijven door

de zwaartekracht en niet doordat ze een samenhangende substantie zijn. Hoofdstuk 5 bestudeert de botsingen tussen de KBO's. Het doel is om te verifiëren of de draaiing van de KBO's wordt veroorzaakt door botsingen met andere KBO's vanaf het moment van hun geboorte. De conclusie luidt dat de grootste KBO's dezelfde rotatiesnelheid hebben als toen ze ontstonden, maar dat de rotatiesnelheid van de kleinste compleet veranderd is door de botsingen. De botsingen lijken overigens de reden te zijn van het feit dat de KBO's opeenhopingen van fragmenten zijn: voortdurende collisions breken en vergruizen geleidelijk aan deze objecten, die door de zwaartekracht bijeengehouden worden.

Aan het eind van hoofdstuk 1 staat een meer gedetailleerde samenvatting van dit proefschrift.

Resumo em Português

O sistema solar

NOVE planetas, Mercúrio, Vénus, Terra, Marte, Júpiter, Saturno, Urano, Neptuno, e Plutão, juntamente com a estrela a que chamamos Sol, formam o nosso sistema solar. Pelo menos é isto que aprendemos na escola. Os planetas acima citados estão ordenados do mais próximo para o mais distante do Sol. Os primeiros quatro — Mercúrio, Vénus, Terra e Marte — são sólidos, constituídos maioritariamente por rocha, e relativamente pequenos, com diâmetros entre 4 900 km (Mercúrio) e 12 800 km (Terra); são os chamados “planetas rochosos”. Os quatro que se seguem, à medida que nos afastamos do Sol, — Júpiter, Saturno, Urano e Neptuno — são enormes esferas de gás, sem uma superfície onde se possa caminhar. Estes “gigantes gasosos” são muito maiores do que os planetas rochosos. Neptuno, o mais pequeno dos gigantes, mede quase 4 “Terras” em diâmetro, e Júpiter, o maior de todos os planetas, tem um diâmetro 11 vezes superior ao da Terra. Se Júpiter fosse do tamanho de uma bola de futebol, Neptuno seria do tamanho de uma bola de ténis e a Terra seria do tamanho de um berlinde. Nesta escala, o Sol teria mais de dois metros de diâmetro.

Os primeiros oito planetas parecem seguir um padrão — quatro pequenos rochosos na região interior, e quatro gigantes gasosos na região exterior. Além disso, movem-se de forma bastante regular — todos circulam o Sol no mesmo sentido, em órbitas heliocêntricas¹, quase circulares e coplanares². Os seis planetas mais próximos do Sol, Mercúrio a Saturno, são visíveis a olho nú e, portanto, do conhecimento dos homens desde que estes olharam para os céus com atenção. Os dois mais distantes, Urano e Neptuno, foram descobertos com o auxílio de telescópios em 1781 e 1846, respectivamente. A descoberta de Plutão, em 1930, veio complicar ligeiramente a aparente simplicidade do sistema solar, e aguçar a curiosidade dos cientistas. Plutão orbita o Sol no mesmo sentido dos restantes

¹Centradas no Sol.

²Todas assentes no mesmo plano, como as faixas de um disco de vinil imaginário.

planetas, mas fá-lo de uma forma mais irregular. A sua órbita é inclinada em relação ao plano da eclíptica³, e é alongada, de tal forma que Plutão umas vezes está mais perto do Sol do que Neptuno, outras vezes está mais longe. Para além disso, Plutão é composto principalmente de gelo, e é muito pequeno. Na nossa escala em que a Terra tem o tamanho de um berlinde, Plutão seria ligeiramente mais pequeno do que um grão de pimenta. Estes factos mostram claramente que Plutão é diferente dos outros planetas. Voltaremos a Plutão mais adiante.

O sistema solar tem outras famílias de objectos, para além do Sol e dos planetas. Entre as órbitas de Marte e Júpiter existe uma região repleta de pequenos corpos rochosos, chamados asteróides. Estes “planetas menores” formam a chamada “cintura de asteróides”. Ceres, o maior dos asteróides, tem cerca de 900 km de diâmetro, e foi o primeiro a ser descoberto, em 1801. Desde então, várias centenas de milhares de asteróides foram descobertos, dos quais apenas 26 têm mais de 200 km em diâmetro. Os asteróides são, na sua grande maioria, muito pequenos, e quanto mais pequenos mais numerosos. Imaginem todos os asteróides “amassados” numa única e gigante bola de plasticina: essa bola seria menor do que a Lua. Se a dividíssemos em quatro bolas iguais, uma delas seria do tamanho de Ceres. Depois, usaríamos outra bola para fazer mais 25 asteróides, os tais que, juntamente com Ceres, são maiores que 200 km. Finalmente, as últimas duas bolas seriam suficientes para fazer todos os outros asteróides.

Cometas

Outra importante família de objectos do sistema solar é a dos cometas. Por causa da sua aparência fantasmagórica, estes astros sempre suscitaram admiração, e até medo. Como geralmente acontece com fenómenos naturais para os quais não existe explicação científica, os cometas foram considerados temíveis mensageiros dos deuses, e prenúncio de catástrofes. Foi o influente filósofo grego Aristóteles que cerca do ano 340 a.C. tentou, pela primeira vez, explicar os cometas como algo de físico. Ele julgava tratarem-se de nuvens luminosas que, dado o seu comportamento errático, não poderiam fazer parte do firmamento. Aristóteles baptizou-os de *kometes* (“cabeludos”, do Grego antigo). Séculos mais tarde, em 1577, o astrónomo dinamarquês Tycho Brahe recorreu a observações de um cometa feitas de diversos locais na Europa para mostrar que este não podia ser uma nuvem na atmosfera: o cometa aparecia na mesma posição no céu, em relação às estrelas, de onde quer que as observações fossem feitas. Se fosse uma nuvem, e a nuvem estivesse por exemplo sobre Paris, quando vista de Lisboa esta apareceria a nordeste, mas vista de Amesterdão apareceria a sul. Brahe concluiu que o cometa teria que estar longe da Terra, mais longe do que a própria Lua.

No século XVII o físico e matemático inglês Isaac Newton desenvolveu uma teoria que viria a ser fundamental para o estudo do sistema solar, e do Cosmos.

³O plano da órbita da Terra em torno do Sol, ou o tal “disco invisível” onde assentam as órbitas dos planetas.

Newton percebeu que todos os objectos se atraem mutuamente, com uma força que é proporcional à sua massa. No nosso planeta essa força dá significado às direcções “para cima” e “para baixo”. A teoria de Newton, chamada Lei da Gravitação Universal, explica porque é que as coisas caem para a Terra, porque é que há marés, porque é que a Lua anda à volta da Terra, porque é que a Terra anda à volta do Sol, etc. Cerca de 20 anos depois de Newton publicar a sua teoria, Edmund Halley usou-a para calcular as órbitas dos cometas. Estas órbitas são elipses. Uma elipse⁴ é uma espécie de circunferência com dois centros, chamados “focos”. Quanto mais afastados são os focos mais alongada é a elipse. Nas órbitas de cometas e planetas⁵, o Sol ocupa um dos focos. Os cálculos de Halley levaram-no a propôr que um determinado cometa, que tinha aparecido em 1456, 1531 e 1607, deveria reaparecer em 1758. De facto o cometa apareceu, no Natal desse ano, e ficou desde então conhecido como o cometa de Halley. A última aparição do cometa de Halley foi em 1986.

Mas os cientistas continuavam sem saber de onde vinham, ou do que eram feitos, os cometas. No final do século XVIII, o filósofo alemão Immanuel Kant e o cientista francês Pierre Laplace puseram a hipótese de que todos os corpos do sistema solar provinham de uma enorme nuvem de gás e poeira. Essa nuvem, rodando no espaço, ter-se-ia contraído sobre si própria, por acção da força da gravidade, e formado o Sol no centro. As regiões exteriores formariam aglomerados que, devido à rotação da nuvem, ficariam em órbita em torno do Sol, dando origem aos planetas. Esta ideia, formulada há 250 anos, veio a ser reforçada por inúmeras observações e é hoje a explicação aceite para a formação do nosso (e outros) sistema planetário. Neste cenário, faz sentido pensar que os cometas se formaram da mesma maneira que os planetas, a partir dos tais aglomerados. Mas então porque é que não são como os planetas? Mais pistas para entender estes mistérios foram descobertas por volta de 1950 por Fred Whipple e Jan Hendrik Oort.

O primeiro, astrónomo americano, chegou à conclusão que os cometas são uma espécie de bolas de neve sujas de poeira. A expressão “dirty snowball” é da autoria do próprio Whipple. Graças às suas órbitas elípticas, estes objectos passam grande parte do tempo congelados longe do Sol, onde as temperaturas se aproximam do zero absoluto, -273°C . Quando um cometa se aproxima do centro do sistema solar, o aumento de temperatura resultante da proximidade do Sol faz com que a sua superfície gelada passe directamente do estado sólido ao estado gasoso. Uma parte deste gás envolve o núcleo gelado do cometa sob a forma um halo luminoso, chamado “coma”, e o restante é literalmente empurrado pela radiação solar, formando a cauda do cometa. Por isso as caudas dos cometas apontam na direcção oposta à do Sol. A poeira entretanto libertada do gelo quando este passa a gás forma uma segunda cauda que quase coincide com a primeira, mas por ser mais “pesada” fica ligeiramente para trás.

⁴A figura na capa deste livro é formada por sete elipses, umas dentro das outras.

⁵No caso dos planetas os focos estão tão próximos que a órbita é quase uma circunferência.

No ano de 1950, o astrónomo holandês Jan Oort usou dois dados observacionais para propôr uma origem para os cometas. À medida que os astrónomos determinavam as órbitas de mais e mais destes objectos, tornou-se claro que existiam dois subgrupos distintos: os cometas de *curto período*, que voltam ao centro do sistema solar cada 5 a 200 anos (onde se inclui o cometa de Halley, cujo período orbital são ± 75 anos), e os cometas de *longo período* que demoram mais de 200 anos a voltar. Este último grupo inclui cometas que só se aproximaram do Sol uma vez desde o aparecimento dos primeiros homens — cometas que só voltam uma vez em cada 10 milhões de anos. Estes cometas têm órbitas extremamente alongadas, que os transportam a distâncias de mais de 100 000 unidades astronómicas⁶ do Sol. Oort reparou que: (1) uma grande quantidade de cometas vinha de distâncias dessa ordem, de mais de 100 000 AU, e (2) esses cometas chegavam às proximidades do Sol vindos de todas as direcções. Estas constatações levaram Oort a propôr a existência de uma região esférica, envolvendo o disco do sistema solar como uma gigante bola de vidro, de onde os cometas caem para o centro, onde se encontra o Sol. Esta região esférica, situada a mais de 100 000 AU do Sol, funcionaria assim como fonte para os cometas que nos visitam no centro do sistema solar. Em homenagem ao homem que a idealizou, esta fonte foi baptizada de “nuvem de Oort”. A palavra “nuvem” foi escolhida em alusão a uma nuvem esférica de poeira, em que os cometas são os grãos de pó.

É estranho, no entanto, que os cometas se tenham formado tão longe do Sol. A nuvem de gás e poeira idealizada por Kant e Laplace, de onde se formou o sistema solar, seria demasiado ténue a essa distância para permitir a formação de aglomerados. Ciente deste problema, um astrónomo holandês naturalizado americano, Gerard Kuiper, teve outra ideia. Se os cometas são feitos de gelo, em princípio formaram-se longe do calor do Sol. Mas não tão longe quanto a nuvem de Oort. Kuiper imaginou o seguinte: talvez os cometas tenham “nascido” perto do limite do nosso sistema planetário, na região além-Neptuno, e com o passar do tempo alguns deles foram sendo “lançados” para a nuvem de Oort pelos planetas gigantes gasosos⁷. Se de facto a região trans-Neptuniana é o berço dos cometas, então ainda lá deverão residir vários, fazendo companhia a Plutão na sua órbita em torno do Sol. Estes candidatos a cometas estarão congelados, aguardando a sua vez de se aproximarem do calor do Sol, ou de serem lançados em direcção à nuvem de Oort. Os astrónomos apontaram os seus telescópios para o céu, em busca dos tais potenciais cometas mas não tiveram sucesso. De tal distância do Sol, cerca de 40 AU, só Plutão dava sinais de existência. As tentativas falhadas fizeram com que a hipótese de Kuiper fosse perdendo força.

Em 1988, uma outra questão, a das órbitas dos cometas de *curto período*, fez com que três cientistas, Martin Duncan, Thomas Quinn e Scott Tremaine,

⁶Uma unidade astronómica é a distância entre a Terra e o Sol, e designa-se por AU.

⁷De um modo semelhante ao usado pelos atletas olímpicos quando lançam uma bola de metal presa na ponta de um cabo, rodando sobre si próprios e largando o cabo.

voltassem a acreditar na ideia de Kuiper. Os cometas de *curto período* têm órbitas pouco inclinadas, ou seja, que não se afastam muito do disco onde os planetas se movem. Por outro lado, e como foi referido atrás, os cometas de *longo período* vêm da distante nuvem de Oort, e aproximam-se do Sol vindos de todas as direcções. Face a estes dois grupos de cometas os cientistas interrogaram-se — ao jeito da história do ovo e da galinha — qual teria “nascido” primeiro. Será que os cometas de longo período, vindos de todas as direcções e inclinações, podem ser “domados”, passando a ter órbitas de curto período, e pouco inclinadas? Ou serão, pelo contrário, os bem comportados cometas de curto período que, de vez em quando, são lançados para órbitas alongadas e inclinadas, em direcção à nuvem de Oort? Duncan, Quinn e Tremaine decidiram fazer uma simulação usando um computador para testar a primeira hipótese. A conclusão foi que não é possível domar os cometas de longo período. Além disso, os três cientistas concluíram que os cometas de curto período têm necessariamente de vir de uma cintura em forma de bolo-rei, em torno do sistema solar, exactamente como Kuiper imaginara. No artigo que publicaram, Duncan e colegas baptizaram a hipotética cintura de cometas de “cintura de Kuiper”.

A revolução tecnológica dos finais do século XX trouxe grandes vantagens para a astronomia. Telescópios cada vez maiores e melhor equipados mostravam-nos o Universo com um detalhe até então impossível. Dave Jewitt e Jane Luu, dois astrónomos da Universidade do Havai, aperceberam-se desse facto e decidiram voltar à caça da tal cintura de cometas de Kuiper, usando telescópios situados no topo do vulcão Mauna Kea, a 4000 metros de altitude. Pacientemente, noite após noite, procuraram um ponto luminoso cujo movimento indicasse tratar-se de um objecto trans-Neptuniano. Mas os anos passavam e Jewitt e Luu não viam nada. Até que em 1992, cinco anos depois de terem iniciado a busca, eles avistaram um pequeno objecto, com cerca de 200 km de diâmetro. Este objecto movia-se numa órbita quase perfeitamente circular, ligeiramente mais distante do que a de Plutão. Seis meses mais tarde encontraram outro objecto, numa órbita semelhante, do lado oposto do sistema solar.

Desde então quase mil “objectos de Kuiper” foram descobertos. Esta nova família de objectos trans-Neptunianos veio alterar o estatuto de Plutão na hierarquia do sistema solar. O estranho, pequeno, e gelado planeta é afinal o maior dos objectos de Kuiper, assim como Ceres é o maior dos asteróides. A descoberta da “cintura de Kuiper” entusiasmou a comunidade científica e fez nascer uma nova área de investigação. Embora os objectos trans-Neptunianos pareçam ser a solução do problema da origem dos cometas, o que se sabe sobre eles é quase nada. Para que consigamos ver um destes objectos a partir da Terra, é necessário que a luz do Sol, sob a forma de minúsculas partículas chamadas fotões, viaje durante mais de cinco horas, seja reflectida pela superfície do objecto, e volte a viajar outro tanto de volta até nós. Não é que os fotões cheguem cá cansados. O problema é que chegam poucos — a maior parte perde-se pelo caminho. Em astronomia, os fotões são os mensageiros de toda a informação que nos chega.

Quanto mais fótons recebemos de um determinado objecto, mais informação podemos obter. É por chegarem poucos vindos dos objectos trans-Neptunianos que nós sabemos tão pouco acerca deles. Provavelmente, um dia teremos de mandar sondas, semelhantes às que vão a Marte, para aprendermos mais sobre estes pequenos mundos gelados.

Esta tese

Nos textos científicos, os objectos de Kuiper são vulgarmente designados por KBOs (do inglês, Kuiper Belt objects). Por vezes, também se usa a designação TNOs, de Trans-Neptunian objects. Julga-se que os KBOs sejam uma espécie de planetas bebés. No modelo de Kant-Laplace referido atrás, os aglomerados que ficam em órbita em torno do Sol vão-se juntando e crescendo até formar os planetas. Os astrónomos chamam a estes aglomerados em fase de crescimento, “planetesimais”. Na região dos KBOs, por ser distante do Sol, havia menos material para formar planetesimais. Por isso os KBOs cresceram mais devagar. Quando o material se esgotou os KBOs estavam ainda na fase da infância, longe de se tornarem planetas. E assim ficaram, congelados. Por essa razão, o estudo dos KBOs é vital para perceber o processo da formação dos planetas.

Esta tese apresenta um estudo das formas e rotações dos KBOs. Para explicar a importância de conhecer as formas dos KBOs, podemos usar o exemplo dos asteróides. Os mais pequenos tem formas equivalentes às dos estilhaços que saltam ao partir uma pedra. Isto indica que estes objectos são isso mesmo: estilhaços resultantes de violentas colisões entre asteróides maiores. Os Capítulos 3 e 4 desta tese mostram que grande parte dos KBOs são relativamente redondos, mas que existe uma percentagem considerável com formas mais ovóides, ou alongadas. Não é possível para já saber porquê. Por outro lado, a velocidade de rotação de um KBO dá-nos informação acerca da sua estrutura interna, especialmente se soubermos a forma do KBO. Por exemplo, se o objecto for maciço, pode rodar bastante depressa, e a sua forma não se alterará significativamente. Mas se o KBO for um amontoado de pequenos fragmentos, a rotação deformará o objecto tornando-o mais ovóide. Se rodar demasiado depressa pode mesmo desintegrar-se. No Capítulo 4, as formas e as rotações dos KBOs são analisadas em conjunto, e parecem indicar que os KBOs são mesmo amontoados de blocos mais pequenos, que se mantém juntos graças à força da gravidade. O Capítulo 5 estuda as colisões entre KBOs. O objectivo é verificar se a rotação dos KBOs foi provocada por colisões entre eles, desde que se formaram até aos nossos dias. A conclusão é que os maiores KBOs têm a mesma rotação que tinham quando se formaram, mas a rotação dos mais pequenos foi completamente alterada pelas colisões. Por outro lado as colisões parecem ser a razão pela qual os KBOs são amontoados de fragmentos: impactos sucessivos foram rachando e partindo o interior destes objectos transformando-os lentamente em blocos de entulho.

No final do Capítulo 1 é apresentado um resumo mais detalhado desta tese.

Curriculum vitae

MARCH 27th, 1975. That was my birthday. I was born in Lisbon, Portugal. I learned to speak relatively early, and as soon as I could say a few words, I started asking questions. I had no particular preference on the subject, which later proved to be one of my good (and bad) characteristics. I went to school at the Escola do Magistério Primário, Escola Preparatória Delfim Santos, and finally Escola Secundária de Benfica. I liked school a lot. Mathematics was my favourite subject. Teachers say I was always agitated, and distracting my colleagues. Besides school I did swimming, tennis, and judo. And I have always liked music, which I often played with friends. When I was about ten years old my uncle gave me his old computer, a ZX Sinclair 48K. In hindsight I think this was very good for me. I lived most of my youth in a neighbourhood called Benfica. Most of my friends are there.

After highschool I went to the Instituto Superior Técnico in Lisbon, to become an engineer. A little over 3 years later I decided that I wanted to study theoretical Physics instead, and moved to the Faculty of Sciences of the University of Lisbon. In the meantime I worked part-time at an internet service provider. Another 3 years later, when I was in my last year of Physics, I worked at the Center for Astronomy and Astrophysics of the University of Lisbon. During that time I joined observing runs with Prof. Yun at La Silla, and Dr. Roos-Serote at Calar Alto. In 1999 I attended a summer school on solar system science (EVISS, Coimbra), organized by Dr. Roos-Serote, where I met Prof. Jewitt. Shortly after, I applied, and was accepted, to a PhD position in Leiden, to work with Dr. Jane Luu on Kuiper Belt research.

I was very fortunate to be able to live and study in Leiden. During my PhD research I carried out several observing runs at the William Hershel and Isaac Newton telescopes on La Palma, and at the Dutch 0.9m, Danish 1.5m, ESO 2.2m telescopes at La Silla. I participated in the NOVA fall school in Dwingeloo (2000), and attended conferences at Meudon (2001), Penn State (2001), the NAC in 2002, Berlin (2002), Porto (2002), and the IAU General Assembly in Sydney (2003). I assisted Dr. Luu with the teaching of the Leiden-Dwingeloo Summerschool in Astrophysics (2001). I enjoyed a very fruitful visit to the Harvard-Smithsonian Center for Astrophysics (2002), where I worked with Dr. Kenyon. At the CfA, I assisted Profs. Donnelly and Stanek with the course Astronomy 1.

In the coming 3 years, I will continue my studies of Kuiper Belt objects at Coimbra, with Prof. João Fernandes, and at Hawaii, with Prof. Dave Jewitt.

Nawoord / Acknowledgments

WRITTEN words take space whereas feelings and memories don't. Therefore I will only be able to mention a few of the many people that helped in the making of this thesis. Nevertheless, I would like to thank everyone I have had contact with in the past, for I have learned from all of you.

To everybody at the Sterrewacht, my deepest thanks for making my stay such a pleasant one. I leave with the wish that I may come back. Marja Zaal, Janet Soulsby, Kirsten Groen, and Jeanne Drost, thank you for being always so helpful. The Sterrewacht computer group has been outstanding everytime I needed their support. I thank Garrelt for being the best office mate I could possibly have. I am grateful to Glenn, Michele, and others for many fruitful discussions, in the spirit of how I believe that science should be pursued. I thank the SocCom and the Big Dipper for organizing many entertaining events, and for the Friday borrels. I have enjoyed the hospitality of everyone at the Harvard-Smithsonian Center for Astrophysics, where I conducted a part of the research presented here. I thank Mango and her housemates for all their support, patience, and friendship, in a crucial step during the preparation of this thesis.

Antonietta, Chris (moran taing!), Gaetano e Luca, vi ringrazio per tanti giorni carini, e perché siete delle persone molto belle. Mariska, thank you for not allowing any day at the Sterrewacht to be boring. I thank Maaïke for always smiling, and adding a bit of poetry to many days. Davor, thanks for being a good friend. As my *allochtoon* buddy, you have a unique perception of how much I will miss Leiden. Ivo, thank you for your friendship, which I deeply treasure.

I am greatly indebted to all my past teachers for my academic education. In connection with this thesis, I thank Prof. Yun and Prof. Agostinho for motivating me to pursue my studies in astronomy. I acknowledge Dr. Roos-Serote for his contribution to Portuguese astronomy, and for organizing a great summer school in Coimbra, which eventually triggered my coming to Leiden. Catarina, obrigado por me teres encorajado. Obrigado a todos os meus amigos em Portugal, por serem sempre uma boa razão para voltar.

Lieve Maaïke, dankjewel voor de mooiste vertaling van mijn samenvatting, voor jouw geduld met me, en voor 10000 andere dingen.

Por último, quero agradecer a toda a minha família porque foi nela, e dela, que formei a base de quem eu sou.